

SPINTRONIC PROPERTIES OF CARBON AND SILICON BASED NANOSTRUCTURES

A DISSERTATION SUBMITTED TO
THE DEPARTMENT OF PHYSICS
AND THE INSTITUTE OF ENGINEERING AND SCIENCE
OF BILKENT UNIVERSITY
IN PARTIAL FULFILLMENT OF THE REQUIREMENTS
FOR THE DEGREE OF
DOCTOR OF PHILOSOPHY

By
Engin Durgun
August, 2007

I certify that I have read this thesis and that in my opinion it is fully adequate, in scope and in quality, as a dissertation for the degree of doctor of philosophy.

Prof. Dr. Salim ıracı (Supervisor)

I certify that I have read this thesis and that in my opinion it is fully adequate, in scope and in quality, as a dissertation for the degree of doctor of philosophy.

Prof. Dr. Cemal Yalabık

I certify that I have read this thesis and that in my opinion it is fully adequate, in scope and in quality, as a dissertation for the degree of doctor of philosophy.

Prof. Dr. Bilal Tanatar

I certify that I have read this thesis and that in my opinion it is fully adequate, in scope and in quality, as a dissertation for the degree of doctor of philosophy.

Assist. Prof. Özgür Oktel

I certify that I have read this thesis and that in my opinion it is fully adequate, in scope and in quality, as a dissertation for the degree of doctor of philosophy.

Prof. Dr. Şakir Erkoç

Approved for the Institute of Engineering and Science:

Prof. Dr. Mehmet B. Baray
Director of the Institute

ABSTRACT

SPINTRONIC PROPERTIES OF CARBON AND SILICON BASED NANOSTRUCTURES

Engin Durgun

Ph. D. in Physics

Supervisor: Prof. Dr. Salim Çıracı

August, 2007

In this thesis, nanostructures which may display novel spintronic behaviors are revealed and their properties are investigated by using first-principles methods. We have concentrated on three different systems, namely carbon linear chains, single-wall carbon nanotubes and silicon nanowires. First of all, an extensive study of the electronic, magnetic and transport properties of finite and infinite-periodic atomic chains composed of carbon atoms and $3d$ transition metal (TM) atoms are carried out. Finite-size, linear molecules made of carbon atomic chains capped with TM atoms, i.e. TM- C_n -TM structures are found to be stable and exhibit interesting magnetoresistive properties. The indirect exchange interaction of the two TM atoms through a spacer of n carbon atoms determines the type of the magnetic ground state of these structures. The n -dependent variations of the ground state between ferromagnetic (F) and antiferromagnetic (AF) spin configurations exhibit several distinct features, including regular alternations and irregular forms. We present a simple analytical model that can successfully simulate these variations, and the induced magnetic moments on the carbon atoms. The periodically repeated TM- C_n atomic chains exhibit half-metallic properties with perfect spin polarization at the Fermi level (E_F). When connected to appropriate electrodes the TM- C_n -TM atomic chains act as molecular spin-valves in their F states due to the large ratios of the conductance values for each spin type. Secondly, a systematic study of the electronic and magnetic properties of TM atomic chains adsorbed on the zigzag single-wall carbon nanotubes (SWNTs) is presented. The adsorption on the external and internal wall of SWNT is considered and the effect of the TM coverage and geometry on the binding energy and the spin polarization at E_F is examined. All those adsorbed chains studied have F ground state, but only their specific types and geometries demonstrated high spin polarization near E_F . Their magnetic moment and binding energy in the ground state display interesting variation with the number of d -electrons of the TM

atom. Spin-dependent electronic structure becomes discretized when TM atoms are adsorbed on finite segments of SWNTs. Once coupled with non-magnetic metal electrodes, these magnetic needles or nanomagnets can perform as spin-dependent resonant tunnelling devices. The electronic and magnetic properties of these nanomagnets can be engineered depending on the type and decoration of adsorbed TM atom as well as the size and symmetry of the tube.

Finally, bare, hydrogen terminated and TM adsorbed Silicon nanowires (SiNW) oriented along [001] direction are investigated. An extensive analysis on the atomic structure, stability, elastic and electronic properties of bare and hydrogen terminated SiNWs is performed. It is then predicted that specific TM adsorbed SiNWs have a half-metallic ground state even above room temperature. At high coverage of TM atoms, ferromagnetic SiNWs become metallic for both spin-directions with high magnetic moment and may have also significant spin-polarization at E_F . The spin-dependent electronic properties can be engineered by changing the type of adsorbed TM atoms, as well as the diameter of the nanowire.

Most of these systems studied in this thesis appear to be stable at room temperature and promising for spintronic devices which can operate at ambient conditions. Therefore, we believe that present results are not only of academic interest, but also can initiate new research on spintronic applications of nanostructures.

Keywords: First principles, ab initio, density functional theory, spintronics, nanoscience, nanostructures, half-metal, spin-valve, giant magneto resistance.

ÖZET

KARBON VE SİLİKON TABANLI NANOYAPILARIN SPİNTRONİK ÖZELLİKLERİ

Engin Durgun

Fizik, Doktora

Tez Yöneticisi: Prof. Dr. Salim Çıracı

Ağustos, 2007

Bu çalışmada, ilk prensip teknikleri ile spintronik uygulamalarda kullanılacak nanomalzemeler araştırılmıştır. Öncelikle karbon ve $3d$ geçiş metallerinden (GM) oluşan sonlu ve periyodik atom zincirlerinin elektronik, manyetik ve iletkenlik özellikleri incelenmiştir. Sonlu ve doğrusal GM- C_n -GM moleküler yapılarının kararlı sistemler oldukları ve ilginç manyeto-direnç özellikleri gösterdikleri bulunmuştur. Bu yapıların manyetik temel durumları, GM'lerin aradaki n tane karbon atomu üzerinden endirek etkileşimleri tarafından belirlenmektedir. Temel manyetik durum n 'e bağlı olarak ferromanyetik (F) ve antiferromanyetik (AF) spin konfigürasyonları arasında değişim göstermektedir. Bu değişimler basit bir analitik model ile başarılı bir şekilde taklit edilmiştir. Periyodik GM- C_n yapıları yarı metalik karakter kazanmakta, dolayısıyla Fermi seviyesi (E_F) yakınlarında tam spin kutuplaşması göstermektedir. GM- C_n -GM yapıları uygun elektrotlara bağlandıklarında, F temel durumunda her spin yönü için farklı iletkenliklere sahip olmakta ve moleküler spin-vanası gibi davranmaktadır.

İkinci olarak, üzerinde GM atom zincirleri soğurulmuş tek çeperli zigzag karbon nanotüplerin (TÇKN) elektronik ve manyetik özellikleri çalışılmıştır. TÇKN'nin çeperlerine içten ve dıştan soğurulma dikkate alınmış ve bağlanma enerjisinin ve spin polarizasyonun nelere bağlı olduğu incelenmiştir. Tüm incelenen sistemlerin temel durumu ferromanyetik bulunmuş ancak yüksek spin kutuplaşması bazı GM'ler için ve uygun geometrilerde gözlenmiştir. GM atomları sonlu TÇKN'ler üzerine soğurulduklarında spine bağlı elektronik yapı kesikli hale gelmektedir. Elde edilen bu manyetik iğneler ya da nano mıknatıslar metal elektrotlara bağlanarak spintronik aygıt olarak kullanılabilirlerdir.

Son olarak çıplak, hidrojenle kaplanmış ve GM atomları soğurmuş [001] yönündeki silikon nanoteller (SiNT) incelenmiştir. Bu sistemlerin yapısal, elastik

ve elektronik özellikleri analiz edilmiştir. Bu analizler sonucunda bazı tipteki GM atomlarını soğurmuş SiNT'lerin oda sıcaklığının üzerinde yarı-metalik karakter gösterebileceği bulunmuştur. Yüksek GM dekorasyonlarında, ferromanyetik SiNT'ler iki spin yönü içinde metalik olmakta ama E_F yakınlarında yine de yüksek spin kutuplaşması elde edilebilmektedir. Spine bağlı bu özellikler, yarıçap, GM tipi, dekorasyon gibi parametrelerle oynayarak değiştirilebilmektedir.

Elde ettiğimiz bu sonuçların, nanoyapıların spintronik uygulamaları üzerine yapılan çalışmalara ışık tutması umulmaktadır.

Anahtar sözcükler: İlk prensipler, ab initio, yoğunluk fonksiyoneli kuramı, spintronik, nanobilim, nano-malzemeler, yarım metal, spin vanası, dev manyeto direnç.

Acknowledgement

I would like to express my deepest gratitude and respect to my supervisor Prof. Dr. Salim ıracı for his patience and guidance during my study. During 5 years of working period, he was interested in not only my scientific studies but also my personal problems like a father. He is the one who makes me feel that I could be successful in this field. He also showed me how to be a real scientist. After a long, busy and efficient research duration, I will really miss to work with him and fell lonely without his guidance.

I would like to thank Dr. Tuğrul Senger for his help, support and friendship. I will always remember the days that we work together and the good times that we share during conference visits.

I appreciate Dr. Ceyhun Bulutay and Dr. Mehmet Bayındır for their motivation and interest. Being a Galatasaray fan, I believe that Dr. Bulutay is especially happy that I am taking my degree during the 100th year anniversary of Fenerbahe.

I am also thankful to my partner and my friend Haldun Sevinli for his help, motivation, and friendship. It is pleasure for me to work with him and I fell happy to drift him to the "dark side" of the field.

I will never forget my ex-partners and friends, Sefa Dağ, Sefaattin Tongay, and Yavuz Öztürk. We are now separated and living on different places on earth but our friendship will never ends.

I would like to thank my friends Deniz akır, Barış Öztop, Sevil Özer, Cem Sevik, Onur Umucalılar, Emre Taşgın, Turgut Tut, Sevilay Sevinli, Ceyda Sanlı, Müge Yüksel, Levent Subaşı, Rasim Volga Ovalı, Mehrdad Atabak, Aşkın Kocabaş, Koray Aydın, Duygu Can, Hasan Şahin, Hakan Kıymazaslan, Bahar Kop, Sinem Binicioğlu and all the others that I cannot write their names. I feel really sorry that I am leaving from you. I will always remember the good and hard times that we shared together and I hope our friendship will last life time.

I am thankful to our new, young group members and my crown princes, Seymur Cahangirov, Can Ataca and Mehmet Topsakal. They will carry the flag from now on and I wish them a great success during their carrier.

I also appreciate Derya Karadeniz, Ekin Fiteni, Itır akır, Emine Abla, Tahir Poyraz, Ali Rıza Arısoy and all the others for their help and making like easier for me.

I would like to thank my only brother Emin, his wife zlem and my little niece Damla for their love and support.

I bless to my mother Makbule and father Muhlis Durgun for their endless love and trust. I cannot achieve this point without their motivation and support. Dad and Mom, I would like to thank you once again for everything you did for me.

I would also thank my new family; my mother-in-law Beşire, father-in-law Bülent Menteşođlu and my sisters-in-law iđdem, Neyzar, and Ayşenur.

And finally, I am thankful to my dear wife, Gölçin without whom everything would be meaningless.

Contents

1	Introduction	1
1.1	History and Current Status	3
1.2	New Materials for Spintronics Applications	7
2	Methodology	10
2.1	Born-Oppenheimer Approximation	11
2.2	The Electronic Problem	11
2.3	Density Functional Theory	13
2.3.1	Hohenberg-Kohn Formulation	13
2.3.2	Kohn-Sham Equations	14
2.4	Functionals for Exchange and Correlation	15
2.4.1	Local Spin Density Approximation (LSDA)	15
2.4.2	Generalized Gradient Approximation (GGA)	16
2.4.3	LDA+U	17
2.5	Periodic Supercells	18

<i>CONTENTS</i>	xi
2.5.1 Bloch's Theorem	18
2.5.2 k-point Sampling	19
2.5.3 Plane-wave Basis Sets	19
2.5.4 Plane-wave Representation of Kohn-Sham Equations	20
2.5.5 Local-Basis Sets	20
2.5.6 Non-periodic Systems	21
2.6 Pseudopotential Approximation	21
2.6.1 Ultrasoft Pseudopotential	22
2.6.2 Projector Augmented Waves	23
2.7 Electronic Transport	23
2.8 Methodology and Parameters Used in the Calculations	25
2.8.1 Convergence Tests	26
2.8.2 Stability: Molecular Dynamics and Transition State Analysis	27
3 Carbon Linear Chains	29
3.1 Methodology	30
3.2 Atomic Structure	31
3.2.1 Binding energy and stability	31
3.2.2 Ab-initio molecular dynamics calculations	34
3.2.3 Breaking strength of the atomic chains	34
3.3 Magnetic Properties	35

3.3.1	A tight-binding model	41
3.3.2	Asymmetric atomic chains	46
3.4	Electronic properties	47
3.4.1	Effect of strain	47
3.4.2	Half-metallic properties	47
3.5	Transport properties	52
4	Single-Wall Carbon Nanotubes	59
4.1	Methodology	61
4.2	TM-wires adsorbed on SWNT	62
4.2.1	External adsorption	64
4.2.2	Internal adsorption	70
4.2.3	Other type of SWNTs	72
4.2.4	Adsorption on finite tubes	73
5	Silicon Nanowires	76
5.1	Methodology	77
5.2	Bare and H-passivated Si Nanowires	77
5.2.1	Atomic Structure and energetics	78
5.2.2	Elastic properties	80
5.2.3	Stability analysis	83
5.2.4	Energy band structure	84

5.3	Functionalization of SiNWs by Transition Metal Atoms	85
5.3.1	Curie Temperature	90
5.3.2	LDA+U	91
5.3.3	High TM Coverage of SiNWs	92
6	Conclusions	94
7	Publications of the Author	97
7.1	Refereed Journals (SCI)	97
7.2	Conference Proceedings	100
7.3	Non-SCI Journals	100
7.4	Popular Magazine	100

List of Figures

1. 1	Illustration of electron tunnelling in ferromagnet / insulator / ferromagnet (F/I/F) tunnel junctions: (a) Parallel and (b) antiparallel orientation of magnetizations with the corresponding spin resolved density of the d states in ferromagnetic metals that have exchange spin splitting Δ_{ex} . Arrows in the two ferromagnetic regions are determined by the majority-spin subband. Dashed lines depict spin conserved tunnelling.	4
1. 2	(a)Spin-valve (b)Magnetic tunnel junction	5
1. 3	(a)-(b) GMR isolator and (c)-(d) MRAM	6
2. 1	A molecule in a supercell geometry.	21
2. 2	Comparison of a wavefunction in the Coulomb potential of the nucleus (dashed) to the one in the pseudopotential (solid). The real (dashed) and the pseudo wavefunction and potentials (solid) match above a certain cutoff radius r_c	22
2. 3	A conductor or device (C) which is connected to the leads L and R.	23
2. 4	The total energy (E_T) variation as a function of cutoff energy (E_{cut}) for single Co atom (left panel) and Co bulk crystal (right panel). The results are obtained by PAW potential.	26

2. 5 Variation of energy, E_T , for the transition from the linear C_5Cr to the C_5+Cr state. $Q_{1\rightarrow 2}$ and $Q_{2\rightarrow 1}$ are energy barriers involved in the transitions. Zero of energy is taken relative to the free Cr atom and free periodic C-linear chain. 28
3. 1 Energetics of the formation of CoC_7Co and CrC_7Cr atomic chains. Left panels correspond to a TM atom attaching to the left free-end of the bare carbon chain; right panels are for the binding of a TM atom to the other end of the TM- C_n chain. The total energy of the system for $d \rightarrow \infty$ is set to zero in each panel. 32
3. 2 Optimized interatomic distances (in Å) of TM- C_n -TM atomic chains in their ferromagnetic (left column) and antiferromagnetic (right column) states. (a) CoC_nCo ; (b) CrC_nCr 33
3. 3 Optimized total energy (continuous line) and tensile force (dashed line) versus strain of CrC_3Cr and CrC_4Cr atomic chains. The chain breaks for strain values exceeding the critical point corresponding to the maximum of the force curve indicated by arrows. The total energies in equilibrium are set to zero. 35
3. 4 The decay of the exchange interaction strength between the Cr atoms in CrC_nCr as a function of their separation d . The curves are the best fits to the $\Delta E_{F\rightarrow AF}$ values in the form $\sim d^a$ 38
3. 5 The energy difference of the AF and the lowest-energy F states, $\Delta E_{F\rightarrow AF} = E_T(AF) - E_T(F)$ versus the number n of carbon atoms in the chain for different 3d transition metal elements. 40

3. 6 (a) Variation of the atomic magnetic moments in the TM-C₄-TM atomic chains in their ground (top panels) and excited (down panels) states. Left (right) panels are for TM = Co (TM = Cr). (b) From top to bottom: Variation of spin-up $\rho \uparrow$ and spin-down charge $\rho \downarrow$ densities, atomic magnetic moments, and change in total valance charge $\Delta\rho$ in the TM-C₁₅-TM atomic chains. Again, left (right) panels are for TM = Co (TM = Cr). 42
3. 7 Schematic electronic configuration of a TM-C_n-TM structure in an AF state. TM-sites have different onsite energies than the C-sites, and the hopping terms are dependent on the magnetic ordering. The energy cost for a spin-up electron of the first C-site to hop to the first TM-site is different from the energy cost for a spin-down electron to do the same hopping. The energy costs are reversed between the spins of the n^{th} C-site where they are identical for each spin for hopping between different C-sites. 44
3. 8 Energy difference of the AF and the lowest FM states in the CoC_nCo and CrC_nCr atomic chains within the Hückel-type model. 46
3. 9 Left panels: Spin-dependent total density of states of the periodic infinite (CrC₃)_∞ and (CrC₄)_∞ atomic chains. Right panels: Same for the (CoC₃)_∞ and (CoC₄)_∞. The Fermi energy is set to zero in all systems. 49
3. 10(a) Energy band structure of C₃Cr; corresponding total density of states (TDOS) for majority (\uparrow) and minority (\downarrow) spins; orbital projected local density of states at Cr atom (PDOS/Cr), at C atoms first nearest neighbor to Cr (PDOS/C1). (b) C₄Cr. State densities with s, p, d orbital symmetry in PDOSs are shown by thin continuous, dotted, broken lines, respectively. Zero of energy is set at E_F . Metallic band crossing the Fermi level, highest valence and lowest conduction bands are labelled by m, v_1 and c_1 , respectively. 51

3. 11 Energy band structures and charge densities of selected states. (a) $(\text{C}_3\text{Co})_\infty$ compound. Semiconducting majority spin (\uparrow) bands are shown in the left panel by continuous lines. The metallic minority spin (\downarrow) bands are presented in the right panel by dotted lines along the Γ -Z. Electron charge density plots of selected states are shown in small side-panels. The lobes of Co-3d and C-2p orbitals are clearly seen. (b) Same for the $(\text{C}_4\text{Co})_\infty$ linear chain. 53
3. 12 Total density of majority (\uparrow) and minority (\downarrow) spin states in arbitrary units. (a) $(\text{C}_3\text{Co})_\infty$ compound. The density (DOS) of the majority spin states has a band gap and the Fermi level is close to the conduction band edge. The density of minority spin states is high at the Fermi level. These states are derived from the Co-3d and C-2p orbitals. (b) Same for the $(\text{C}_4\text{Co})_\infty$ compound. The insets show that the metallic states at E_F are derived from the 3d-states of Co atom. (c) DOSs calculated for $(\text{C}_3\text{Co})_m$ chains show how the electronic structure of the infinite-periodic chain ($m = \infty$) develops from those of the finite-length chains (i.e. $m = 1, 3, 5$) as m increases. 54
3. 13 Conductance versus energy for the CrC_nCr ($n = 3 - 5$) atomic chains between two infinite gold electrodes. The left (right) panels are for the ground (excited) magnetic states of the structures. The Fermi levels are set to zero. 55
3. 14 Conductance versus energy for the CoC_nCo ($n = 3 - 5$) atomic chains between two infinite gold electrodes. The left (right) panels are for the ground (excited) magnetic states of the structures. The Fermi levels are set to zero. 56
3. 15 Spin polarized conductance of CrC_4Cr molecular spin-valve device when connected to semi-infinite Au electrodes. The insets show the molecular energy levels of the isolated chains. 58

4. 1	The configuration of adsorbed transition metal (TM) atoms (Co, Cr, Fe, Mn, and V) forming chain structures on the (8,0) SWNT are illustrated for various coverage geometries, such as $\theta=1/2$, 1, 2 and 4.	61
4. 2	The spin-dependent band structure and total density of states (TDOS) of V, Co and Fe-chains adsorbed on the zigzag (8,0) SWNT for $\theta=1/2$, 1 and 2 geometries. Solid and dotted lines are for majority and minority spin states, respectively. The zero of energy is set to the Fermi level E_F	63
4. 3	The spin-dependent band structure and total density of states (TDOS) of Mn and Cr-chains adsorbed on the zigzag (8,0) SWNT for $\theta=1/2$, 1 and 2 geometries. Solid and dotted lines are for majority and minority spin states, respectively. The zero of energy is set to the Fermi level E_F	68
4. 4	The variation of magnetic moment, μ (a), and the binding energy, E_b (b) as a function of number of d -states for $\theta=1/2$, 1, and 2 for external adsorption.	70
4. 5	Variation of the average magnetic moment μ and binding energy E_b of Fe-chain adsorbed on the external walls of zigzag ($n,0$) SWNT ($n=6, 8$, and 9) with the coverage geometry θ and tube index n . (a) μ versus θ ; (b) E_b versus θ ; (c) E_b versus n	72

4. 6 Left panels: The number of states and corresponding structures of Fe atoms adsorbed on a finite (8,0) SWNT with open but fixed ends for (a) $\theta = 1/2$ (i.e 64 carbon atoms + one Fe), (b) $\theta = 1$ (i.e 64 carbon atoms + 2 Fe), and (c) $\theta = 2$ (i.e 128 carbon atoms + 8 Fe). The zero of energy is set to the Fermi level E_F . The total net magnetic moment for each finite tube, μ is shown. Total density of states of majority and minority spin states of infinite and periodic systems are also shown by continuous lines for $\theta=1/2, 1,$ and 2. Right panels: Atomic configurations of Fe atoms adsorbed on the finite size (8,0) SWNT with closed ends. (d) One Fe atom is adsorbed on a tube consisting of 96 carbon atoms. (e) Two Fe atom are adsorbed on a tube consisting of 96 carbon atoms. (f) Eight Fe atoms are adsorbed on a tube of consisting of 160 carbon atoms. The calculated total magnetic moments μ_T and TDOS of majority and minority spin states are illustrated for each configuration. 73

5. 1 Upper panels: Top and side views of optimized atomic structures of bare SiNW(N)grown along [001] direction. Lower panels: Same for H-SiNW(N) with N=21, 25, 57, 61 and 81. Large and small balls indicate Si and H atoms, respectively. Side views consist of two primitive unit cells. 78

5. 2 Distribution of interatomic distances of structure-optimized bare SiNW(N) (bottom curve in each panel) and H-SiNW(N) (middle curve) for N=21, 57 and 81. Upper curve with numerals indicate first, second, third, fourth etc nearest neighbor distances calculated for bulk Si crystal in equilibrium. 81

5. 3 Distribution of interatomic distances of structure-optimized bare SiNW(N) (bottom curve in each panel) and H-SiNW(N) (middle curve) for N=25 and 61. Upper curve with numerals indicate first, second, third, fourth etc nearest neighbor distances calculated for bulk Si crystal in equilibrium. 82

5. 4	Variation of elastic strength (Young's modulus) κ with number of atoms N in the primitive unit cell of the bare and hydrogen terminated SiNW(N)s. Wires with $N=21$, 57 and 81 have round cross section, whereas wires with $N=25$ and 61 have square-like cross section.	83
5. 5	Energy band structures of SiNW(N) for $N=21$, 25, 57, 61. 81. Shaded area is the band gap. Zero of band energies are set at the Fermi level.	84
5. 6	Energy band structures of H-SiNW(N) for $N=21$, 25, 57, 61. 81. Shaded area is the band gap. Zero of band energies are set at the Fermi level.	85
5. 7	Top and side views of optimized atomic structures of single TM atom adsorbed H-SiNW (per primitive cell, $n = 1$). Binding energies in regard to the adsorption of TM atoms, i.e. E_B , E'_B for $n = 1$ are defined in the text. μ denotes the net magnetic moment per primitive unit cell. Small, large-light and large-dark balls represent H, Si and TM atoms, respectively.	86
5. 8	Band structure and spin-dependent total density of states (TDOS) for $N=21$, 25 and 57. Left panels: Semiconducting H-SiNW(N). Middle panels: Half-metallic H-SiNW(N)+TM. Right panels: Density of majority and minority spin states of H-SiNW(N)+TM. Bands described by continuous and dotted lines are majority and minority bands. Zero of energy is set to E_F	88
5. 9	The energy band structure variation of H-SiNW(21)+Co (up panel), H-SiNW(25)+Cr (mid-panel) and H-SiNW(57)+Cr (down panel) with respect to U value.	91

5. 10 Side views of optimized atomic structures of H-SiNWs covered by n TM atoms. \bar{E}_B , \bar{E}'_B are average binding energy values for $n > 1$ and are defined in the text. μ denotes the net magnetic moment per primitive unit cell. Small, large-light and large-dark balls represent H, Si and TM atoms, respectively. 92
5. 11 $D(E, \downarrow)$, density of minority (light) and $D(E, \uparrow)$, majority (dark) spin states. (a) H-SiNW(25)+Cr, $n = 8$; (b) H-SiNW(57)+Cr, $n = 8$. P and μ indicate spin-polarization and net magnetic moment (in Bohr magnetons per primitive unit cell), respectively. 93

List of Tables

3.1	The energy difference of the AF and the lowest-energy F states, $\Delta E_{F \rightarrow AF} = E_T(AF) - E_T(F)$ in eV, and the magnetic moment μ of the ground state in units of Bohr magneton μ_B . For cases with AF ground states the moment corresponding to the lowest-energy F state is given in parenthesis.	37
3.2	Variation of electronic and magnetic properties of TM- C_n -TM chains under axial strain ε . $\Delta E_{F \rightarrow AF}$ is the energy difference of the AF and the lowest energy F states given in eV. μ is the magnetic moment in units of μ_B . E_g^σ is the energy difference in eV between the lowest unoccupied and highest occupied molecular orbitals for spin type σ	48
4.1	The distance between TM and nearest C atom d_{C-TM} ; average binding energy E_b ; average magnetic moments per atom μ ; spin-polarization at the Fermi level $P(E_F)$ for chain structures of Co, Cr, Fe, Mn, and V transition metal atoms adsorbed on the (8,0) SWNT for $\theta = 1/2, 1$, and 2. $P(E_F) <$ corresponds to $D(E_F, \downarrow) > D(E_F, \uparrow)$	62

4.2	The distance between TM and nearest neighbor C atom d_{C-TM} ; binding energy E_b ; magnetic moments μ per TM atom; polarization at Fermi level $P(E_F)$ of various chain structures of Co, Fe, and V atoms adsorbed inside the (8,0) SWNT for $\theta = 1/2$ and $\theta=1$. $P(E_F) <$ corresponds to $D(E_F, \downarrow) > D(E_F, \uparrow)$	72
5.1	The binding energies (in eV) with respect to atomic and bulk energies of various metals.	79
5.2	The binding energies (in eV) with respect to atomic and bulk energies of various metals.	79

Chapter 1

Introduction

Until recently, the spin of the electron was largely ignored in charge-based electronics. A new technology where the electron spin carries information instead of its charge is now emerging. This spin-based electronics is called spintronics.

Spintronics [1, 2, 3] is a multidisciplinary field whose aim is the manipulation of spin degree of freedom in solid-state systems. In this concept, the term spin stands for either the spin of a single electron \mathbf{s} , which can be detected by its magnetic moment $-g\mu_B\mathbf{s}$ (where μ_B is the Bohr magneton and g is the electron g -factor), or the average spin of an ensemble of electrons. The control of spin is then a control of either the population and the phase of the spin of particles, or a coherent spin manipulation of a single or a few-spin system. This offers opportunities for a new generation of devices combining standard microelectronics with spin-dependent effects.

The goal of spintronics is to understand the interaction between the particle spin and its environment and to make useful devices using this knowledge. Fundamental studies of spintronics include generation of spin polarization and investigations of spin transport in electronic materials, as well as of spin dynamics and spin relaxation.

Generation of spin polarization usually means creating a non-equilibrium spin

population. While this can be achieved in several ways, electrical spin injection is more desirable for device applications. In electrical spin injection a magnetic electrode is connected to the sample.

When the current drives spin-polarized electrons from the electrode to the sample, non-equilibrium spin accumulates there. The rate of spin accumulation depends on spin relaxation. The spin relaxation is the process of bringing the accumulated spin population back to equilibrium. Typical time scales for spin relaxation in electronic systems are measured in nanoseconds, while the range is from picoseconds to microseconds. Spin detection relies on sensing the changes in the signals caused by the presence of non-equilibrium spin in the system. The objective in many spintronic devices is to maximize the spin detection sensitivity. At this point the changes in the spin states (not the spin itself) are detected.[3]

Traditional approaches to use spin are based on the alignment of a spin (either up or down) relative to a reference (an applied magnetic field or magnetization orientation of the ferromagnetic material). Device operations then proceed with electrical current that depends in a predictable way on the degree of alignment. Adding the spin degree of freedom to conventional charge-based electronics or using the spin degree of freedom alone will add more capability and performance to electronic products. The advantages of these new devices would be nonvolatility, increased data processing speed, decreased electric power consumption, and increased integration densities compared with conventional semiconductor devices.

Major challenges in the field that are addressed by both experiment and theory include the optimization of electron spin lifetimes, the detection of spin coherence in nanoscale structures, transport of spin-polarized carriers across relevant length scales and interfaces, and the manipulation of spin on sufficiently fast time scales. It is seen that the merging of electronics, photonics, and magnetics will ultimately lead to new spin-based multifunctional devices such as spin-FET (field effect transistor), spin-LED (light-emitting diode), spin RTD (resonant tunneling device), optical switches operating at terahertz frequency, modulators, encoders, decoders, and quantum bits for quantum computation and communication. The success of these efforts depends on a deeper understanding of fundamental spin

interactions in materials as well as the roles of dimensionality, defects, etc. in modifying these dynamics. If we can understand and control the spin degree of freedom in solid-state systems, the potential for high-performance spin-based electronics will be excellent.

1.1 History and Current Status

In a pioneering work, Mott [4] provided a basis for understanding of spin-polarized transport. Mott sought an explanation for an unusual behavior of resistance in ferromagnetic metals. He realized that at sufficiently low temperatures electrons of majority and minority spin, with magnetic moment parallel and antiparallel to the magnetization of a ferromagnet, respectively, do not mix in the scattering processes. The conductivity can then be expressed as the sum of two independent and unequal parts for two different spin projections. It suggests that the current in ferromagnets is spin polarized. This is also known as the two-current model and it provides an explanation for various magnetoresistive phenomena.[5]

Tunneling measurements played a key role in early experimental work on spin-polarized transport. Studying N/F/N junctions, where N was a nonmagnetic metal and F was a ferromagnetic semiconductor [6], revealed that I-V curves could be modified by an applied magnetic field.[7] When unpolarized current is passed across a ferromagnetic semiconductor, the current becomes spin-polarized.[8]

Julliere [9] measured tunnelling conductance of F/I/F junctions, where I was an amorphous Ge. Julliere formulated a model for a change of conductance between the parallel ($\uparrow\uparrow$) and antiparallel ($\uparrow\downarrow$) magnetization in the two ferromagnetic regions F1 and F2, as depicted in Fig. 1. 1. The corresponding tunnelling magnetoresistance (TMR) is defined as

$$TMR = \frac{\Delta R}{R_{\uparrow\uparrow}} = \frac{R_{\uparrow\downarrow} - R_{\uparrow\uparrow}}{R_{\uparrow\uparrow}} = \frac{G_{\uparrow\uparrow} - G_{\uparrow\downarrow}}{G_{\uparrow\downarrow}} \quad (1. 1)$$

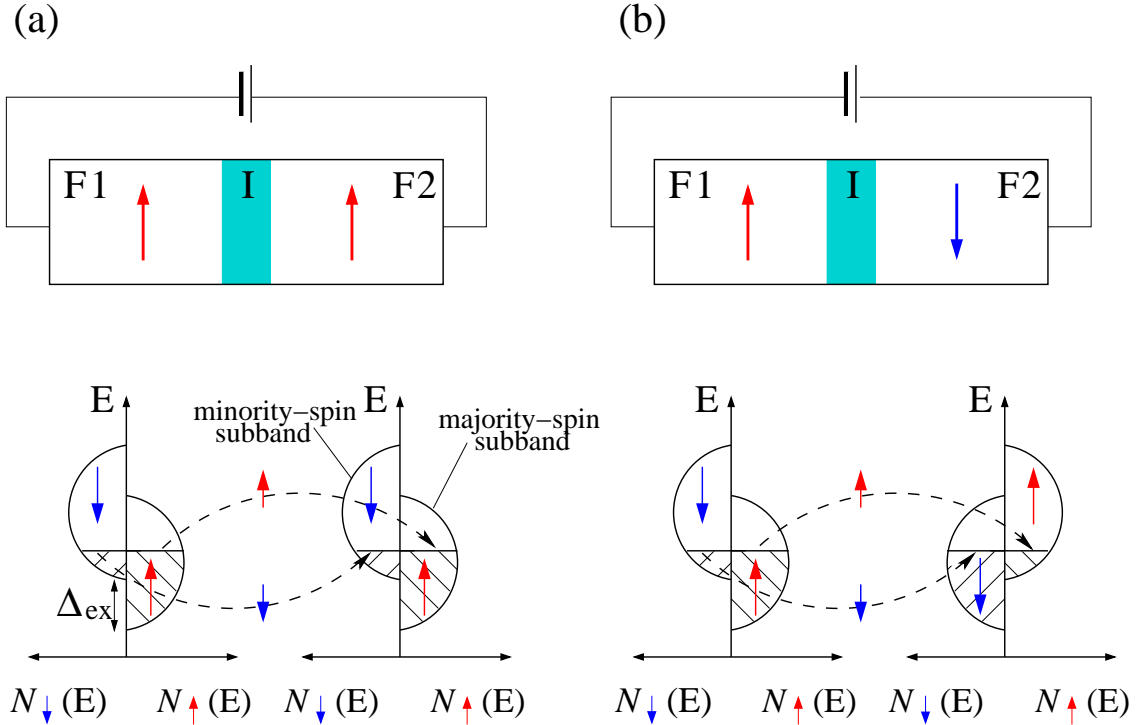


Figure 1. 1: Illustration of electron tunnelling in ferromagnet / insulator / ferromagnet (F/I/F) tunnel junctions: (a) Parallel and (b) antiparallel orientation of magnetizations with the corresponding spin resolved density of the d states in ferromagnetic metals that have exchange spin splitting Δ_{ex} . Arrows in the two ferromagnetic regions are determined by the majority-spin subband. Dashed lines depict spin conserved tunnelling.

where conductance G and resistance $R = 1/G$ are labelled by the relative orientations of the magnetizations in F1 and F2. It is possible to change the relative orientations, between $\uparrow\uparrow$ and $\uparrow\downarrow$, even at small applied magnetic fields. TMR is a magnetoresistance effect where the electrical resistance changes in the presence of an external magnetic field. While the early results of Julliere were not confirmed, TMR at 4.2 K was observed using NiO as a tunnel barrier.[10]

The discovery of the giant magnetoresistive effect (GMR) [11] in 1988 is considered as the beginning of the spin-based electronics. GMR is observed in artificial thin-film materials composed of alternate ferromagnetic and nonmagnetic layers. The resistance of the material is lowest when the magnetic moments in ferromagnetic layers are aligned and highest when they are anti-aligned. The term "giant" reflected the magnitude of the effect (more than $\sim 10\%$), as compared to

the better known anisotropic magnetoresistance ($\sim 1\%$). In such magnetic superlattice structures, the magnetization of the layers are coupled to each other by an indirect exchange interaction mediated by the electrons of the spacer layer.[12, 13] The interlayer exchange coupling and the magnetoresistance are found to be oscillating as a function of the spacer thickness, and the interaction amplitude decays proportional to the inverse square of the spacer thickness. [14, 15, 16] Recently fabricated materials operate even at room temperature and exhibit substantial changes in resistivity when subjected to relatively small magnetic fields.

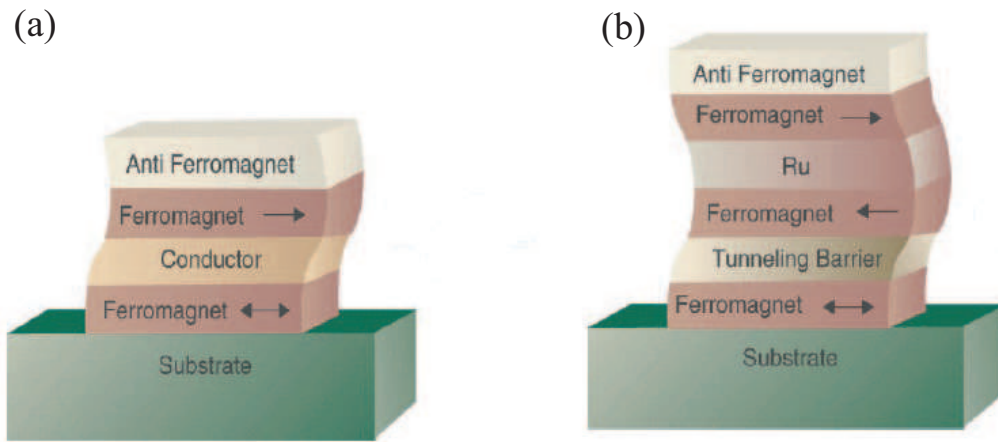


Figure 1. 2: (a)Spin-valve (b)Magnetic tunnel junction

The prediction of Julliere's model also illustrates the spin-valve effect which is later discovered in structures displaying GMR. A spin-valve suggests that the resistance of a device can be changed by manipulating the relative orientation of the magnetizations.

A spin-valve (Fig. 1. 2a) which is a GMR-based device, has two ferromagnetic layers sandwiching a thin nonmagnetic metal, with one of the two magnetic layers being pinned which means the magnetization in that layer is insensitive to moderate magnetic fields. The other magnetic layer is called the free layer, and its magnetization can be changed by application of a relatively small magnetic field. As the magnetizations in the two layers change from parallel to antiparallel alignment, the resistance of the spin-valve rises typically from 5 to 10 %. Pinning is usually accomplished by using an antiferromagnetic layer that is in intimate contact with the pinned magnetic layer.

A magnetic tunnel junction (MTJ) [17] (Fig. 1. 2b) is a device in which a pinned layer and a free layer are separated by a very thin insulating layer. The tunneling resistance is modulated by magnetic field in the same way as the resistance of a spin valve is and it exhibits 20 to 40 % change in the magnetoresistance. Because the tunneling current density is usually small, MTJ devices tend to have high resistances.

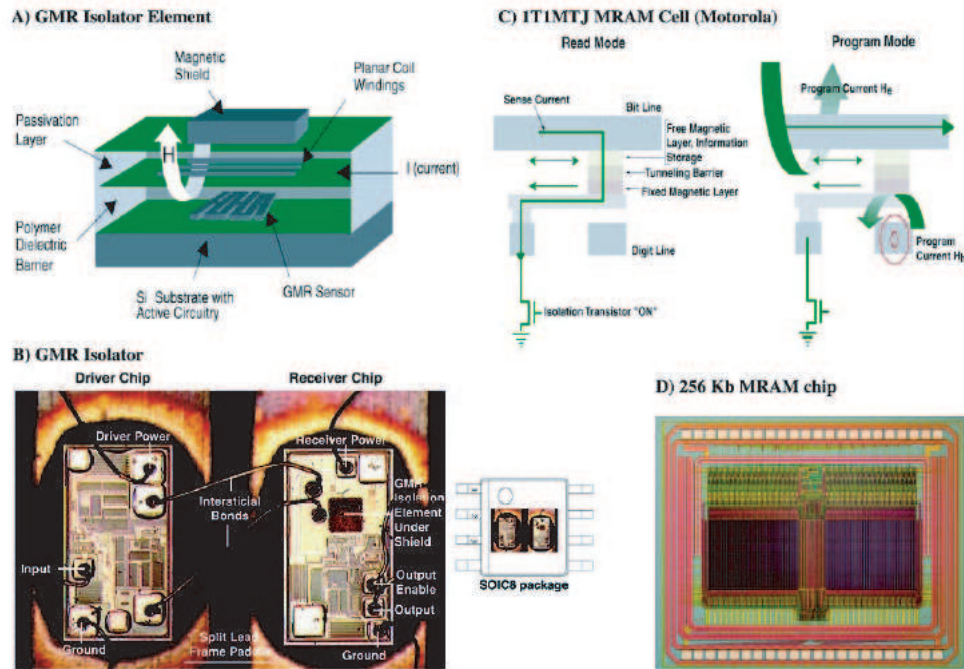


Figure 1. 3: (a)-(b) GMR isolator and (c)-(d) MRAM

GMR and MTJ structures are used in various applications. Important ones include magnetic field sensors, read heads for hard drives, galvanic isolators, and magnetoresistive random access memory (MRAM). GMR spin valve read heads are dominating applications in hard drives. Although some alternative configurations have been proposed, nearly all commercial GMR heads use the spin valve format as originally proposed by IBM.[18] The GMR-based galvanic isolator (Fig. 1. 3) is a combination of an integrated coil and a GMR sensor on an integrated circuit chip. GMR isolators introduced in 2000 eliminate ground noise in communications between electronics blocks. The GMR isolator is ideally suited for integration with other communications circuits and the packaging of a large number of isolation channels on a single chip. The speed of the GMR

isolator is currently 10 times faster than today's optoisolators and can eventually be 100 times faster. The principal speed limitations are the switching speed of the magnetic materials and the speed of the associated electronics.

MRAM uses magnetic hysteresis to store data and magnetoresistance to read data. GMR-based MTJ [19] memory cells are integrated on an integrated circuit chip and function like a static semiconductor RAM chip. Additionally, the data are also retained when the power is off. Potential advantages of the MRAM compared with silicon electrically erasable programmable read-only memory (EEPROM) and flash memory are 1000 times faster write times, no wearout with write cycling (EEPROM and flash wear out with about 1 million write cycles), and lower energy for writing. MRAM data access times are about 1/10000 that of hard disk drives. MRAM is not yet available commercially, but production of MRAM is anticipated in few years.

1.2 New Materials for Spintronics Applications

The search for materials combining properties of the ferromagnet and the semiconductor is a long-standing goal. There are continuing efforts in improving issues in materials fabrication and device design. One of the approaches is to search for new materials that exhibit large carrier spin polarization. Candidates include special class of materials, so called half-metallic ferromagnets (HM) [20, 21]. HMs show metallic character for one spin direction and possess a band gap for other spin direction and achieve perfect (100 %) spin polarization at Fermi level. Four types of HMs are predicted so far: oxide compounds [22, 23] (*e.g.*, rutile CrO_2 and spinel Fe_3O_4), perovskites [24] (*e.g.*, $(\text{La,Sr})\text{MnO}_3$), Zinc-blende compounds [25] (*e.g.*, CrAs) and Heusler alloys [20] (*e.g.*, NiMnSb). Zinc-blende HM with high magnetic moment μ and high Curie temperature $T_c > 400\text{K}$ (such as CrAs and CrSb in ZB structure) have been grown in thin-film forms [25] and half-metallic graphene nanoribbons are theoretically predicted.[26]

With the advent of nanotechnology fabrication of quantum structures with dimensions of the order of molecular and atomic sizes became accessible, and analogous magnetoresistive properties are studied in 1D geometry. Fundamental spin-dependent electron transport properties have been demonstrated in the context of molecular spintronics [27, 28, 29, 30, 31, 32] which is a promising field of research in basic science and potential applications. Even the ultimately thin wires made of single atomic chains are produced under experimental conditions and are actively studied. These nanowire systems include atomic chains of both metal and transition metal elements such as Al, Au, Cr, Fe, etc., as well as C and Si atomic chains which also exhibit metallic properties.[33, 34, 35, 36, 37, 38, 39, 40, 41, 42, 43] Carbon chains in this respect are promising, since carbon has a strong tendency to form linear atomic chains, whereas other elements tend to make zigzag chains and they are more vulnerable to clustering.[41, 42, 43] Much recently, finite or periodic forms of TM monatomic chains have been subject of various theoretical studies. The atomic structure, magnetic and transport properties of these chains have been investigated.[44, 45, 46, 47]

Carbon nanotubes [48, 49] which are novel nanostructures with unique physical properties are other promising materials. Long-ranged indirect exchange coupling between magnetic impurities on carbon nanotubes are already introduced [50, 51], and this property can be exploited in future spintronic devices. Electric field control of spin transport [52] and coherent transport of electron spin in a ferromagnetically contacted carbon nanotube [53] is experimentally reported.

Rod-like, oxidation resistant Si nanowires (SiNW) can now be fabricated at small diameters [54] (1-7 nm) and display diversity of interesting electronic properties. In particular, the band gap of semiconductor SiNWs varies with their diameters. They can be used in electronic and optical applications like field effect transistors [55] (FETs), light emitting diodes [56], lasers [57] and interconnects. Room temperature ferromagnetism is already discovered in Mn⁺-doped SiNW.[58] Once combined with advanced silicon technology, SiNW can be a potential material with promising nanoscale technological applications in spintronics and magnetism.

In this context first-principles studies of carbon and silicon based nanostructures that can produce spin polarization effects are important. The main purpose of this study is to model and predict new nanomaterials which possess interesting spintronics properties when they are functionalized. The structural, electronic, magnetic and transport properties of these materials are systematically analyzed and possibility of real device applications are discussed.

The organization of the thesis is as follows : After Introduction part, the theory and methodology used in calculations is briefly discussed in Chapter 2 by leaving details to related references. The GMR effect and half-metallicity in carbon linear chains is studied in Chapter 3. The spintronic properties of functionalized single-wall carbon nanotubes and silicon nanowires are analyzed in Chapter 4 and Chapter 5, respectively. In Chapter 6 as a Conclusion part, the obtained results are briefly summarized.

Chapter 2

Methodology

Understanding the physical and chemical properties of matter in any phase and in any form is a complex and advanced many-body problem. In all cases the system can be described by a number of nuclei and electrons interacting through electrostatic interactions. In principle all the properties can be derived by solving the many-body Schrödinger equation:

$$\widehat{H}\Psi_i(\mathbf{r}, \mathbf{R}) = E_i\Psi_i(\mathbf{r}, \mathbf{R}) \quad (2. 1)$$

The Hamiltonian of a many body system can be written in a general form:

$$H = \sum_{I=1}^N \frac{\overrightarrow{P}_I^2}{2M_I} + \sum_{i=1}^{N_e} \frac{\overrightarrow{p}_i^2}{2m} + \sum_{i>j} \frac{e^2}{|\overrightarrow{r}_i - \overrightarrow{r}_j|} + \sum_{I>J} \frac{Z_I Z_J e^2}{|\overrightarrow{R}_I - \overrightarrow{R}_J|} - \sum_{i,I} \frac{Z_I e^2}{|\overrightarrow{R}_I - \overrightarrow{r}_i|} \quad (2. 2)$$

where $R = R_N$, $N = 1...N$, symbolizes N nuclear coordinates, and $r = r_{N_e}$, $i = 1...N_e$, are considered to be N_e electronic coordinates. Z_I 's are the nuclear charges and M_I 's are the N nuclear masses.

However, it looks like only one equation to deal with, in practice it is almost impossible to solve this problem exactly except for a few simple cases. This is a multi-component many-body system and Schrödinger equation cannot be easily decoupled into a set of independent equations because of electrostatic correlations between each component. One have to deal with $(3N_e + 3N)$ degrees of freedom to obtain a desired solution. As a result, approximation methods should be derived to achieve reliable and satisfies outcome.

2.1 Born-Oppenheimer Approximation

Due to the small mass of electrons compared with mass of the nuclei, electrons move much faster. Thus electrons have the ability to follow the motion of the nuclei instantaneously, so they remain in the same stationary state of the electronic Hamiltonian all the time.[59] With these conditions, wave function can be factorized as follows:

$$\Psi(\mathbf{R}, \mathbf{r}, t) = \Theta(\mathbf{R}, t)\Phi(\mathbf{R}, \mathbf{r}) \quad (2. 3)$$

where nuclear wave function $\Theta(\mathbf{R}, t)$ obeys the time-dependent Schrödinger equation and electronic wave function $\Phi(\mathbf{R}, \mathbf{r})$ is the m -th stationary state of the electronic Hamiltonian. In spite of m can be any electronic eigenstate at least in principle, most of the cases consider $m=0$ or in other words ground state.

Assuming these approximations, we are left with the problem of solving the many-body electronic Schrödinger equation for fixed nuclear positions.

2.2 The Electronic Problem

Many-body electronic Schrödinger equation is still a very difficult problem to handle and exact solution is known only for some simple cases, such as free electron gas. At analytic level, one has to refer approximations.

In the very beginnings quantum mechanics (in 1928) first approximation method was proposed by Hartree.[60] It postulates that many-electron wave function can be written as product one-electron wave functions each of which satisfies one-particle Schrödinger equation in an effective potential.

$$\Phi(\mathbf{R}, \mathbf{r}) = \prod_i \varphi_i(\mathbf{r}_i) \quad (2. 4)$$

$$\left(-\frac{\hbar^2}{2m}\nabla^2 + V_{eff}^{(i)}(\mathbf{R}, \mathbf{r})\right)\varphi_i(\mathbf{r}) = \epsilon_i\varphi_i(\mathbf{r}) \quad (2. 5)$$

with

$$V_{eff}^{(i)}(\mathbf{R}, \mathbf{r}) = V(\mathbf{R}, \mathbf{r}) + \int \frac{\sum_{j \neq i}^N \rho_j(\mathbf{r}')}{|\mathbf{r} - \mathbf{r}'|} d\mathbf{r}', \quad (2. 6)$$

where

$$\rho_j(\mathbf{r}) = |\phi_j(\mathbf{r})|^2 \quad (2. 7)$$

is the electronic density associated with particle j . Effective potential does not include the charge density terms associated with i , in order to prevent self-interaction terms. In this approximation, the energy is given by:

$$E^H = \sum_i^N \varepsilon_n - \frac{1}{2} \int \int \frac{\rho(\mathbf{r})\rho(\mathbf{r}')}{|\mathbf{r} - \mathbf{r}'|} d\mathbf{r}d\mathbf{r}', \quad (2. 8)$$

where the factor 1/2 comes from the fact that electron-electron interaction is counted twice.

The coupled differential equations in 2. 5 can be solved by minimizing the energy with respect to a set of variational parameters in a trial wave function and then putting them back into 2. 6, and solving the Schrödinger equation again. This procedure, which is called self-consistent Hartree approximation, should be repeated until the self-consistency is reached.

To improve Hartree approximation, fermionic nature of electrons should be considered. Due to Pauli exclusion principle, two fermions, electrons in our case, cannot occupy the same state being all of their quantum numbers are the same. This suggests that total electron wave function should be in a antisymmetric form:

$$\Phi(\mathbf{R}, \mathbf{r}) = \frac{1}{\sqrt{N!}} \begin{pmatrix} \phi_1(\mathbf{r}_1) & \dots & \phi_1(\mathbf{r}_N) \\ \vdots & \ddots & \vdots \\ \phi_N(\mathbf{r}_1) & \dots & \phi_N(\mathbf{r}_N) \end{pmatrix} \quad (2. 9)$$

which is known as Slater determinant. This approximation is called Hartree-Fock (HF) and it explains particle exchange in an exact manner.[61, 62] It also provides a moderate description of inter-atomic bonding but many-body correlations are completely absent. Recently, the HF approximation is routinely used as a starting point for more advanced calculations.

Parallel to the development of electronic theory, Thomas and Fermi proposed, at about same time as Hartree, that the full electron density was the fundamental variable of the many-body problem, and derived a differential equation for the density without referring to one-electron orbitals. Although, this theory which is known as Thomas-Fermi Theory [63, 64], did not include exchange and correlation effects and was able to sustain bound states, it set up the basis of later development of Density Functional Theory (DFT).

2.3 Density Functional Theory

The initial work on DFT was reported in two publications: first by Hohenberg-Kohn in 1964 [65], and the next by Kohn-Sham in 1965 [66]. This was almost 40 years after Schrödinger (1926) had published his pioneering paper marking the beginning of wave mechanics. Shortly after Schrödinger's equation for electronic wave function, Dirac declared that chemistry had come to an end since all its content was entirely contained in that powerful equation. Unfortunately in almost all cases except for the simple systems like He or H, this equation was too complex to allow a solution. DFT is an alternative approach to the theory of electronic structure, in which the electron density distribution $\rho(\mathbf{r})$ rather than many-electron wave function plays a central role. In the spirit of Thomas-Fermi theory [63, 64], it is suggested that a knowledge of the ground state density of $\rho(\mathbf{r})$ for any electronic system uniquely determines the system.

2.3.1 Hohenberg-Kohn Formulation

The Hohenberg-Kohn [65] formulation of DFT can be explained by two theorems:

Theorem 1: The external potential($V(\mathbf{r})$) is univocally determined by the electronic density, except for a trivial additive constant.

Since $\rho(\mathbf{r})$ determines $V(\mathbf{r})$, then it also determines the ground state wave function and gives us the full Hamiltonian for the electronic system. Hence $\rho(\mathbf{r})$

determines implicitly all properties derivable from H through the solution of the time-dependent Schrödinger equation.

Theorem 2: (Variational Principle) The minimal principle can be formulated in terms trial charge densities, instead of trial wavefunctions.

The ground state energy E could be obtained by solving the Schrödinger equation directly or from the Rayleigh-Ritz minimal principle:

$$E = \min \frac{\langle \tilde{\Psi} | H | \tilde{\Psi} \rangle}{\langle \tilde{\Psi} | \tilde{\Psi} \rangle} \quad (2. 10)$$

Using $\tilde{\rho}(\mathbf{r})$ instead of $\tilde{\Psi}(\mathbf{r})$ was first presented in Hohenberg and Kohn. For a non-degenerate ground state, the minimum is attained when $\tilde{\rho}(\mathbf{r})$ is the ground state density. And energy is given by the equation:

$$E_V[\tilde{\rho}] = F[\tilde{\rho}] + \int \tilde{\rho}(\mathbf{r})V(\mathbf{r})d\mathbf{r} \quad (2. 11)$$

with

$$F[\tilde{\rho}] = \langle \Psi[\tilde{\rho}] | \hat{T} + \hat{U} | \Psi[\tilde{\rho}] \rangle \quad (2. 12)$$

where $\Psi[\tilde{\rho}]$ is the ground state of a potential \hat{U} which has $\tilde{\rho}$ as its ground state and $V(\mathbf{r})$ is the external potential. It should be noted that $F[\tilde{\rho}]$ is a universal functional which does not depend explicitly on $V(\mathbf{r})$.

These two theorems form the basis of the DFT. The main remaining error is due to inadequate representation of kinetic energy and it will be cured by representing Kohn-Sham equations.

2.3.2 Kohn-Sham Equations

There is a problem with the expression of the kinetic energy in terms of the electronic density. The only expression used until now is the one proposed by Thomas-Fermi, which is local in the density so it does not reflect the short-ranged, non-local character of kinetic energy operator. In 1965, W. Kohn and L. Sham [66] proposed the idea of replacing the kinetic energy of the interacting

electrons with that of an equivalent non-interacting system. With this assumption density can be written as

$$\rho(\mathbf{r}) = \sum_{s=1}^2 \sum_{i=1}^{N_s} |\varphi_{i,s}(\mathbf{r})|^2 \quad (2. 13)$$

$$T[\rho] = \sum_{s=1}^2 \sum_{i=1}^{N_s} \langle \varphi_{i,s} | -\frac{\nabla^2}{2} | \varphi_{i,s} \rangle \quad (2. 14)$$

where $\varphi_{i,s}$'s are the single particle orbitals which are also the lowest order eigenfunctions of Hamiltonian non-interacting system

$$\left\{ -\frac{\nabla^2}{2} + v(\mathbf{r}) \right\} \varphi_{i,s}(\mathbf{r}) = \epsilon_{i,s} \varphi_{i,s}(\mathbf{r}) \quad (2. 15)$$

Using new form $T[\rho]$ density functional takes the form

$$F[\rho] = T[\rho] + \frac{1}{2} \int \int \frac{\rho(\mathbf{r})\rho(\mathbf{r}')}{|\mathbf{r} - \mathbf{r}'|} d\mathbf{r}d\mathbf{r}' + E_{XC}[\rho] \quad (2. 16)$$

where this equation defines the exchange and correlation energy as a functional of the density. Using this functional in 2. 11, total energy functional is finally obtained which is known as Kohn-Sham functional [66]

$$E_{KS}[\rho] = T[\rho] + \int \rho(\mathbf{r})v(\mathbf{r})d\mathbf{r} + \frac{1}{2} \int \int \frac{\rho(\mathbf{r})\rho(\mathbf{r}')}{|\mathbf{r} - \mathbf{r}'|} d\mathbf{r}d\mathbf{r}' + E_{XC}[\rho] \quad (2. 17)$$

in this way we have expressed the density functional in terms KS orbitals which minimize the kinetic energy under the fixed density constraint. In principle these orbitals are a mathematical object constructed in order to render the problem more tractable, and do not have a sense by themselves. The solution of KS equations has to be obtained by an iterative procedure, in the same way of Hartree and Hartree-Fock equations.

2.4 Functionals for Exchange and Correlation

2.4.1 Local Spin Density Approximation (LSDA)

Kohn-Sham pointed out that solids can often be considered as close to the limit of the homogeneous electron gas. In that limit, the effects of exchange and correlation are local in character. In local density approximation (LDA) [67] or more

generally local spin density approximation (LSDA), the exchange-correlation is simply an integral over all space with the exchange-correlation energy density at each point assumed to be the same as in a homogeneous electron gas with that density,

$$E_{xc}^{LSDA}[\rho^\uparrow, \rho^\downarrow] = \int d^3r \rho(r) \epsilon_{xc}^{hom}(\rho^\uparrow(\mathbf{r}), \rho^\downarrow(\mathbf{r})) \quad (2.18)$$

The LSDA is the most general local approximation and is given explicitly for exchange and by approximate expressions for correlation. For unpolarized systems LDA is simply found by setting $\rho^\uparrow(\mathbf{r}) = \rho^\downarrow(\mathbf{r}) = \rho(\mathbf{r})/2$.

Once one has made the local ansatz of the L(S)DA, then all the rest follows. Since the functional E_{xc} is universal, it follows that it is exactly the same as for the homogeneous gas. The only information needed is the exchange-correlation energy of the homogeneous gas as a function of density.

The rationale for the local approximation is that for the densities typical of those found in solids where the range of effects of exchange and correlation is rather short. It is expected to be best for solids close to a homogeneous gas and worst for very inhomogeneous cases like atoms where the density must go continuously to zero outside the atom. Nevertheless, even in very inhomogeneous cases, the LSDA works remarkably well. Generally, it over-binds molecules and solids but the chemical trends are usually correct.

The degree to which the LSDA is successful has made it useful in its own right and has stimulated ideas for constructing improved functionals.

2.4.2 Generalized Gradient Approximation (GGA)

The success of LSDA has led to the development of various generalized gradient approximations (GGA)[68] with marked improvement over LSDA over many cases. Widely used GGAs can now provide the accuracy required for density functional theory to be used in various type of analysis.

The first step beyond local approximation is a functional of the magnitude of the gradient of the density ($\nabla\rho$) as well as the value n at each point. The low-order expansion of the exchange and correlation energies does not lead to consistent improvement over LSDA. The basic problem is that gradients in real materials are so large that the expansion breaks down.

The term GGA denotes a variety of ways proposed for functions that modify the behavior at large gradients in such a way as to preserve desired properties. It is convenient to define the functional as a generalized form of Eq. 2. 18

$$E_{xc}^{GGA}[\rho^\uparrow, \rho^\downarrow] = \int d^3r \rho(\mathbf{r}) \epsilon_{xc}^{hom}(\rho) F_{xc}(\rho^\uparrow, \rho^\downarrow, \nabla\rho^\uparrow, \nabla\rho^\downarrow, \dots) \quad (2. 19)$$

where F_{xc} is dimensionless and ϵ_{xc}^{hom} is the exchange-correlation energy of the unpolarized gas. Numerous forms for F_{xc} have been proposed and they can be illustrated by three widely used forms of Becke(B88)[69], Perdew and Wang (PW91)[68], and Perdew, Burke, and Enzerhof (PBE)[70].

Typically, there are more rapidly varying density regions in atoms than in condensed matter, which leads to greater lowering of the exchange energy in atoms than in molecules and solids. This results in the reduction of binding energy, correcting the LDA over binding, and improving agreement with experiment, which is the most important characteristics of present GGAs. Generally, GGA approximation improves binding energies, atomic energies, bond lengths and bond angles when compared to those obtained by LDA.

2.4.3 LDA+U

The most enduring problem with Kohn-Sham approach is that no systematic way has been developed to improve functionals for exchange and correlation. The problems are most severe in materials in which the electrons tend to be localized and strongly interacting, such as transition metal oxides and rare earth elements. Various methods have been developed to extend the functional approach to incorporate effects that are expected to be important on physical grounds. One of

the suggested methods is the so called, LDA+U.

The term "LDA+U" stands for the methods that involve LDA- or GGA-type calculations coupled with an additional orbital-dependent interaction.[71] The additional interaction is usually considered only for highly localized atomic-like orbitals on the same site with the same form as the "U" interaction in Hubbard models.[72] The electrons are separated into two subsystems: localized d (or f) electrons for which Coulomb dd interaction should be taken into account by a term $1/2U\sum n_i n_j$ (n_i 's are d -orbital occupancies) as in a mean-field (Hartree-Fock) approximation, and delocalized s , p electrons which could be described by using an orbital independent one-electron potential. The effect of the added term is to shift the localized orbitals relative to the other orbitals, which attempts to correct errors known to be large in the usual LDA or GGA calculations. The "U" term should be varied or optimized in calculations in order to obtain reliable results.

2.5 Periodic Supercells

By using the above presented formalisms observables of many-body systems can be transformed into single particle equivalents. However, there still remains two difficulties: A wave function must be calculated for each of the electrons in the system and the basis set required to expand each wave function is infinite since they extend over the entire solid. For periodic systems both problems can be handled by Bloch's theorem.[73]

2.5.1 Bloch's Theorem

Bloch theorem states that in a periodic solid each electronic wave function can be written as:

$$\Psi_i(\mathbf{r}) = u_i(\mathbf{r})e^{i\mathbf{k}\mathbf{r}} \quad (2. 20)$$

where u_k has the period of crystal lattice with $u_k(\mathbf{r}) = u_k(\mathbf{r} + \mathbf{T})$. This part can be expanded using a basis set consisting of reciprocal lattice vectors of the crystal.

$$u_i(\mathbf{r}) = \sum_G a_{k,G} e^{i(\mathbf{G})\mathbf{r}} \quad (2. 21)$$

Therefore each electronic wave function can be written as a sum of plane waves

$$\Psi_i(\mathbf{r}) = \sum_G a_{i,k+G} e^{i(\mathbf{k}+\mathbf{G})\mathbf{r}} \quad (2. 22)$$

2.5.2 \mathbf{k} -point Sampling

Electronic states are only allowed at a set of \mathbf{k} -points determined by boundary conditions. The density of allowed \mathbf{k} -points are proportional to the volume of the cell. The occupied states at each \mathbf{k} -point contribute to the electronic potential in the bulk solid, so that in principle, an finite number of calculations are needed to compute this potential. However, the electronic wave functions at \mathbf{k} -points that are very close to each other, will be almost identical. Hence, a single \mathbf{k} -point will be sufficient to represent the wave functions over a particular region of \mathbf{k} -space. There are several methods which calculate the electronic states at special \mathbf{k} points in the Brillouin zone.[74] Using these methods one can obtain an accurate approximation for the electronic potential and total energy at a small number of \mathbf{k} -points. The magnitude of any error can be reduced by using a denser set \mathbf{k} -points.

2.5.3 Plane-wave Basis Sets

According to Bloch's theorem, the electronic wave functions at each \mathbf{k} -point can be extended in terms of a discrete plane-wave basis set. Infinite number of plane-waves are needed to perform such expansion. However, the coefficients for the plane waves with small kinetic energy $(\hbar^2/2m)|\mathbf{k} + \mathbf{G}|^2$ are more important than those with large kinetic energy. Thus some particular cutoff energy can be determined to include finite number of \mathbf{k} -points. The truncation of the plane-wave basis set at a finite cutoff energy will lead to an error in computed energy. However, by increasing the cutoff energy the magnitude of the error can be reduced.

2.5.4 Plane-wave Representation of Kohn-Sham Equations

When plane waves are used as a basis set, the Kohn-Sham(KS) [66] equations assume a particularly simple form. In this form, the kinetic energy is diagonal and potentials are described in terms of their Fourier transforms. Solution proceeds by diagonalization of the Hamiltonian matrix. The size of the matrix is determined by the choice of cutoff energy, and will be very large for systems that contain both valence and core electrons. This is a severe problem, but it can be overcome by considering pseudopotential approximation.

2.5.5 Local-Basis Sets

When finite size systems are considered or molecular calculations are performed, it is common to use a basis composed of a finite number of atomic orbitals, centered at each atomic nucleus within the molecule (linear combination of atomic orbitals ansatz). Initially, these atomic orbitals were typically Slater orbitals, which corresponded to a set of functions which decayed exponentially with distance from the nuclei. Later, it was realized that these Slater-type orbitals could in turn be approximated as linear combinations of Gaussian orbitals instead. Because it is easier to calculate overlap and other integrals with Gaussian basis functions, this led to huge computational savings.

Today, there are hundreds of basis sets composed of Gaussian-type orbitals. The smallest of these are called minimal basis sets, and they are typically composed of the minimum number of basis functions required to represent all of the electrons on each atom. The largest of these can contain literally dozens to hundreds of basis functions on each atom.

Basis sets in which there are multiple basis functions corresponding to each atomic orbital, including both valence orbitals and core orbitals are called single, double, or multiple-zeta basis sets.

Localized basis sets are especially useful, if it is desired to investigate onsite physical properties such as charge analysis on each atom or partial density of state calculations.

2.5.6 Non-periodic Systems

The Bloch Theorem cannot be applied to a non-periodic systems, such as a system with a single defect. A continuous plane-wave basis set would be required to solve such systems. Calculations using plane-wave basis sets can only be performed on these systems if a periodic supercell is used. Periodic boundary conditions are applied to supercell so that the supercell is reproduced through out the space. As seen schematically in Fig. 2. 1 even molecules can be studied by constructing a large enough supercell which prevents interactions between molecules.

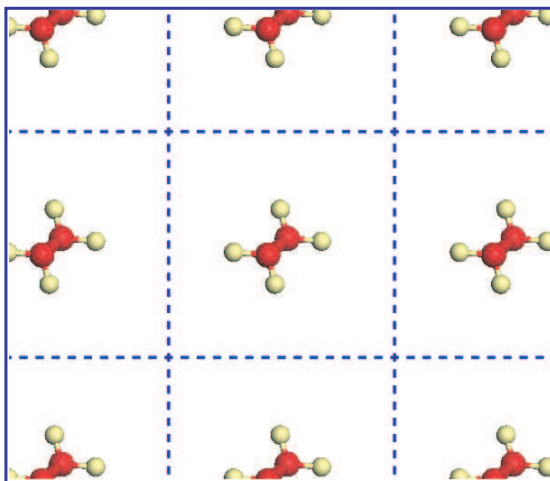


Figure 2. 1: A molecule in a supercell geometry.

2.6 Pseudopotential Approximation

It is well-known that most physical properties of solids are dependent on the valence electrons to a much greater extent than on the core electrons. The pseudopotential approximation utilizes this idea by replacing the core electrons and the

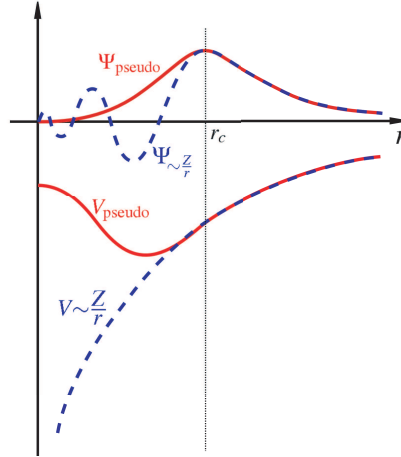


Figure 2. 2: Comparison of a wavefunction in the Coulomb potential of the nucleus (dashed) to the one in the pseudopotential (solid). The real (dashed) and the pseudo wavefunction and potentials (solid) match above a certain cutoff radius r_c .

strong ionic potential by a weaker pseudopotential that acts on a set of pseudo wave pseudo wave functions rather than the true valence wave functions. An ionic potential, valence wave function and corresponding pseudopotential and pseudo wave function are illustrated in Fig. 2. 2.

2.6.1 Ultrasoft Pseudopotential

One goal of pseudopotentials is to create pseudofunctions that are as smooth as possible and accurate. One approach known as "ultrasoft pseudopotentials" reaches the goal of accurate calculations by a transformation that re-expresses the problem in terms of a smooth function and an auxiliary function around each ion core that represents the rapidly varying part of the density. The transformation proposed by Vanderbilt[75] rewrites the non-local potential in a form involving a smooth function $\tilde{\phi} = r\tilde{\psi}$ that is not norm conserving. For each reference atomic states smooth functions $\tilde{\psi}$ are solutions of generalized eigenvalue problem.



Figure 2. 3: A conductor or device (C) which is connected to the leads L and R.

2.6.2 Projector Augmented Waves

The projector augmented wave (PAW) [76] method is a general approach to a solution of the electronic structure problem that reformulates the orthogonalized plane wave method (OPW), adapting it to modern techniques for calculation of total energy, forces, and stress. Like the ultrasoft pseudopotential method, it introduces projectors and auxiliary localized functions. The PAW approach also defines a functional for the total energy and it uses advances in algorithms for efficient solution of the generalized eigenvalue problem. However, the difference is that the PAW approach keeps the full all-electron wavefunction in a similar to the general OPW expression so it recovers the wavefunction within the core region of atoms. Since the full wavefunction varies rapidly near the nucleus, all integrals are evaluated as a combination of integrals of smooth functions extending throughout space plus localized contributions evaluated by radial integration.

2.7 Electronic Transport

The conductance through a region of interacting electrons (device) which is connected to leads (Fig 2. 3) is related to the scattering properties of the region itself and it is expressed by the Landauer formula [77]:

$$G = \frac{2e^2}{h} T \quad (2. 23)$$

where T is the transmission function and G is the conductance. The formula

represents the probability of an electron injected at one end of the conductor will transmit to the other end. The transmission function will be equal to one for a ballistic conductance. The transmission function can be expressed in terms of the Green's functions of the conductor and the leads [78]:

$$T = Tr(\Gamma_L \mathbf{G}_c^r \Gamma_R \mathbf{G}_c^a) \quad (2. 24)$$

where $\mathbf{G}_c^{r,a}$ are the retarded and advanced Green's functions of the conductor, and $\Gamma_{L,R}$ are functions that describe the coupling of the conductor to the leads. The Green's function of the conductor can be calculated from:

$$(\epsilon - H)\mathbf{G} = I \quad (2. 25)$$

where $\epsilon = E + i\eta$ with η arbitrarily small, I is the identity matrix, and H is the Hamiltonian of the whole system. If the Hamiltonian of the system expressed in a matrix representation, then Eq. 2. 25 corresponds to the inversion of an infinite matrix for the open system. This system consists of the conductor and the semi-infinite leads. The above Green's function can be partitioned into sub-matrices that correspond to the individual subsystems,

$$\begin{pmatrix} \mathbf{G}_L & \mathbf{G}_{LC} & \mathbf{G}_{LCR} \\ \mathbf{G}_{CL} & \mathbf{G}_C & \mathbf{G}_{CR} \\ \mathbf{G}_{LRC} & \mathbf{G}_{RC} & \mathbf{G}_R \end{pmatrix} = \begin{pmatrix} (\epsilon - H_L) & h_{LC} & 0 \\ h_{LC}^\dagger & (\epsilon - H_C) & h_{CR} \\ 0 & h_{CR}^\dagger & (\epsilon - H_R) \end{pmatrix}^{-1} \quad (2. 26)$$

where the matrix $(\epsilon - H_C)$ represents the finite isolated conductor, $(\epsilon - H_{R,L})$ represent the infinite leads, and h_{CR} and h_{LC} are the coupling matrices. From this equation explicit expression for \mathbf{G}_C can be obtained:[78]

$$\mathbf{G}_C = (\epsilon - H_C - \Sigma_L - \Sigma_R)^{-1} \quad (2. 27)$$

where we define $\Sigma_L = h_{LC}^\dagger g_L h_{LC}$ and $\Sigma_R = h_{RC} g_R h_{RC}^\dagger$ as the self-energy terms due to the semi-infinite leads and $g_{L,R} = (\epsilon - H_{L,R})^{-1}$ are the leads Green's functions. The self-energy terms can be viewed as effective Hamiltonians that arise

from the coupling of the conductor with the leads. Once the Green's functions are known, the coupling functions $\Gamma_{L,R}$ can be calculated as

$$\Gamma_{L,R} = i[\Sigma_{L,R}^r - \Sigma_{L,R}^a] \quad (2. 28)$$

where the advanced self-energy $\Sigma_{L,R}^r$ is the Hermitian conjugate of the retarded self-energy $\Sigma_{L,R}^a$. The core of the problem lies in the calculation of the Green's functions of the semi-infinite leads.

2.8 Methodology and Parameters Used in the Calculations

For all of the results presented, first-principles plane wave calculations [80, 81] within DFT [65, 66] using ultra-soft pseudopotentials [75] are performed. Some of the results are also confirmed by PAW potential [76]. The electronic configuration of the potential (valence and core electrons) is determined after verifying well-known experimental results (such as lattice parameters and cohesive energies of bulk crystal structures). The exchange-correlation potential has been approximated by generalized gradient approximation (GGA) using two different functionals, PW91[68] and PBE.[70] For partial occupancies, we have used the Methfessel-Paxton smearing method.[116] The width of smearing has been chosen as 0.1 eV for geometry relaxations and as 0.01 eV for accurate energy band and density of state (DOS) calculations. All structures have been treated by supercell geometry (with lattice parameters a_{sc} , b_{sc} , and c_{sc}) using the periodic boundary conditions. A large spacing ($\sim 10\text{\AA}$) between non-periodic directions has been assured to prevent interactions between them. Convergence with respect to the number of plane waves used in expanding Bloch functions and \mathbf{k} -points used in sampling the Brillouin zone (BZ) have been tested before analyzing the systems. The BZ of the systems has been sampled by necessary number of mesh points in \mathbf{k} -space within Monkhorst-Pack scheme.[74] A plane-wave basis set with kinetic energy cutoff $\hbar^2|\mathbf{k} + \mathbf{G}|^2/2m = 350\text{eV}$ has been used. All atomic positions and

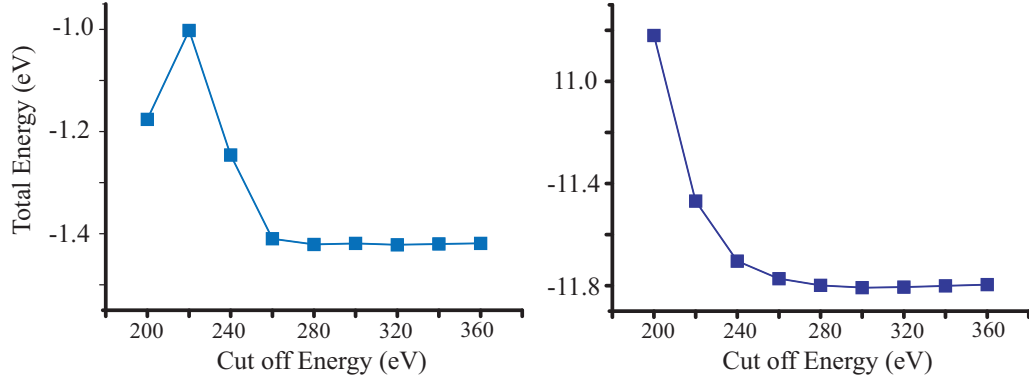


Figure 2. 4: The total energy (E_T) variation as a function of cutoff energy (E_{cut}) for single Co atom (left panel) and Co bulk crystal (right panel). The results are obtained by PAW potential.

lattice parameters have been optimized by using the conjugate gradient method where total energy and atomic forces are minimized. The convergence of calculation is achieved when the difference of the total energies of last two consecutive step is less than 10^{-5} eV and the maximum force allowed on each atom is less than 0.05 eV/Å. For finite structures, supercell has been constructed in order to yield ~ 10 Å vacuum space in each direction and BZ is sampled only at the Γ -point. The other parameters of the calculations are kept the same.

2.8.1 Convergence Tests

In order to obtain reliable results, especially the pseudopotential should be carefully chosen and the number of \mathbf{k} -points and kinetic energy cutoff (E_{cut}) should be carefully tested. E_{cut} depends on the atoms used in the calculations. If there are more than one atom in the system, than the atom with the highest E_{cut} will determine the limit. For the convergence test, the total energy(E_T) of a simpler system is calculated as a function of E_{cut} . In Fig. 2. 4 the convergence test for single Co atom and Co crystal is given as an example since it has one of the highest E_{cut} value. E_{cut} should be chosen in the region where E_T is not vary. For Co this value can should be greater than 300 eV and it is chosen as 350 eV in

our calculations. Similar analysis should be performed also for \mathbf{k} -point sampling. For this time not the simpler system but the E_T of original structure should be calculated as function of number of \mathbf{k} -point.

2.8.2 Stability: Molecular Dynamics and Transition State Analysis

Although it is possible to obtain reliable results first-principles results, further analysis are needed in order to clarify the stability of proposed structures. One of the ways to check the stability is to perform *ab initio* molecular dynamics calculations at high temperatures (at least higher than room temperature). If there is any instability, it should be observed at sufficiently long simulation time. Unfortunately, these kind of calculations are computationally very costly and a simulation time in the order of picosecond is quite a long time. In order to keep the temperature under control during simulation Langevin thermostat [82] is used. Langevin thermostat uses stochastic dynamics via Brownian motion model, implemented using the fluctuation-dissipation theorem. It is controlled by damping time parameter, which controls the rate of decay of fluctuations in the temperature. Otherwise the temperature of the system may increase to very high values while oscillating and the structure may be deformed or destroyed unrealistically.

A transition state analysis should also be performed in order to understand whether the obtained geometry is a global (or local) minimum or a metastable configuration. An element can be found in various forms in nature. As an example while the ground state of carbon is a diamond structure, C_{60} or nanotube configuration can also be synthesized. In other words, a configuration which is not a ground state can also be stable system if the states are separated by a sufficiently large energy barrier. In transition state analysis, we try different reaction paths to convert the obtained geometry from one configuration to other and calculate E_T at each step. In Fig. 2.5 two states of carbon linear chain and Cr atom is analyzed. As seen from the calculation while adsorption of Cr atom

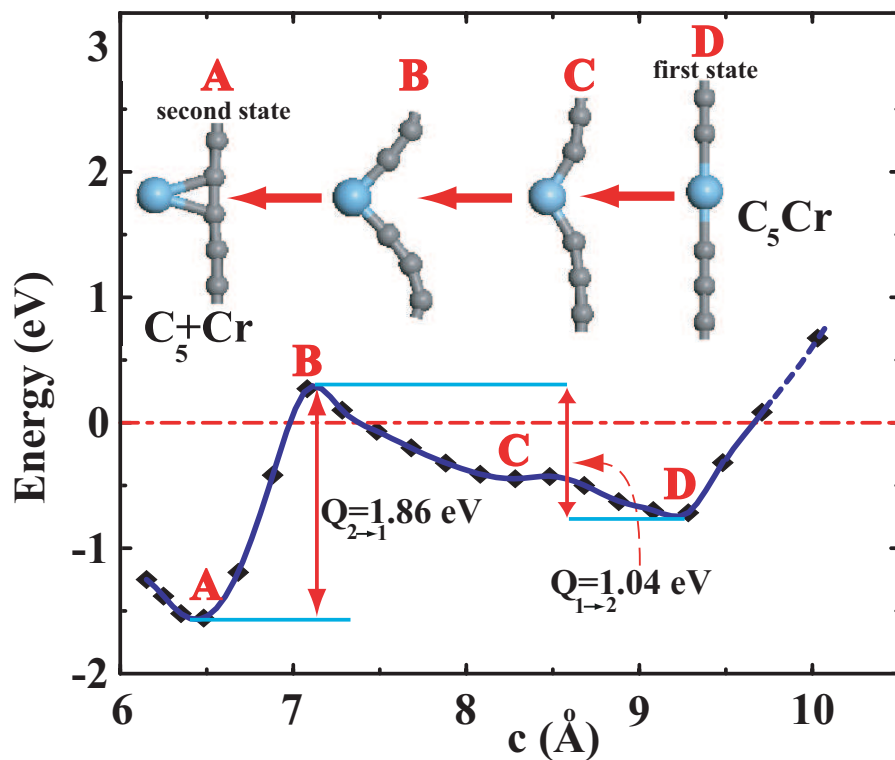


Figure 2. 5: Variation of energy, E_T , for the transition from the linear C_5Cr to the C_5+Cr state. $Q_{1\rightarrow 2}$ and $Q_{2\rightarrow 1}$ are energy barriers involved in the transitions. Zero of energy is taken relative to the free Cr atom and free periodic C-linear chain.

is more energetic, substitution of Cr atom is also an stable system since there is a very high energy barrier. This analysis is performed for all the systems under consideration.

The general parameters and potentials given in this section are tested and optimized for each type calculations. The calculation parameters and other details which are specific to that section will be briefly summarized for interested readers.

Chapter 3

Carbon Linear Chains

As it is discussed in Chapter 1 as an introduction, the fabrication of quantum structures with dimensions of the order of molecular sizes became possible. Even the ultimately thin wires made of single atomic chains are produced in experimental conditions and are actively studied. Linear carbon chain which is the main focus of this Chapter is also observed in a multiwalled carbon nanotube.[79] In this context, first principles studies of such molecular structures which may produce spin polarization effects are important. Motivated with these arguments, in this Chapter the spin-polarized structural, magnetic and electronic transport properties (GMR effect) of carbon atomic chains capped with 3d transition-metal atoms (TM- C_n -TM) and half-metallicity for periodic cases are studied. The magnetic ground state of the TM- C_n -TM molecular chains (para-, ferro- and antiferromagnetic) are analyzed. The size dependent (i.e., number of carbon atoms in the spacer) and TM dependent (i.e., type of TM atom) of physical properties are investigated. In order to understand the underlying super-exchange mechanism, a simple analytical Hückel-type model is presented. And, finally spin-dependent transport properties of these structures are examined.[83, 84, 85]

3.1 Methodology

For all the results obtained in this chapter, first-principles plane wave calculations[80, 81] are performed within Density Functional Theory (DFT)[65, 66] using the parameters which are discussed in Methodology Chapter.

Magnetic ground state is identified by calculating the energy difference $\Delta E_T = E^{su} - E_T^{sr}$ (the difference between spin-unpolarized (*su*) and spin-relaxed (*sr*) total energies). Chains with $\Delta E_T > 0$ and $\mu > 0$ have ferromagnetic ground state. For antiferromagnetic states, $\Delta E_T > 0$, $\mu = 0$, but the sum of the absolute value of spin states, $\sum_i [|S_i \uparrow| + |S_i \downarrow|] > 0$.

The stability of optimized structures at $T = 0$ K is tested first by applying deformations by displacing the atoms in random directions from their equilibrium positions and then by reoptimizing the deformed structures. Strongly deformed structures returning to their initial optimized configuration are taken stable. Furthermore, vibrational mode analysis is carried out to search for probable instabilities. In addition, we performed *ab initio* molecular dynamics calculations at high temperatures using Langevin thermostat.[82]

It should be noted that for comparison purposes the calculations have been repeated by using methods which utilize local basis sets, such as SIESTA [86] and GAUSSIAN03.[87] In the GAUSSIAN03 calculations the UBPW91 and UB3LYP functionals with 6-31G** basis set have been employed and results have been subjected to wave function stability analysis. All these calculations have led to consistent results.

The equilibrium conductance calculations of the structures when connected to metallic electrodes have been done using Landauer formalism.[78] The required Hamiltonian matrices of the device and electrode regions are obtained in a DZP basis (double-zeta basis plus polarization orbitals) using SIESTA,[86] and the surface Green function of the electrodes is calculated recursively.[88]

3.2 Atomic Structure

3.2.1 Binding energy and stability

Carbon atom-strings or -chains, C_n , which are the precursor to TM- C_n -TM molecular structures, have been investigated for decades.[89] Finite segments of C_n have already been synthesized.[90, 91] As an ultimate 1D structure having only one atom in the cross section, carbon strings can form only linear atomic chains and are stabilized by double bonds, which consist of a σ -bond of the carbon $2s+2p_z$ atomic orbitals along the chain axis, and π -bonds of $2p_x$ and $2p_y$ orbitals. Because of the cylindrical symmetry of the chain structure, the latter π -orbitals form a doubly degenerate but half-filled band, which cross the Fermi level. The double bond structure underlies the unusual properties of C_n , such as its high axial strength, transversal flexibility and strong cohesion. For example, the elastic stiffness of C_n , i.e. the second derivative of the strain energy per atom with respect to the axial strain, $d^2E/d\varepsilon^2$, was calculated to be 119 eV, which is twice the value calculated for the carbon nanotubes.[89] Despite its low coordination number of two as compared to four in diamond or three in graphite, the cohesion energy of C_n is as large as 90% of that of diamond crystal. Mechanical, electronic and magnetic properties of TM- C_n -TM are derived from those of carbon strings. First concern of this chapter is to demonstrate that TM- C_n -TM chains are stable and that their synthesis is energetically feasible.

Transition state analysis performed for different reaction paths provides us with the conclusive evidences showing that the linear TM- C_n -TM atomic chains are stable and can be synthesized. In Fig. 3. 1, the energetics related with the formation of CoC_7Co and CrC_7Cr atomic chains are presented. These chains can conveniently grow from a finite C_n chain by attaching TM atoms from both ends. No energy barrier is involved in the course of the binding. First, a single Cr atom is attached to the left end of the chain consisting of seven carbon atoms. Then, the second Cr atom is attached to the free right end. As expected, the variation of the binding energy, E_b , of the Cr atom with respect to its distance d from the end of the carbon chain is similar for both Cr atoms. The symmetry

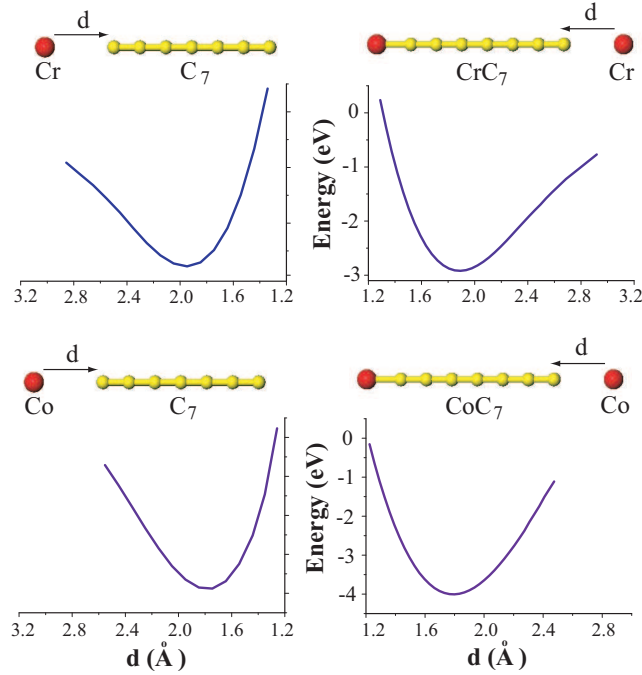


Figure 3. 1: Energetics of the formation of CoC_7Co and CrC_7Cr atomic chains. Left panels correspond to a TM atom attaching to the left free-end of the bare carbon chain; right panels are for the binding of a TM atom to the other end of the TM- C_n chain. The total energy of the system for $d \rightarrow \infty$ is set to zero in each panel.

of the $E_b(d)$ curves for the left and right panels in Fig. 3. 1 can be broken for small n , where significant direct coupling between two TM-atoms can be present. The binding energy of the Co atoms are found to be larger than that of Cr. The binding energies in the range of 2-4 eV/per TM-atom indicate an exothermic process. The energetics of growth clearly demonstrates that TM- C_n -TM chains are not simply a theoretical construct of fundamental interest, but they can also be realized experimentally. To this end, carbon monatomic chain produced at the center of a multi-wall carbon nanotube,[79] can be used as the initial stage of the fabrication. This way carbon nanotube itself encapsulates the compound and protects it from oxidation and chemisorption of foreign atoms. Experiments can be achieved by atomic manipulation using atomic force microscopy.

The optimized atomic structure of TM- C_n -TM atomic chains, in particular

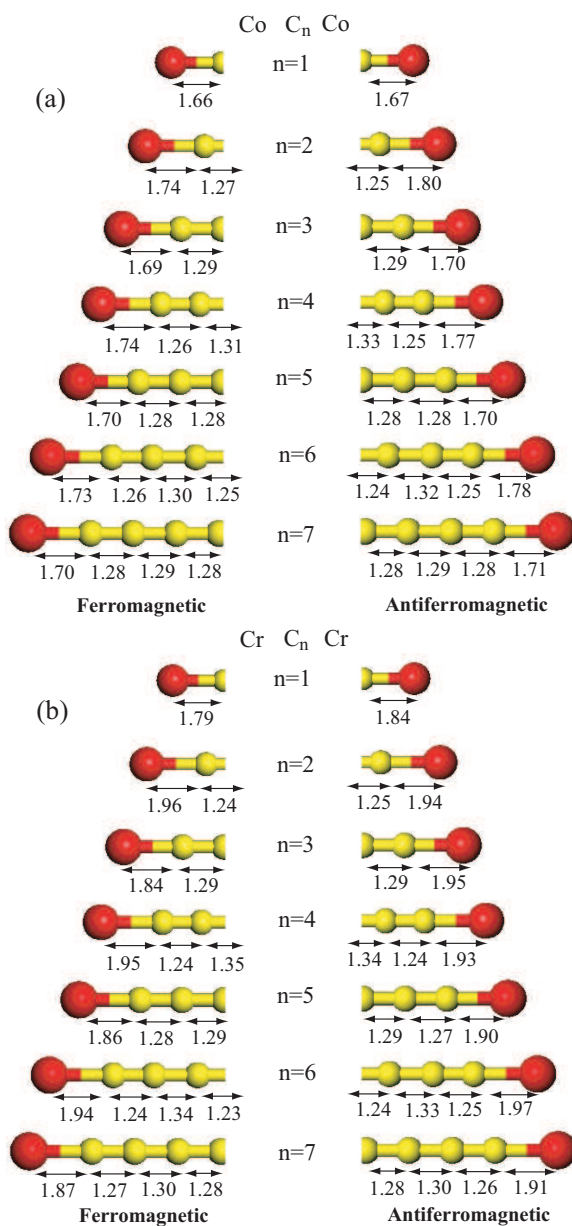


Figure 3. 2: Optimized interatomic distances (in Å) of TM-C_n-TM atomic chains in their ferromagnetic (left column) and antiferromagnetic (right column) states. (a) CoC_nCo; (b) CrC_nCr.

interatomic distances slightly vary depending on whether the chain is in ferromagnetic or antiferromagnetic state. However, a systematic variation based on the type of the magnetic state could not be deduced. On the other hand, in Fig. 3. 2 it is seen that C-C bond lengths of the chains exhibit a significant difference depending on n being odd or even. It is noted that C-C double bonds are rather uniform with $d \sim 1.28 \text{ \AA}$ when the number of carbon atoms n is odd for both the F and AF states. However, in the cases with even n there exists a bond-length alternation with two different types of C-C bonds. For the even n case, alternating single and triple C-C bonds with $d_{sin} \sim 1.33 \text{ \AA}$ and $d_{tri} \sim 1.25 \text{ \AA}$ are realized. When the carbon chain tends to dimerise the terminal Cr or Co atoms have longer bond lengths. The even-odd disparity displayed by the length and hence the types of bonds originate from the symmetry.

3.2.2 Ab-initio molecular dynamics calculations

It might be expected that the chain structures are vulnerable to clustering due to random motion of individual atoms at elevated temperatures, if the equilibrium structure has instabilities. To check this effect, the stability of the TM-C_{*n*}-TM linear chains are further tested by carrying out *ab-initio* molecular dynamics calculations at high temperatures using Langevin thermostat.[82] Calculations carried out for all structures at high temperatures ($800 \text{ K} < T < 1200 \text{ K}$), for 250 time steps (0.5 ps) confirmed the stability of linear chain geometry.

3.2.3 Breaking strength of the atomic chains

A crucial property of atomic chains is their stability against applied axial stress. The breaking strength is the maximum strain that a TM-C_{*n*}-TM atomic chain can sustain. Variations of total energy and the tensile force as a function of ε in CrC_{*n*}Cr for $n = 3$ and 4 are presented in Fig. 3. 3. Here the tensile strain is defined as the fractional elongation of the chain, namely $\varepsilon = (L - L_0)/L_0$, where L_0 is the equilibrium length of the chain, and L is the length of the structure under the applied tensile force F_t . It should be noted that $F_t = -L_0^{-1} \partial E_T / \partial \varepsilon$.

For small tensile strain ($\varepsilon > 0$) the variation of E_T is parabolic. Initially, the tensile force, F_t increases with increasing ε , passes through a maximum that corresponds to an inflection point of attractive E_T . Further increase of ε leads to decreasing of F_t . The maximum of F_t corresponds to the breaking point of the chain. Since the carbon-carbon bonds are much stronger, the chain breaks at one of the Cr contacts. In Fig. 3. 3 the breaking strain is estimated to be $\varepsilon_B \sim 13\%$.

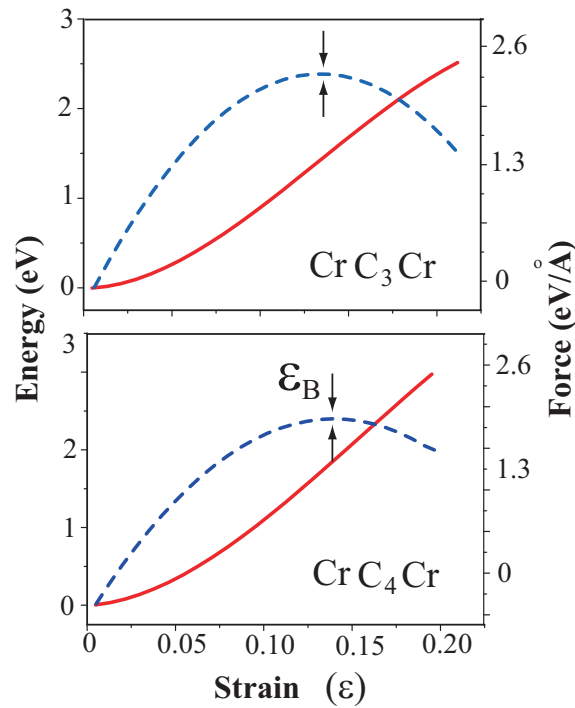


Figure 3. 3: Optimized total energy (continuous line) and tensile force (dashed line) versus strain of CrC_3Cr and CrC_4Cr atomic chains. The chain breaks for strain values exceeding the critical point corresponding to the maximum of the force curve indicated by arrows. The total energies in equilibrium are set to zero.

3.3 Magnetic Properties

The principle character of the TM- C_n -TM atomic chains is their magnetic ground state that varies with n . The exchange interaction of the magnetic TM atoms

through the nonmagnetic carbon chain determines the magnetic ordering in these molecular structures. In order to find the ground state magnetic moment, the total energy of the TM-C_n-TM structure is calculated for each possible value of its magnetic moment, since spin-relaxed calculations may sometimes fail to reach the lowest-energy magnetic state within the numerical algorithms available. If AF state is not the ground state, it is in general lowest-energy configuration of a F ground state in the TM-C_n-TM structures. The energy difference of the AF and the lowest-energy F states, $\Delta E_{F \rightarrow AF} = E_T(AF) - E_T(F)$, is a measure of the strength of the exchange interaction between the two TM atoms, and it is tabulated in Table 3.1 for all the elements of the 3d TM row of the periodic table, with $n = 1$ to 7. A negative value of $\Delta E_{F \rightarrow AF}$ corresponds to an AF ground state. It is the energy required to invert the local magnetic moment on one of the TM atoms to obtain an antiparallel alignment of the moments on the TM atoms starting from the parallel alignment (F state). The net molecular magnetic moments corresponding to the ground state are also tabulated in Table 3.1 (if the ground state is AF with $\mu = 0$, the moment of the higher energy F state is given in parenthesis). The total energy calculations performed using spin polarized LDA resulted in energies similar to those obtained by using spin-polarized GGA. For example, $\Delta E_{F \rightarrow AF}$ of CrC₃Cr is calculated to be 1.03 eV and 0.87 eV using LDA and GGA, respectively. Similarly CrC₄Cr has $\Delta E_{F \rightarrow AF} = -0.11$ and -0.08 eV by using LDA and GGA, respectively. In particular, the magnetic order in the ground states of chain structures are found to be robust and does not change when either one switches from GGA or LDA are employed.

An interesting feature revealed from the Table 3.1 is for a given TM atom the ground state of the TM-C_n-TM chain varies between F and AF configurations as a function of the number of carbon atoms. The variations are dominantly in the form of regular alternations with a period of two atoms, in particular for V, Cr, Fe, and Co. For the CrC_nCr molecules, the ground states are AF for even n , where the first excited state is F with a total magnetic moment $\mu = 10\mu_B$ (μ_B is the Bohr magneton). However for odd n the ground state is F with $\mu = 8\mu_B$. Calculations for CoC_nCo molecules show a similar but inverted behavior. The ground state is AF for odd n and the energy difference $\Delta E_{F \rightarrow AF}$ again oscillates in

Table 3.1: The energy difference of the AF and the lowest-energy F states, $\Delta E_{F \rightarrow AF} = E_T(AF) - E_T(F)$ in eV, and the magnetic moment μ of the ground state in units of Bohr magneton μ_B . For cases with AF ground states the moment corresponding to the lowest-energy F state is given in parenthesis.

TM- C_n -TM	Number of C atoms, n						
TM	1	2	3	4	5	6	7
Sc	-0.06 (2)	-0.11 (2)	-0.32 (2)	-0.10 (4)	-0.02 (2)	-0.06 (4)	-0.02 (2)
Ti	-0.28 (4)	0.41 6	0.36 4	0.40 6	-0.16 (4)	0.10 6	-0.16 (4)
V	-0.27 (6)	0.48 8	-0.34 (6)	0.37 8	-0.39 (6)	0.31 8	-0.27 (6)
Cr	1.12 8	-0.10 (10)	0.87 8	-0.08 (10)	0.70 8	-0.06 (10)	0.58 8
Mn	-0.09 (10)	-0.07 (12)	0.24 10	-0.04 (12)	0.29 10	-0.03 (12)	0.20 10
Fe	-0.34 (2)	0.34 6	-0.33 (4)	0.23 6	-0.32 (4)	0.19 6	-0.31 (4)
Co	-0.17 (2)	0.32 4	-0.12 (2)	0.28 4	-0.13 (2)	0.24 4	-0.13 (2)
Ni	0.00 0	1.18 2	0.00 0	0.18 2	0.00 0	0.07 2	0.00 0

sign with the variation of n but the signs are inverted. This even-odd n alternation is inherent to atomic chain structures, and manifests itself in the electronic and conductance properties of atomic chains.[92, 93, 89] The regular alternation of the magnetic ground state for longer CrC_nCr and CoC_nCo chains up to $n = 15$ have been found to persist.

The strength of the exchange interaction decays slowly with increasing n , as expected. In Fig. 3. 4, the case for CrC_nCr is considered as an example. The decay rate of the interaction as a function of the distance d between the Cr atoms is empirically deduced by fitting the $\Delta E_{F \rightarrow AF}$ values to a simple power dependence $\sim d^\alpha$. The value of α turns out to be -0.72 and -1.43 for the F and AF configurations, respectively. Models for extended systems (such as RKKY) that describe the exchange interaction of magnetic moments embedded in nonmagnetic media predict an asymptotic decay of the interaction in the form d^{-1} in one-dimensional systems. As will be discussed later in this section, this discrepancy exemplifies that conventional models are not readily applicable to the present molecular TM- C_n -TM structures.

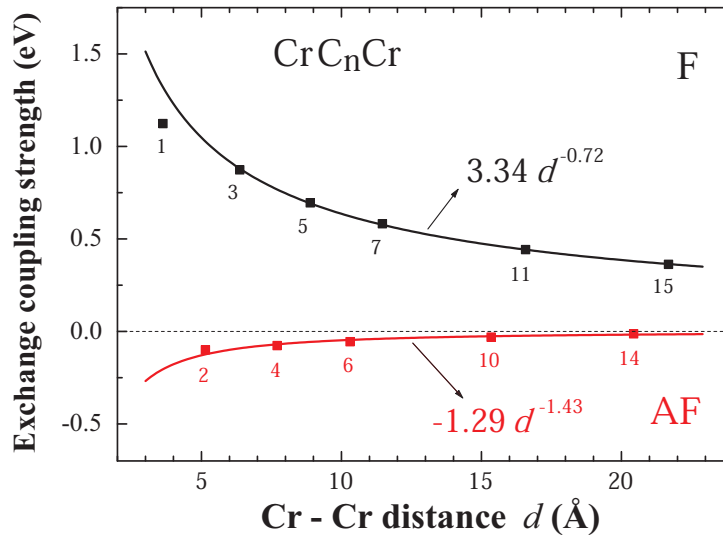


Figure 3. 4: The decay of the exchange interaction strength between the Cr atoms in CrC_nCr as a function of their separation d . The curves are the best fits to the $\Delta E_{F \rightarrow AF}$ values in the form $\sim d^\alpha$.

The $3d$ TM atoms can be grouped into sets according to the n -dependent ground state variations of the TM- C_n -TM chains. Namely, Ti, V and Fe display Co-like regular alternations, with the exception of TiC_3Ti , where the ground state is found to be F, although all other odd- n cases have AF states. Mn, Cr, and also Mo from the $4d$ row, on the other hand, display an inverted alternation where F and AF states are interchanged relative to the first set of elements. Again, MnC_1Mn is an exception. The latter set of TM atoms have the common property of half-filled d -shells, namely the electronic configurations of the neutral atoms having $3d^5$. The variations of the magnetic ground state with n of the chains made by Sc and Ni atoms, the far-end elements of the $3d$ row of periodic table, are different from the others. For Sc, all cases with $n = 1$ to 7 have AF ground states. Although the behavior of Ni resembles to that of the Co group in that the even- n cases have F ground states, the odd- n cases are *nonmagnetic* with $\mu = 0$. Fig. 3. 5 illustrates the variations of $\Delta E_{F \rightarrow AF}$ versus the number n of carbon atoms in the chain for the three different sets of TM atoms.

In the TM- C_n -TM molecules not only the magnetic ground state and the total molecular magnetic moment but also the distribution of the atomic magnetic moments display interesting variations. The spin dependent interactions within the molecule create distortions in the spin populations of the carbon atoms, leading to induced magnetic moments on the carbons too, which are nonmagnetic otherwise. The atomic magnetic moments are also calculated based on an orbital-resolved Mulliken analysis.[86] In Fig. 3. 6(a) CoC_4Co and CrC_4Cr are considered as sample cases in their ground and first excited magnetic states. Several distinct forms of atomic magnetic moment distribution on the carbon chain are obtained depending on the magnetic state of the molecule, type of the TM atom, and the length of the chain. The induced magnetic moments on the carbon atoms neighboring to the Cr atoms are as large as $|\mu| \sim 0.3\mu_B$ in CrC_4Cr . Owing to perfect linear geometry and quantum interference effects the induced magnetization of C atoms can be long-ranged. In Fig. 3. 6(b) we display their variation in the ground states of two longer molecules, CoC_{15}Co and CrC_{15}Cr , together with atomic spin populations and changes in total valance charges relative to isolated atoms. It is observed that in the F ground state of CrC_{15}Cr , even though the

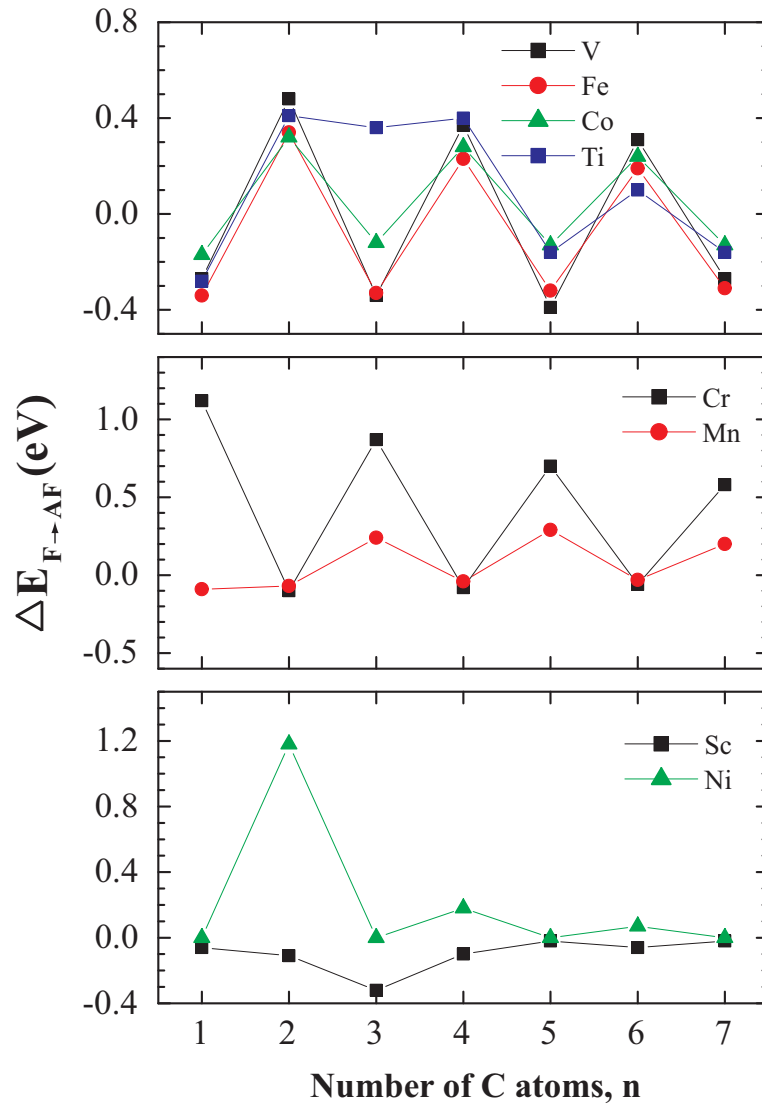


Figure 3. 5: The energy difference of the AF and the lowest-energy F states, $\Delta E_{F \rightarrow AF} = E_T(AF) - E_T(F)$ versus the number n of carbon atoms in the chain for different $3d$ transition metal elements.

total charge transfer of the carbon atoms are small except for the end atoms, there induces considerable spin imbalance on the carbon atoms leading to atomic magnetic moments alternating in sign.

The mechanism of the long-range exchange interaction between the TM atoms in the TM-C_n-TM structures can be inferred from the analysis of spin dependent interactions. It is in some respects reminiscent of Ruderman-Kittel-Kasuya-Yosida (RKKY) interaction[94] which deals with the coupling between magnetic impurities in a nonmagnetic host, and the interlayer exchange coupling of magnetic layers separated by nonmagnetic spacer layers.[95, 96, 97] RKKY interaction is a second order perturbative effect that plays a significant role in determining the coupling of localized *d*-shell electron spins in a metal by means of an interaction through the conduction electrons of the medium. The ferromagnetic/antiferromagnetic oscillations in the indirect exchange coupling of the magnetic impurities is a prediction of the RKKY theory. The interlayer exchange coupling theories explain the oscillatory variations in terms of the spin dependent change of the density of states due to quantum interferences generated by multiple reflections from the interfaces. In both formulations the oscillatory exchange coupling is related to the sharp cut-offs in momentum space due to the Fermi surfaces of the host or the spacer media.

Here, owing to the quasi-zero-dimensional nature and hence finite level spacing of the TM-C_n-TM structures, and non-perturbative character of the interaction of the TM atoms with the carbon chain a different treatment is required. One needs to employ self-consistent density functional methods or a direct diagonalization of the spin-dependent model Hamiltonian of the system. In the following, a simple model that can explain the qualitative features of the indirect exchange coupling in the TM-C_n-TM molecular structures is presented.

3.3.1 A tight-binding model

Variation of the exchange coupling between magnetic layers or atoms separated by non-magnetic spacers has been widely studied for extended bulk or layered

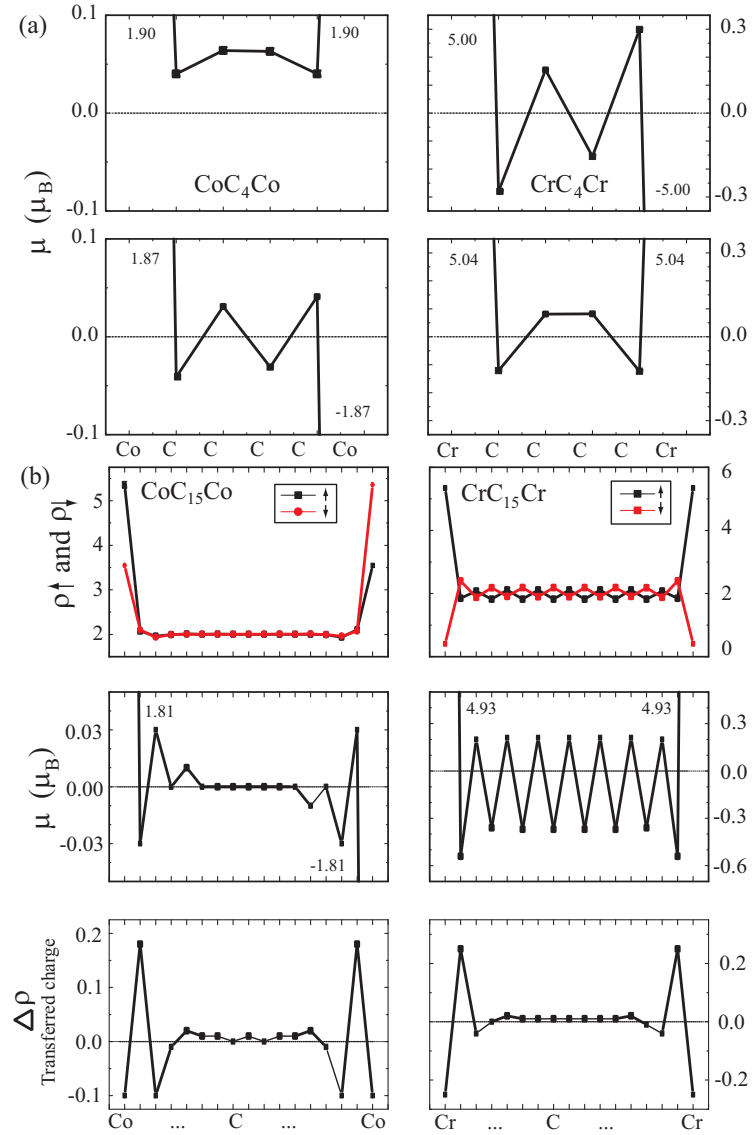


Figure 3. 6: (a) Variation of the atomic magnetic moments in the TM-C₄-TM atomic chains in their ground (top panels) and excited (down panels) states. Left (right) panels are for TM = Co (TM = Cr). (b) From top to bottom: Variation of spin-up $\rho \uparrow$ and spin-down charge $\rho \downarrow$ densities, atomic magnetic moments, and change in total valance charge $\Delta\rho$ in the TM-C₁₅-TM atomic chains. Again, left (right) panels are for TM = Co (TM = Cr).

systems both experimentally and theoretically. In our case of TM-atom capped carbon chains, the non-periodic nature of the system, and the strength of the spin-dependent interactions requires a model which can take into account the molecular character of the system. A simple model is proposed in order to explain the dominant mechanism of the exchange interaction between the TM atoms through a quasi-zero dimensional nonmagnetic spacer, i.e. the finite carbon chain. Two main features of the interaction to be simulated within our model are: (i) The variation of the energy difference between the F and AF states of the chain (namely $\Delta E_{F \rightarrow AF}$) with respect to the number of carbon atoms present, (ii) The dependence of atomic magnetic moments on the number of C atoms, and on the species of the TM atom. The model kept as simple as possible for the clarity of the basic mechanism.

Consider a tight-binding model Hamiltonian where each atom is represented by a site with a single level per spin type. Only the first nearest neighbor hopping is allowed.

$$H = \sum_{i=0;\sigma}^{n+1} \epsilon_{i,\sigma} c_{i,\sigma}^{\dagger} c_{i,\sigma} - \sum_{i=0;\sigma}^n t_{i,i+1;\sigma} c_{i,\sigma}^{\dagger} c_{i+1,\sigma} + h.c. \quad (3. 1)$$

where i is the site index. Zero and $(n + 1)$ sites are the TM-sites, in between are the carbon sites. $c_{i,\sigma}$ and $c_{i,\sigma}^{\dagger}$ are the annihilation and creation operators for an electron with spin σ ($\sigma = \uparrow, \downarrow$). The onsite energies $\epsilon_{i,\sigma}$ and the hopping terms $t_{i,i+1;\sigma}$ are both spin dependent. The non-magnetic carbon sites are represented by spin-degenerate parameters, and the effect of TM-capping is simulated by assigning spin dependent onsite and coupling parameters to the TM sites.

The relative strengths of the spin-dependent parameters of the TM sites can be inferred from the electronic structure of isolated TM atoms. The number of spin up and spin down electrons are different for a TM atom and the highest occupied (lowest unoccupied) spin up atomic level is different from that of the down spin. This enters to our model as different onsite parameters for each spin. The effective coupling parameters of the two spin states to the neighboring C sites will be different for the same reason. We choose the magnetic moment of the left TM site as positive and that of the right TM site is to be chosen with respect to the magnetic state of the molecule, that is positive for ferromagnetic

and negative for antiferromagnetic alignments. In Fig. 3. 7 a schematic plot of valence electron distributions that can be correlated to the relative strengths of the model Hamiltonian parameters is shown.

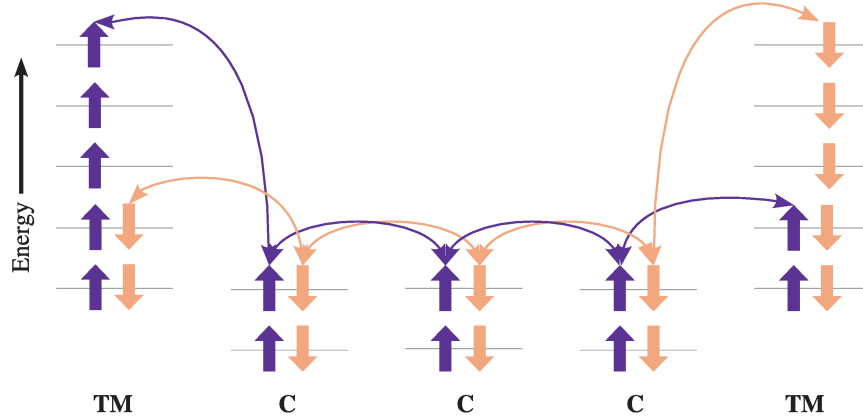


Figure 3. 7: Schematic electronic configuration of a TM-C_n-TM structure in an AF state. TM-sites have different onsite energies than the C-sites, and the hopping terms are dependent on the magnetic ordering. The energy cost for a spin-up electron of the first C-site to hop to the first TM-site is different from the energy cost for a spin-down electron to do the same hopping. The energy costs are reversed between the spins of the n^{th} C-site where they are identical for each spin for hopping between different C-sites.

An interpretation of this model is possible if one makes an analogy with a particle in a one dimensional potential well [97]. One needs to consider two different potential profiles for the electrons of each spin type. The potential for the majority spin electrons at the left TM-site is higher than the potential at the spacer, namely the well region. It leads to symmetric potential profiles for each spin type for the ferromagnetic configuration and antisymmetric ones for the anti-ferromagnetic case.

The Hamiltonian is then characterized in terms of parameters $\{E_1, E_2, t_1, t_2\}$ where $E_1 = \epsilon_{0,\uparrow}$, $E_2 = \epsilon_{0,\downarrow}$ are the onsite energies for the majority and minority spins of the left TM-site and $t_1 = t_{0,1,\uparrow}$, $t_2 = t_{0,1,\downarrow}$ are their coupling energies to the nearest carbon site. The onsite energy of the carbon sites are set to zero as reference and C-C hopping parameter to t for both spin types. As the same species

of TM atoms at both ends are considered, the onsite and hopping parameters of the right TM site are chosen in accordance with the particular magnetic order of the molecule (F or AF). Having written each parameter in units of t , spin-up and spin-down Hamiltonians of the system are diagonalized separately since we do not consider any spin-flip interactions. The energy spectrum for each spin type in both F and AF states of the molecule is calculated, and half filling is applied to the combined spectra to end up with the total energies of the F and AF configurations.

Co and Cr are kept as the cap TM atoms. Isolated Cr has 5 majority and zero minority spins in its d -shell, whereas isolated Co has 5 majority and 2 minority spins. When the TM atom is chemically bound to the C-chain from left, the electrons of the leftmost C-atom will experience different interaction potentials depending on their spins, and the coupling terms to the TM-site will also be spin dependent.

The energy cost for a majority spin electron to hop from the C-site to the TM-site is expected to be comparable for both Co and Cr atoms in view of their isolated electronic configuration. On the other hand, the energy required for a minority spin electron to hop from the C-site to the TM-site should be larger for Co atom than it is for Cr atom. Similarly, the hopping terms are different for minority spin electrons hopping to Co or Cr atoms. Along these arguments, we find that the parameter sets $\{1.0, 0.0, 1.5, 1.0\}$ and $\{1.0, 0.3, 1.5, 0.5\}$ for Cr and Co, respectively, lead to results in fairly good qualitative agreement with our first-principles DFT results. The difference in total energy of the molecule for varying number of C atoms is presented in Fig. 3. 8, as calculated using both the DFT methods and the simple tight-binding model. Although the model does not include any self-consistent calculations for the electronic configuration it is capable of representing the basic physical mechanism underlying the magnetic state dependence of the TM-capped C-chains on the number of atoms in the C-chain.

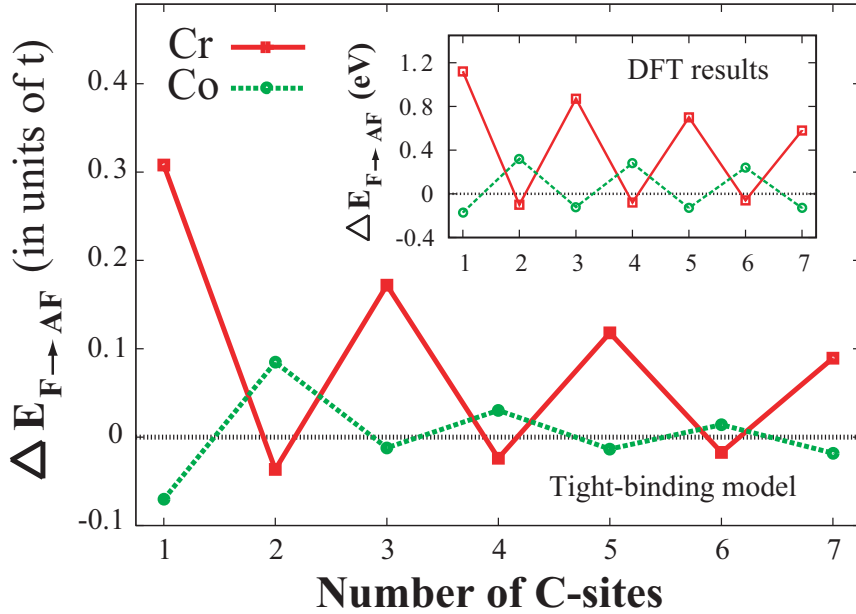


Figure 3. 8: Energy difference of the AF and the lowest FM states in the CoC_nCo and CrC_nCr atomic chains within the Hückel-type model.

3.3.2 Asymmetric atomic chains

The symmetric TM- C_n -TM finite chain structures have been discussed so far. How the above features change when the atomic symmetry of the chain is broken will be addressed next. First, we consider the TM- C_n -TM structure having asymmetry in the type of TM, like CoC_nCr chain with $n=1-4$. As expected, $\Delta E_{F \rightarrow AF} = E_{AF} - E_F$ is large and approximately equal to 1.6 eV for even n , but is relatively small and equal to 0.7 eV for odd n . Nevertheless, $\Delta E_{F \rightarrow AF} > 0$ indicating that the ground state of all these chains is ferromagnetic for all n ; $\mu = 7\mu_B$ for even n , and $\mu=5-6 \mu_B$ for odd n .

Another interesting situation combines two chains, CoC_nCo and CoC_mCo with $n = m - 1$ or $n = m$, into a chain $\text{CoC}_n\text{CoC}_m\text{Co}$. It is interesting to know the type of ground state of the chain, since CoC_nCo is ferromagnetic for even n , but antiferromagnetic for odd n . We found that the chain with $n = 3$ and $m = 2$ is F. It has $\Delta E_{F \rightarrow AF}=0.32$ eV and $\mu=5 \mu_B$. The case $n = m = 3$ has still

F ground state with $\Delta E_{F \rightarrow AF} = 0.23$ eV and $\mu = 10 \mu_B$ in spite of the fact that CoC_3Co has an AF ground state

3.4 Electronic properties

TM- C_n -TM chains have electronic energy structure with finite level spacing. Because of their magnetic ground state, energy gaps are separately defined for the minority and majority spin states. Namely, the gap for majority spin states is $E_g^\uparrow = E_{LUMO}^\uparrow - E_{HOMO}^\uparrow$. Similarly, for the minority spin states the energy gap is $E_g^\downarrow = E_{LUMO}^\downarrow - E_{HOMO}^\downarrow$.

3.4.1 Effect of strain

It is shown that the TM- C_n -TM structures can sustain strains of $\varepsilon \sim 13\%$ before they break. We consider how the electronic and magnetic properties of these chains change under the applied stress. We have calculated $\Delta E_{F \rightarrow AF}$, μ and E_g^\uparrow and E_g^\downarrow as a function of ε . Results are listed in Table 3.2 which show that the magnetic properties are robust. The AF or F ground state and the value of the magnetic moment μ remain unchanged. However, E_g^\uparrow and E_g^\downarrow display significant variation due to the relative shifts of LUMO and HOMO levels under tensile strain $0 \leq \varepsilon \leq 0.1$. In general due to the decreasing coupling between orbitals, E_g^\uparrow of TM- C_n -TM (with TM = Cr, Co and $n = 3$ and 4) decreases as ε increases. This trend is inverted only for CoC_4Co chain.

3.4.2 Half-metallic properties

Further to the interesting magnetic and electronic properties of TM- C_n -TM finite size atomic chains, the periodic $(\text{TM}-\text{C}_n)_\infty$ chains show half-metallic properties. In half metals (HM) [20, 21, 25], due to broken spin degeneracy, energy bands

Table 3.2: Variation of electronic and magnetic properties of TM-C_n-TM chains under axial strain ϵ . $\Delta E_{F \rightarrow AF}$ is the energy difference of the AF and the lowest energy F states given in eV. μ is the magnetic moment in units of μ_B . E_g^σ is the energy difference in eV between the lowest unoccupied and highest occupied molecular orbitals for spin type σ .

	$\epsilon = 0$	0.025	0.050	0.075	0.100
CrC₃Cr					
$\Delta E_{F \rightarrow AF}$	0.87	1.02	1.05	1.03	0.88
μ	8	8	8	8	8
E_g^\uparrow	1.33	1.23	1.13	1.06	0.98
E_g^\downarrow	1.83	1.73	1.60	1.47	1.33
CrC₄Cr					
$\Delta E_{F \rightarrow AF}$	-0.08	-0.07	-0.09	-0.10	-0.10
μ	0	0	0	0	0
E_g^\uparrow	1.27	1.13	0.99	0.85	0.69
E_g^\downarrow	1.27	1.13	0.99	0.85	0.69
CoC₃Co					
$\Delta E_{F \rightarrow AF}$	-0.12	-0.14	-0.14	-0.14	-0.14
μ	0	0	0	0	0
E_g^\uparrow	0.87	0.87	0.87	0.74	0.65
E_g^\downarrow	0.87	0.87	0.87	0.74	0.65
CoC₄Co					
$\Delta E_{F \rightarrow AF}$	0.28	0.15	0.07	0.04	0.01
μ	4	4	4	4	4
E_g^\uparrow	1.73	1.60	1.45	1.29	1.10
E_g^\downarrow	0.26	0.48	0.57	0.62	0.71

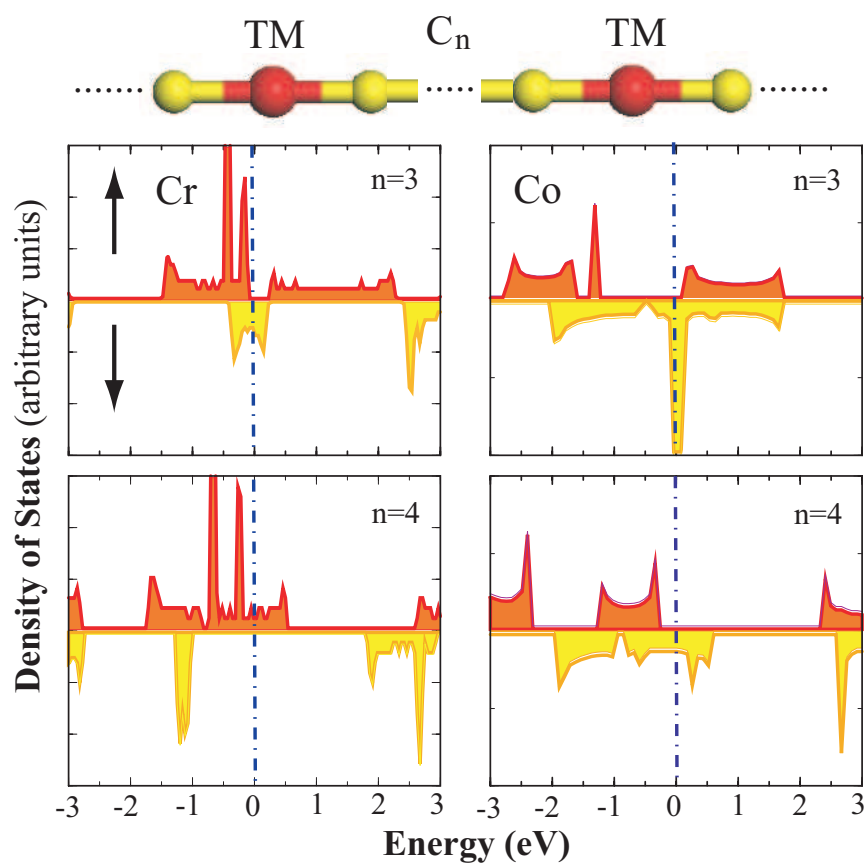


Figure 3. 9: Left panels: Spin-dependent total density of states of the periodic infinite $(\text{CrC}_3)_\infty$ and $(\text{CrC}_4)_\infty$ atomic chains. Right panels: Same for the $(\text{CoC}_3)_\infty$ and $(\text{CoC}_4)_\infty$. The Fermi energy is set to zero in all systems.

$E_n(\mathbf{k}, \uparrow)$ and $E_n(\mathbf{k}, \downarrow)$ split and each band accommodates one electron per \mathbf{k} -point. Furthermore, they are semiconductors for one spin direction, but show metallic properties for the opposite spin direction. As a result, the difference between the number of electrons of different spin orientations in the unit cell, $N = N_\uparrow - N_\downarrow$, must be an integer and hence the spin-polarization at the Fermi level $P = [D(E_F, \uparrow) - D(E_F, \downarrow)]/[D(E_F, \uparrow) + D(E_F, \downarrow)]$ is complete. Here $D(E_F, \uparrow)$ is the density of states of the majority spin states. This situation is in contrast with the ferromagnetic metals, where both spin-directions contribute to the density of states at E_F and P is less than 100%.

Our extensive analysis on these structures indicate that $(\text{CrC}_n)_\infty$ ($n = 2, \dots, 7$) and $(\text{CoC}_n)_\infty$ ($n = 1, \dots, 6$) are stable periodic structures and exhibit half-metallic properties with interesting even-odd disparities [101, 102]. Spin dependent total density of states of $(\text{CrC}_n)_\infty$ and $(\text{CoC}_n)_\infty$ are presented for $n = 3$ and 4 in Fig. 3. 9. For $(\text{CrC}_3)_\infty$, the majority spin bands are semi-conducting with $E_g^\uparrow = 0.4$ eV, but the minority spin bands cross the Fermi level showing a metallic behavior. However, in $(\text{CrC}_4)_\infty$ periodic chain the majority spin bands become metallic, while minority bands are semiconductor with a large gap, $E_g^\downarrow = 2.9$ eV as seen in Fig. 3. 10. Here we note also the even-odd n disparity in the spin types of metallic (semiconducting) bands. The number of carbon atoms determines whether the majority bands are an n-type or p-type semiconductor. For example, $(\text{CrC}_3)_\infty$ is a p-type semiconductor with direct band-gap. For $(\text{CoC}_3)_\infty$, E_g^\uparrow is direct and it exhibits an n-type character, but it is p-type when $n = 4$ as seen in Fig. 3. 11.

TM-3d orbitals play a dominant role in the electronic and magnetic properties of these periodic chains. The dispersive bands show significant TM-3d and C-2p hybridizations. Although small modifications to the band structure can be expected due to many body effects, the band structure leading to a metallic character is found to be robust and is not affected by the axial tensile stress of $\varepsilon < 0.05$. The spin-orbit coupling energy is also small and cannot influence the half-metallicity. Calculations performed in a double unit-cell demonstrated that the Peierls instability that could have caused the splitting of the metallic bands at the Fermi level does not occur in the present systems. For 1D structures atoms may dimerise and the energy of the system is lowered when compared

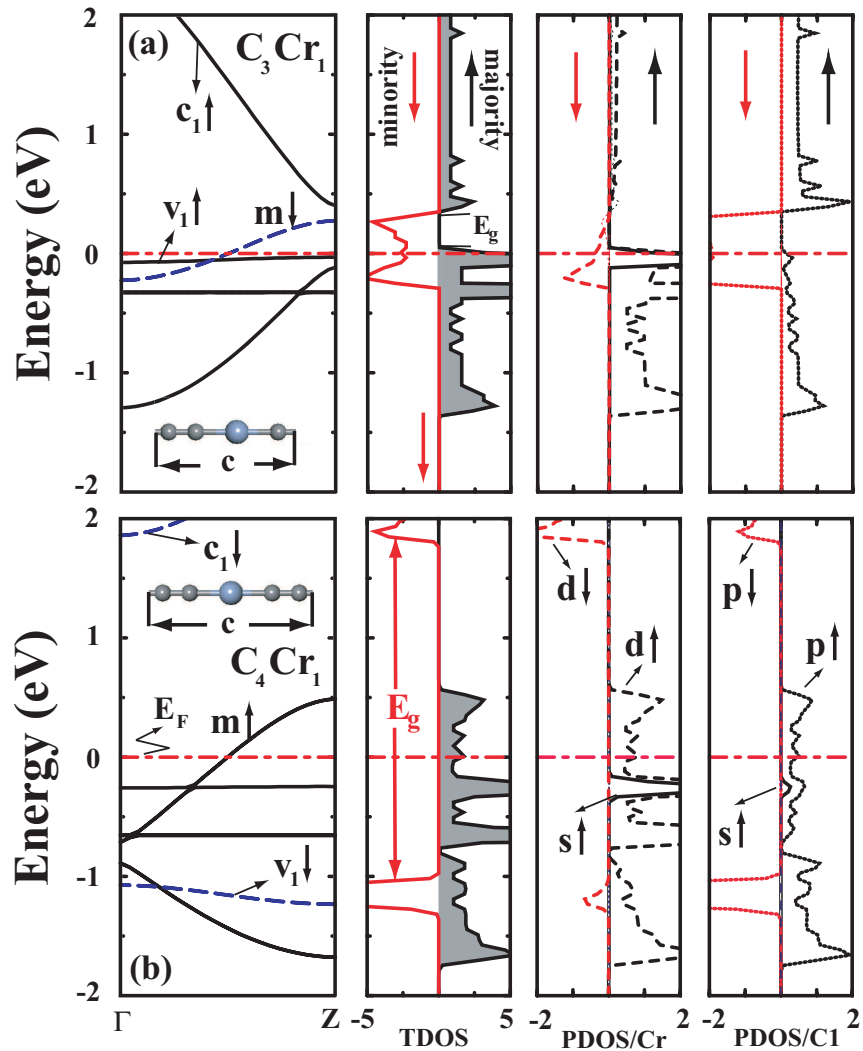


Figure 3. 10: (a) Energy band structure of C_3Cr ; corresponding total density of states (TDOS) for majority (\uparrow) and minority (\downarrow) spins; orbital projected local density of states at Cr atom (PDOS/Cr), at C atoms first nearest neighbor to Cr (PDOS/C1). (b) C_4Cr . State densities with s, p, d orbital symmetry in PDOSs are shown by thin continuous, dotted, broken lines, respectively. Zero of energy is set at E_F . Metallic band crossing the Fermi level, highest valence and lowest conduction bands are labelled by m, v_1 and c_1 , respectively.

to uniform structure. The energy lowering is due to splitting of folded metallic bands and this effect is known as Peierls instability or distortion. It should be noted that the band picture ceases in small segments of (TM-C_n) due to broken translational symmetry. Then, bands are replaced by the distribution of discrete states. However, as n increases the continuous state distribution of (CoC_n)_∞ is recovered as shown in Fig. 3. 12. In summary, the indirect exchange interaction of two Cr (or Co) atoms in the above structures underlies the half-metallic properties.

3.5 Transport properties

The spin-dependent properties of the isolated TM-C_n-TM chains are expected to lead magnetoresistive effects in their electronic transport properties similar to the GMR effect observed in magnetic multilayers. Only the two TM atoms play the role of the ferromagnetic layers, and the carbon chain is the spacer mediating the exchange interaction, leading to giant magnetoresistance ratios, and hence an analogous molecular scale GMR effect can be achieved.

Conductance properties of molecular devices, however, depend not only on their intrinsic structure but also on the electrodes. In particular if the coupling of the device to the electrodes is strong, the electronic structure and hence the transport properties of the device can be quite different, and cannot be inferred from the electronic structure of the isolated device. For the sake of simplicity, Au and Al atomic chains is considered to model the electrodes. The properly treated semi-infinite atomic chain electrodes still capture the essential features of the conductance properties of these molecular-size devices. In the case of Au electrodes, we find that the AF ground state of the TM-C_n-TM structures were maintained with smaller $|\Delta E_{F \rightarrow AF}|$ values than that of their isolated forms. However, the ground states were changed to F upon connecting to Al electrodes. In what follows the results obtained using Au-electrodes are presented.

We calculate the conductance of the device within Landauer formalism,

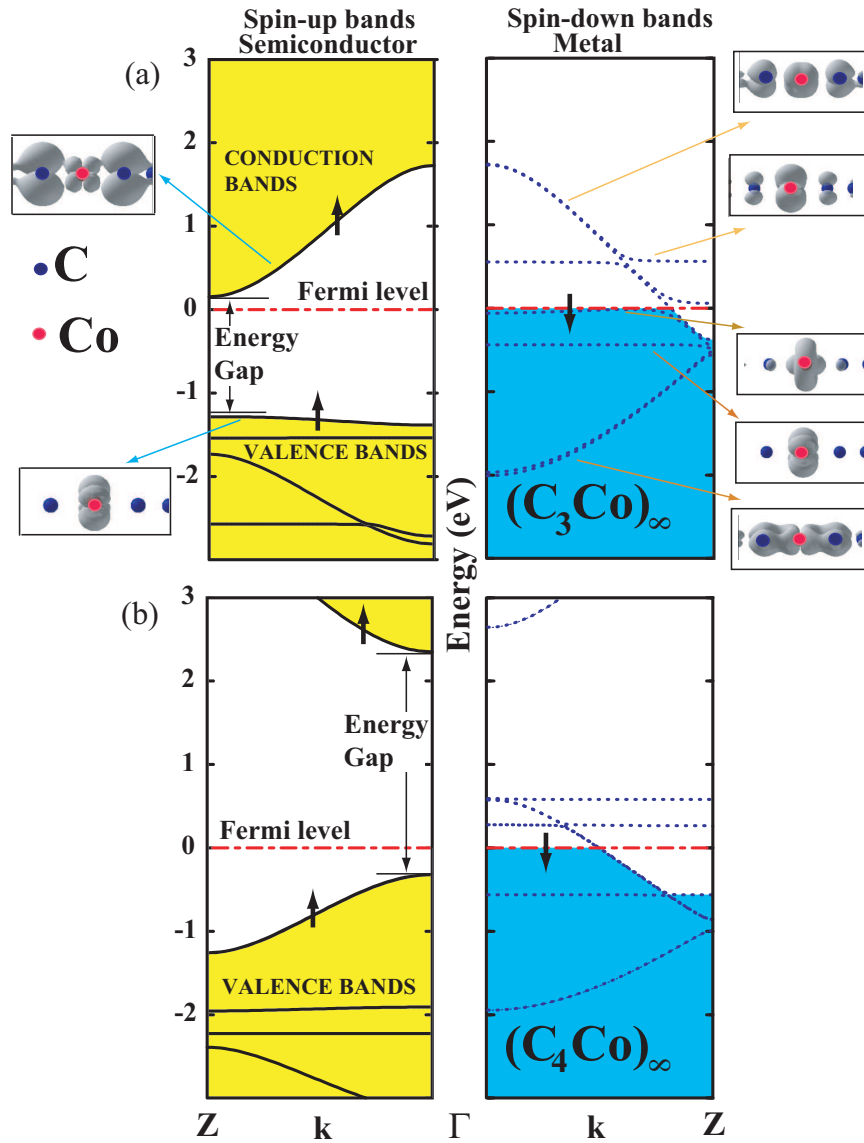


Figure 3. 11: Energy band structures and charge densities of selected states. (a) $(C_3Co)_\infty$ compound. Semiconducting majority spin (\uparrow) bands are shown in the left panel by continuous lines. The metallic minority spin (\downarrow) bands are presented in the right panel by dotted lines along the Γ -Z. Electron charge density plots of selected states are shown in small side-panels. The lobes of Co-3d and C-2p orbitals are clearly seen. (b) Same for the $(C_4Co)_\infty$ linear chain.

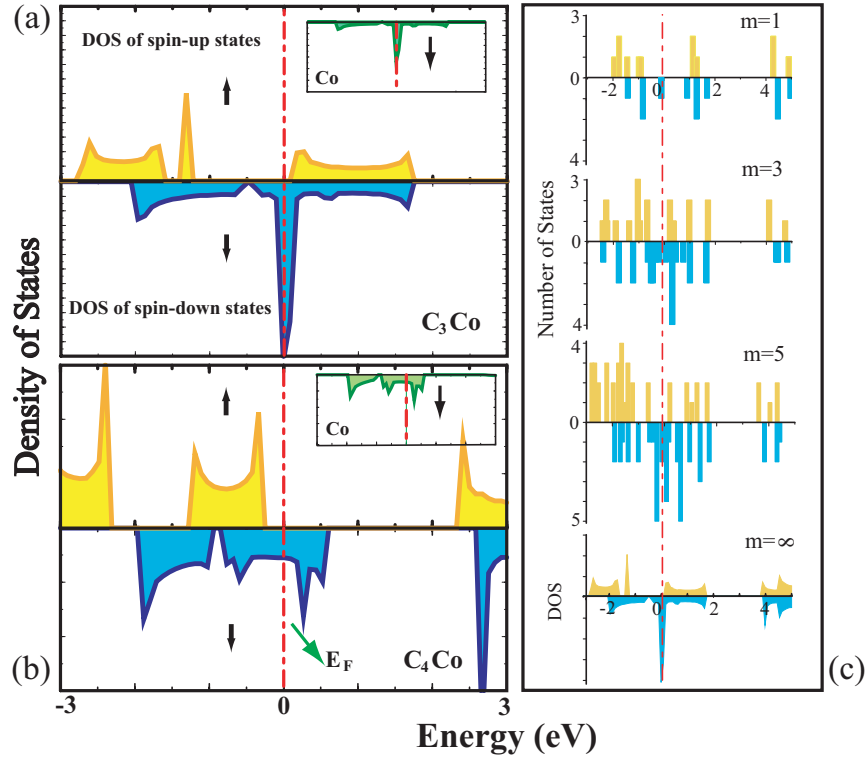


Figure 3. 12: Total density of majority (\uparrow) and minority (\downarrow) spin states in arbitrary units. (a) $(C_3Co)_\infty$ compound. The density (DOS) of the majority spin states has a band gap and the Fermi level is close to the conduction band edge. The density of minority spin states is high at the Fermi level. These states are derived from the Co- $3d$ and C- $2p$ orbitals. (b) Same for the $(C_4Co)_\infty$ compound. The insets show that the metallic states at E_F are derived from the $3d$ -states of Co atom. (c) DOSs calculated for $(C_3Co)_m$ chains show how the electronic structure of the infinite-periodic chain ($m = \infty$) develops from those of the finite-length chains (i.e. $m = 1, 3, 5$) as m increases.

$G(E) = (e^2/h)\text{Tr}(\mathbf{\Gamma}^L \mathbf{G}^r \mathbf{\Gamma}^R \mathbf{G}^a)$, for each spin configuration [78] as explained in Methodology chapter. In the above, \mathbf{G}^r and \mathbf{G}^a are retarded and advanced Green's functions, $\mathbf{\Gamma}^L$ and $\mathbf{\Gamma}^R$ are coupling functions to the left and right electrodes, respectively. In order to match the device potential and the surface potential of the semi-infinite electrodes, the device regions are defined to include some portions of the electrodes as buffer atoms. The self-consistent calculations lead to spin-up and spin-down Hamiltonians [86] of the device region, which are used to calculate the transmission coefficient for each spin state in the AF as well as in the excited F configuration. The surface Green's function of the contacts is calculated recursively.

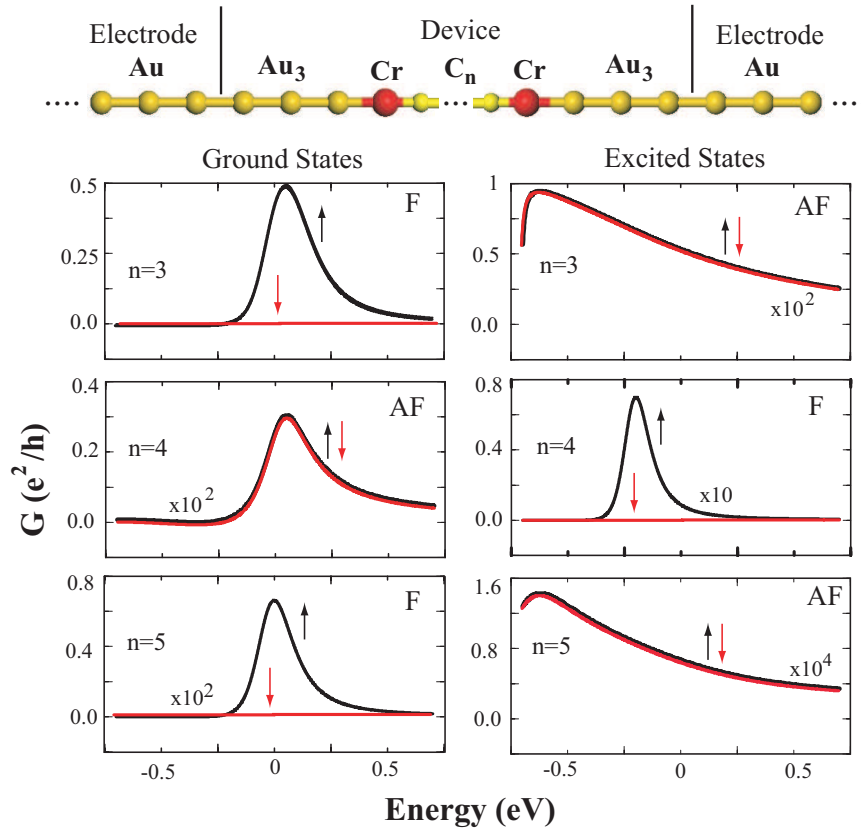


Figure 3. 13: Conductance versus energy for the CrC_nCr ($n = 3 - 5$) atomic chains between two infinite gold electrodes. The left (right) panels are for the ground (excited) magnetic states of the structures. The Fermi levels are set to zero.

Our results for the CrC_nCr ($n = 3 - 5$) atomic chains, which is connected

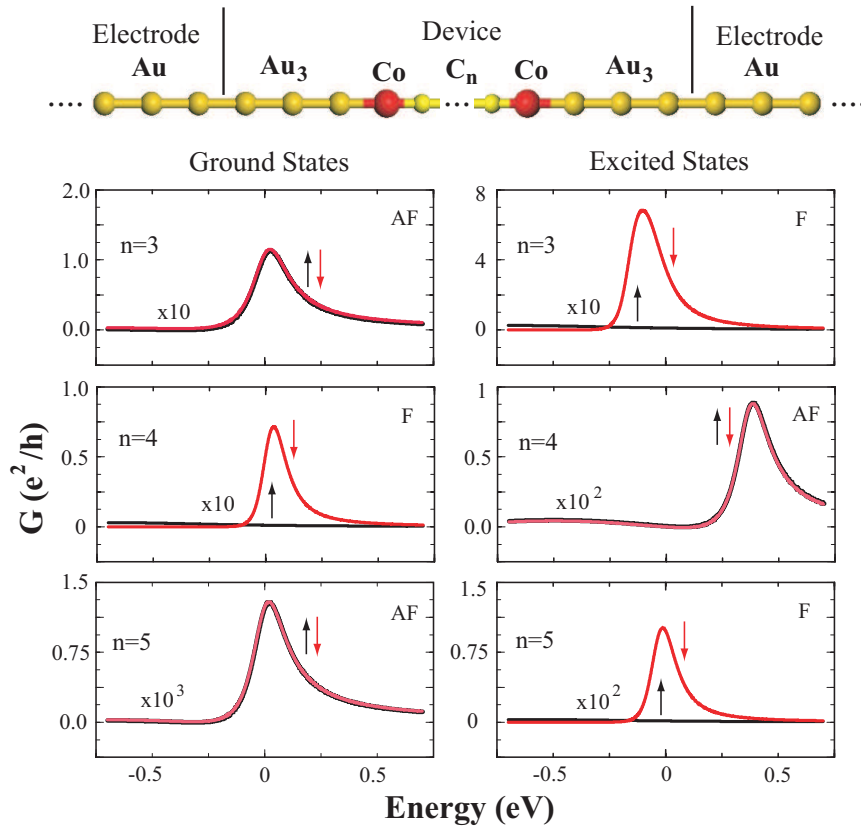


Figure 3. 14: Conductance versus energy for the CoC_nCo ($n = 3 - 5$) atomic chains between two infinite gold electrodes. The left (right) panels are for the ground (excited) magnetic states of the structures. The Fermi levels are set to zero.

to the Au-(chain) electrodes from both sides are presented in Fig. 3. 13. The calculated conductance G of these nanostructures in their ground state is given in the left panels. Since $n = 3$ structure is in F state, majority spin electrons have $G \sim 0.5 e^2/h$ while the minority spin electrons have negligible conductance. The situation is dramatically different for $n = 4$ which has AF ground state resulting in same but relatively smaller transmission for both spin orientations. CrC_5Cr has a F ground state as $n = 3$, but the conductance of majority spin electrons is relatively smaller due to the position of energy levels with respect to the Fermi level.

In the right panels, the transport characteristics of the excited states undergo dramatic changes. The conductance of spin-up electrons coincides with that of the spin-down electrons in the AF ground state of CrC_4Cr , namely spin-valve is off. In its F excited state while the transmission of spin-down electrons is substantially suppressed, the conductance of spin-up electrons is enhanced by one order of magnitude. In the latter situation, the spin valve is on. This is a clear indication of spin-valve effect through the linear CrC_4Cr molecule between two gold electrodes.

In Fig 3. 14, a behavior similar to CrC_nCr molecules is found for CoC_nCo molecules between two gold-electrodes. Here the spin valve effect occurs for $n = 3$ and $n = 5$. In the excited F state of CoC_3Co molecule the conductance of minority spin states is enhanced. We note that spin-valve effect in CrC_4Cr and CoC_3Co occurs effectively at $E < E_F$, and at $E = E_F$ for CoC_5Co . The shift of the maximum transmission from the Fermi level arises due to the shift of the energy levels of TM- C_n -TM molecule due to various reasons, such as number of C atoms and coupling to electrodes. We also note that the contribution of tunneling becomes significant for small n .

Conductance properties of molecular devices depend not only on their intrinsic structure but also on the electrodes. We have also examined Au leads with finite cross section to model more realistic electrodes. The TM- C_n -TM structures having an AF ground state remained AF with smaller $|\Delta E_{F \rightarrow AF}|$ values in cases of Au electrodes, whereas the ground states were changed to F upon connecting to Al

electrodes. Here, we choose to discuss the case of finite cross-section Au electrodes with single-atom sharp tips, which couples weakly to the device and preserves the generic electronic structure of the isolated TM-C_n-TM chains. Consequently, we obtain a prominent spin-valve effect that is compatible with the spin-relaxed energy configurations of the isolated molecules.

In Fig. 3. 15, we show our results for the CrC₄Cr molecule. In the AF state of the device, the conductance of majority-spin (spin-up) electrons coincides with that of minority-spin (spin-down). However, if the system is in the excited F state, the conductance through the spin-down levels is substantially reduced while it is enhanced through the spin-up levels. The equilibrium conductance value is enhanced by a factor of ~ 60 for the CrC₄Cr structure. This is a clear indication of a strong spin-valve effect through the TM-C_n-TM molecular structures. Consistent with the energy levels of the isolated chain given in the insets of Fig. 3. 15, it is the spin-up HOMO level in CrC₄Cr that dominantly contributes to the conduction.

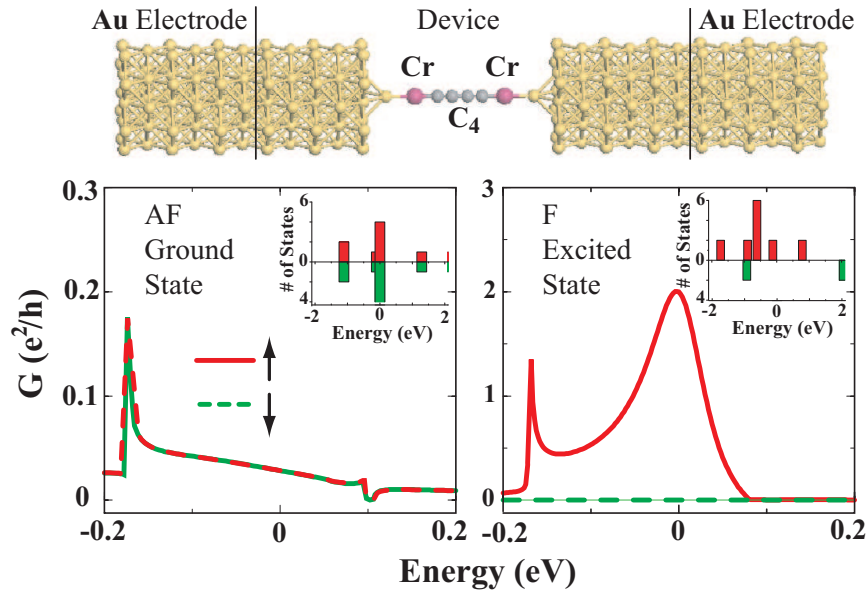


Figure 3. 15: Spin polarized conductance of CrC₄Cr molecular spin-valve device when connected to semi-infinite Au electrodes. The insets show the molecular energy levels of the isolated chains.

Chapter 4

Single-Wall Carbon Nanotubes

Nanotubes interacting with magnetic foreign objects are other possible candidates for spintronics structures. The ability to produce sizeable changes in the conductance of a nanotube due to an applied magnetic field has been one of the driving forces for active research on magnetic properties of carbon-based structures.[53, 103] Due to their inherent spin asymmetry, the interaction with magnetic foreign objects, such as adsorbed transition metal (TM) atoms,[104, 105, 106] nanoparticles [107], and substrates,[108] is likely to cause a spin-dependent response on the transport properties of the combined structure. [104, 107, 109, 110]

Costa *et al.*[50] investigated the indirect magnetic coupling between two distant magnetic adatoms attached to the wall of a carbon nanotube. They found that the coupling between TM atoms is mediated by the electronic carriers and is oscillatory for metallic armchair tubes, but monotonic for zigzag nanotubes. Spin-dependent transport through carbon nanotubes sandwiched between ferromagnetic electrodes has been studied recently. Experimental papers dealing with multi-wall carbon nanotubes (MWNT) have produced results which differ not only quantitatively, but also qualitatively from one another. For example, reported maximum GMR values using Co contacts have ranged from 9%[53] to 30%.[111]

The interaction of magnetic atoms with nanotubes may result in high spin-polarization and even a half-metallicity. Since carbon nanotubes are ballistic conductors,[112, 113] the spin polarization induced by magnetic electrodes (such as Fe, Co, or Ni) can be preserved as the electrons propagate through the nanotube. To this end, it has been necessary to know which elements can be best bonded to nanotubes and how they affect the magnetic properties. Based on the first-principles DFT calculation, Yang *et al.*[114] found that a Cr or V atomic chain adsorbed on a metallic armchair carbon nanotube opens up a band gap for the minority spin states, making the whole system a 100% spin-polarized conductor. The band gaps of minority spin bands were 0.49 and 0.44 eV for V and Cr, respectively. The adsorption of Mn, Fe, Co, or Ni chains led to large but not complete spin polarization.[114] Fagan *et al.* [105, 106] studied the structural, electronic and magnetic properties of Fe chains adsorbed on SWNT. They discussed several configurations including external and internal geometries by presenting calculated binding energies, band structures and magnetic moments. Similarly, Yagi *et al.*[115] investigated the interaction of $3d$ transition metal atoms and dimers with a single-walled armchair carbon nanotube by first-principles DFT. They found that Co atoms adsorbed at the hollow site of internal wall of armchair nanotubes can show half-metallic behavior.

In this chapter, the spin-dependent properties of TM (Co, Cr, Fe, Mn, and V) atomic chains adsorbed on the external and internal walls of zigzag SWNTs are presented. Variation of the spin polarization with radius of SWNT as well as with the type of TM atoms, which are adsorbed according to well-defined patterns (decorations) are examined. Moreover the strain analysis in radial and axial directions are performed in order to reveal how robust the magnetic properties are. It should be noted that while the half-metallicity requiring an integer number of spin per unit cell can exist only for infinite and ideal systems, realistic devices can be produced only on finite-size SWNTs, which are either connected to the metal leads or lie on a substrate. In this respect, the main issue is to achieve a high spin-polarization on a finite size SWNT. In order to clarify the effect of nanotube-size on the spin-dependent electronic structure, finite systems are also investigated.

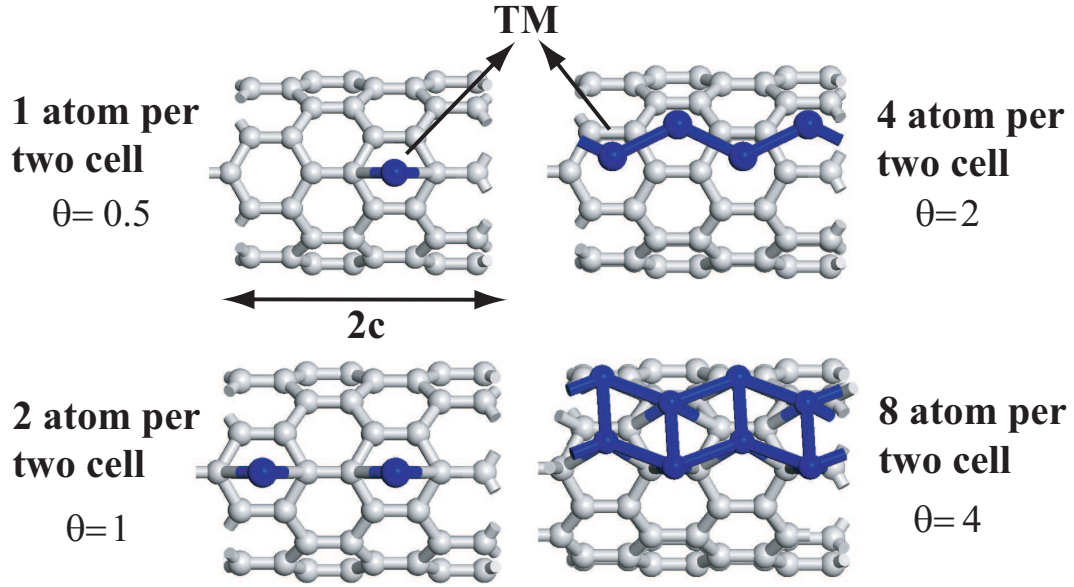


Figure 4. 1: The configuration of adsorbed transition metal (TM) atoms (Co, Cr, Fe, Mn, and V) forming chain structures on the (8,0) SWNT are illustrated for various coverage geometries, such as $\theta=1/2, 1, 2$ and 4 .

4.1 Methodology

For all the results obtained in this chapter, first-principles plane wave calculations [80, 81] is performed within Density Functional Theory (DFT) [65, 66] using the parameters which are discussed in Methodology chapter.

The binding energy (per atom) of the adsorbed TM atomic-chain has been calculated for each configuration by using the expression,

$$E_b = \{E_T[SWNT] + E_T[TM - chain] - E_T[SWNT + TM - chain]\}/N \quad (4. 1)$$

where N is the number of adsorbed TM atoms per cell. In this equation, three terms respectively stand for the optimized total energy of the bare SWNT, TM-chain, and SWNT with adsorbed TM-chain. All the optimized total energies are calculated in the same supercell. The spin-polarization at the Fermi level, E_F

	$\theta = 1/2$				$\theta = 1$				$\theta = 2$			
	$d_{C-TM}(\text{\AA})$	$E_b(\text{eV})$	$\mu(\mu_B)$	$P(E_F)$	d_{C-TM}	$E_b(\text{eV})$	$\mu(\mu_B)$	$P(E_F)$	d_{C-TM}	$E_b(\text{eV})$	$\mu(\mu_B)$	$P(E_F)$
Co	2.0	1.7	1.1	-	2.0	1.4	1.1	-	2.0	0.6	1.7	-0.65
Cr	2.2	0.6	4.2	-0.21	2.2	0.4	5.2	0.38	2.3	0.5	4.4	0.53
Fe	2.1	0.8	2.2	-0.91	2.1	0.9	4.0	-	2.2	0.5	3.1	-0.65
Mn	2.2	0.4	5.5	-	2.2	0.7	5.0	-	2.5	0.6	4.6	-0.19
V	2.2	1.4	3.8	0.68	2.2	1.5	4.1	0.90	2.3	1.0	2.9	0.73

Table 4.1: The distance between TM and nearest C atom d_{C-TM} ; average binding energy E_b ; average magnetic moments per atom μ ; spin-polarization at the Fermi level $P(E_F)$ for chain structures of Co, Cr, Fe, Mn, and V transition metal atoms adsorbed on the (8,0) SWNT for $\theta = 1/2, 1$, and 2 . $P(E_F) < 0$ corresponds to $D(E_F, \downarrow) > D(E_F, \uparrow)$.

is defined as

$$P(E_F) = [D(E_{F,\uparrow}) - D(E_{F,\downarrow})]/[D(E_{F,\uparrow}) + D(E_{F,\downarrow})] \quad (4. 2)$$

in terms of the density of states of majority and minority spin states, $D(E_{F,\uparrow})$ and $D(E_{F,\downarrow})$, respectively. The average binding energy E_b , the average magnetic moment per adsorbed TM atom μ , and $P(E_F)$ have been calculated for different level of coverage of $\theta = 1/2, 1$ and 2 . Here, θ indicates the number of adsorbed TM atoms per unit cell. In order to remove the constraints of supercell geometry and to test the stability further, the TM atomic chain-SWNT systems have been relaxed after their supercell sizes are doubled (namely $c_{sc} = 2c$). Moreover, in order to test the effects of deformation on the physical properties, we have also studied the cases where the underlying (8,0) tubes are kept under -25% radial strain.[117]

4.2 TM-wires adsorbed on SWNT

In this section, firstly the results for TM atoms adsorbed on the external and internal walls of the (8,0) SWNT to form an atomic chain are summarized.

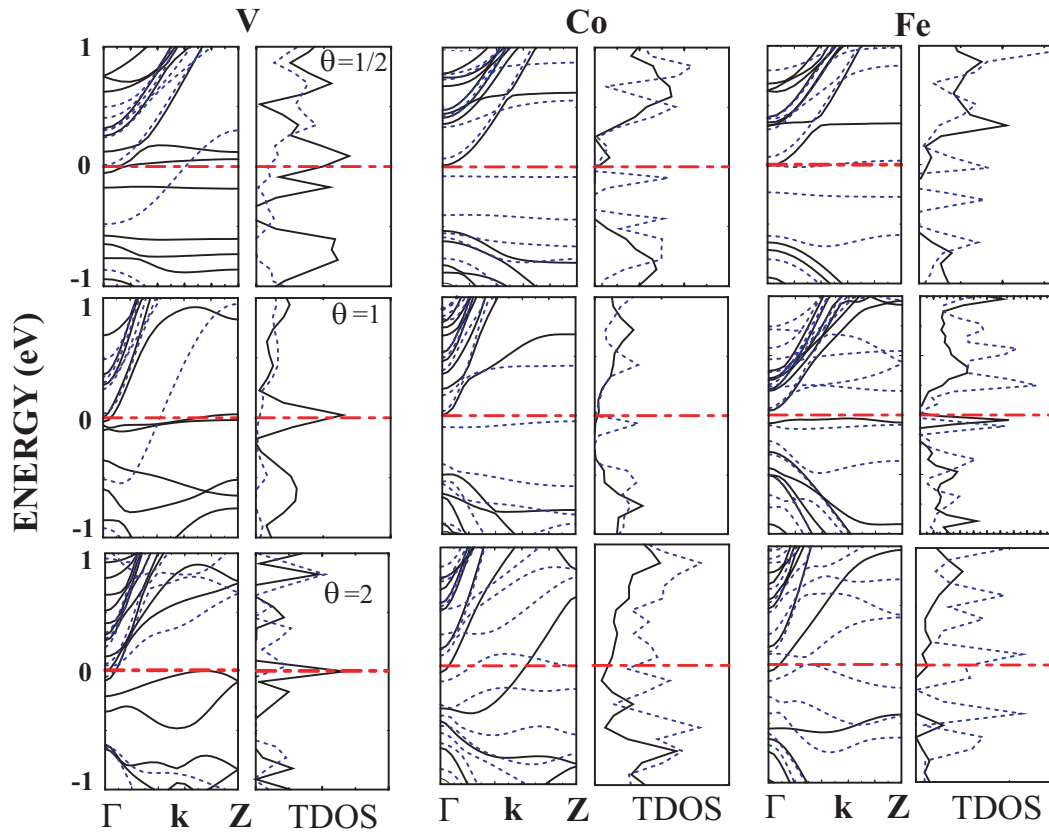


Figure 4. 2: The spin-dependent band structure and total density of states (TDOS) of V, Co and Fe-chains adsorbed on the zigzag (8,0) SWNT for $\theta=1/2$, 1 and 2 geometries. Solid and dotted lines are for majority and minority spin states, respectively. The zero of energy is set to the Fermi level E_F .

4.2.1 External adsorption

Bond distances d , E_b , μ , and $P(E_F)$ calculated for the Co, Cr, Fe, Mn, and V atomic chains adsorbed on the (8,0) zigzag SWNT are listed in Table 4.1 for $\theta = 1/2, 1$, and 2. The atomistic model corresponding to various coverages is illustrated in Fig.4. 1. The spin-polarized band structures and the total density of states (TDOS) near E_F are presented in Fig. 4. 2 for adsorbed V, Co, and Fe chains and in Fig. 4. 3 for Mn and Cr chains.

4.2.1.1 Vanadium

The ground state of the V-chain adsorbed on SWNT is found to be ferromagnetic for all geometries described in Fig. 4. 1. The value of the average magnetic moment (All magnetic moments are given per TM atom unless otherwise mentioned), μ is calculated as 3.8, 4.1, and 2.9 μ_B for $\theta=1/2$, 1, and 2, respectively. The calculations are also performed for the bare V-chains by removing the (8,0) SWNT, but keeping the same chain geometry when they were adsorbed on the tube. For example, for $\theta=1/2$, where the distance between nearest V atoms (d_{V-V}) is 8.52 Å, μ is calculated as 5.0 μ_B , that is equal to the magnetic moment of the free V atom in s^1d^4 configuration. This indicates that for $\theta=1/2$ V-V coupling is negligible. V-C interaction or charge transfer between V and C atoms is responsible for the reduction of μ from 5.0 μ_B to 3.8 μ_B upon adsorption on SWNT. As for $\theta=1$, d_{V-V} of the bare V atomic chain becomes 4.26 Å and $\mu=4.8 \mu_B$; for $\theta=2$, $d_{V-V}=2.4$ Å and resulting μ is 4.1 μ_B . These interactions are also crucial for the stability of decorated structures on SWNT which were discussed previously both experimentally [118] and theoretically.[109, 110] The coupling between V atoms gets stronger as θ increases. This causes a slight increase in the distance between V-C atoms from 2.2 to 2.3 Å.

The adsorption of the V-chain makes the semiconducting (8,0) SWNT metallic for both spin directions. Complete polarization at E_F , in other words half-metallicity (having an integer number of net spin in a cell) did not occur. However, for $\theta=1/2$ and 1 the density of states for majority spin carrier at E_F , $D(E_F, \uparrow)$ is

much larger than minority spin carrier as illustrated in Fig. 4. 2. Since, $P(E_F)$ as large as 90% can be achieved, these structures may be suitable for spintronic device applications.

For nanotubes, namely (10,0) and (14,0) with a larger radius, Yang *et al.*[114] found d_{C-V} as 2.2 Å and $\mu = 2.2\mu_B$ with $P(E_F) = 45\%$ for $\theta = 2$ geometry. They also showed that V-chain adsorbed on armchair SWNTs exhibit HM properties.[114] Andriotis *et al.*[119] found that the hollow site of graphene is energetically favorable with $d_{C-V} \sim 1.9$ Å and $\mu = 1.02\mu_B$. It is very well known that SWNT with small radius, that can be viewed as the graphene sheet rolled over a cylinder of radius R , behaves differently from the planar graphene. On the other hand, adsorption properties of a SWNT with very large radius can be taken as those of planar graphene corresponding to $R \rightarrow \infty$.

4.2.1.2 Iron

For $\theta=1/2$, the SWNT+TM atomic chain system has a ferromagnetic ground state with $\mu = 2.2\mu_B$. Here μ is reduced from the magnetic moment of free atom due to Fe-C interaction which, in turn, results in transfer of 4s electrons to 3d as confirmed by our Mulliken analysis. The energy band calculation shows that system is metallic for both types of spin carriers, but $P(E_F)$ is very high for minority spin carriers. Analysis of partial density of states (PDOS) suggests that the hybridized 3d states of Fe contributes to $P(E_F)$. For $\theta = 1$, the ground state of the system is still ferromagnetic, but the increased Fe-Fe interaction and reduction in unit cell size make the system semiconducting with negligible $P(E_F)$. For $\theta = 2$, the ferromagnetic system is metallic for both spin carriers. While Fe-C distances have changed slightly under radial strain $\epsilon_r = -0.25$, the metallicity for both spin carriers and high $P(E_F)$ is maintained. For the same structure on the (8,0) SWNT Fagan *et al.*[105] obtained similar results for ground state properties. They calculated d_{C-Fe} between 2.1-2.4 Å and μ as $3.0 \mu_B$ which are consistent with present results. However, they obtained E_b as 0.9 eV which is larger than ours. Our results indicate that the system is metallic with high $P(E_F)$, whereas they predicted a semiconducting structure with a small gap. Moreover,

the optimized geometry of the present study is also different. Those differences between the present study and that of Fagan *et al.*[105] perhaps originate from different method of calculations (plane wave versus local basis set). Yang *et al.* [114] predicting metallic character with $P(E_F)=86\%$ and $\mu = 2.6\mu_B$ for (14,0), confirms our results. For the graphene structure Yagi *et al.*[114] and Duffy *et al.*[121] also found hollow site as the most stable adsorption site for a single Fe with $\mu \sim 2\mu_B$.

Finally, the properties of two parallel Fe-chains adsorbed on the (8,0) SWNT which is specified as $\theta = 4$ have been studied. The ground state of the system is ferromagnetic with $\mu = 3.0\mu_B$ per Fe atom and shows metallic behavior for both spin carriers with negligible $P(E_F)$. Since Fe-Fe interaction is stronger than Fe-C interaction the Fe atoms show a tendency to form a cluster. However, for a different geometry, but the same θ , where two parallel Fe-chains are separated (hence Fe-Fe coupling is reduced) the net magnetic moment of the ground state did not change significantly, but $P(E_F)$ increased to $P(E_F)=0.82$. This result suggests that the spin-polarization is strongly dependent on θ as well as on the pattern of the decoration of the adsorbed TM atoms.

The calculations have been repeated by using different GGA functional, namely PBE[70] for the Fe-atomic chains adsorbed externally with $\theta=1/2$, 1, and 2. The use of PBE did not change the results obtained by using PW91. For example maximum changes in the binding energy has been 0.1, 0.1 and 0.2 eV for $\theta=1/2$, 1, and 2, respectively. The geometry and d_{C-Fe} calculated by two functionals are same but, μ values slightly change and become 2.4, 4.0, and 3.0 μ_B for $\theta=1/2$, 1, and 2, respectively for PBE.

4.2.1.3 Chromium

Cr atomic chains adsorbed on the (8,0) SWNT with $\theta=1/2$ and 1 give rise to metallic state for both types of spin carriers and result in negligible $P(E_F)$. However the induced μ is large. Bare chains of both $\theta=1/2$ and 1 have the same $\mu = 6\mu_B$ as that of free Cr atom in s^1d^5 configuration due to negligible

Cr-Cr interaction. The decrease in μ when Cr is adsorbed on SWNT is due to transfer of s -electrons into d -electrons. For $\theta = 2$ we obtained a significant $P(E_F)$ with $\mu = 4.4\mu_B$. Yagi *et al.*[115] reported $P(E_F)=29\%$ with $\mu = 3.2\mu_B$ for (14,0) suggesting that μ decreases with increase of nanotubes radius. The calculations by Yagi *et al.*[115] on the (6,6) and (8,8) armchair SWNT showed that a small gap opens for minority spin carriers and system becomes HM with 100% spin polarization with $\mu = 4\mu_B$. They obtained E_b less than 1 eV for both metallic and zigzag nanotubes which is consistent with our result indicating relatively weak interaction between Cr and SWNT. Duffy *et al.*[121] studied single Cr adsorption on graphene and reported ferromagnetic ground state with $\mu = 5.0\mu_B$

4.2.1.4 Cobalt

While the Co chains adsorbed on the (8,0) SWNT have ferromagnetic ground states with $\mu \sim 1.0 \mu_B$ for $\theta=1/2$ and 1, the magnetic moments corresponding to the bare Co chains ($\mu = 3.0 \mu_B$) are equal to that of single, free Co atom in the d^8s^1 configuration. This indicates that direct Co-Co interaction is almost negligible at distances larger than 4.26 \AA , but Co-C interaction reduces the strength of μ . The energy band analysis indicates that the Co atomic chains adsorbed on the (8,0) SWNT for $\theta = 1/2$ and 1 is semi-half metallic, namely the system is semiconducting for minority spin bands, but the band of majority spin states just touches E_F at the center of BZ. Moreover, the band originating from localized $3d_{\downarrow}$ state just below E_F contributes to the conductance under small bias and makes that spin polarization significant for minority spin carriers. For $\theta=2$, the system is metallic for both spin directions with high $P(E_F)$ in favor of minority spin carrier. The calculations by Yang *et al.*[114] indicated also significant spin polarization with $P(E_F)= 41\%$ with $\mu = 1.2\mu_B$ for the Co-chain adsorbed on the (14,0) SWNT for $\theta = 2$. The decrease of μ with increasing radius of zigzag nanotubes is consistent with the results obtained for V, Fe. The calculations concerning the interaction of Co atom with (4,4) and (8,8) metallic SWNTs at $\theta=1/2$ indicate that even complete polarization at E_F can be obtained.[123]

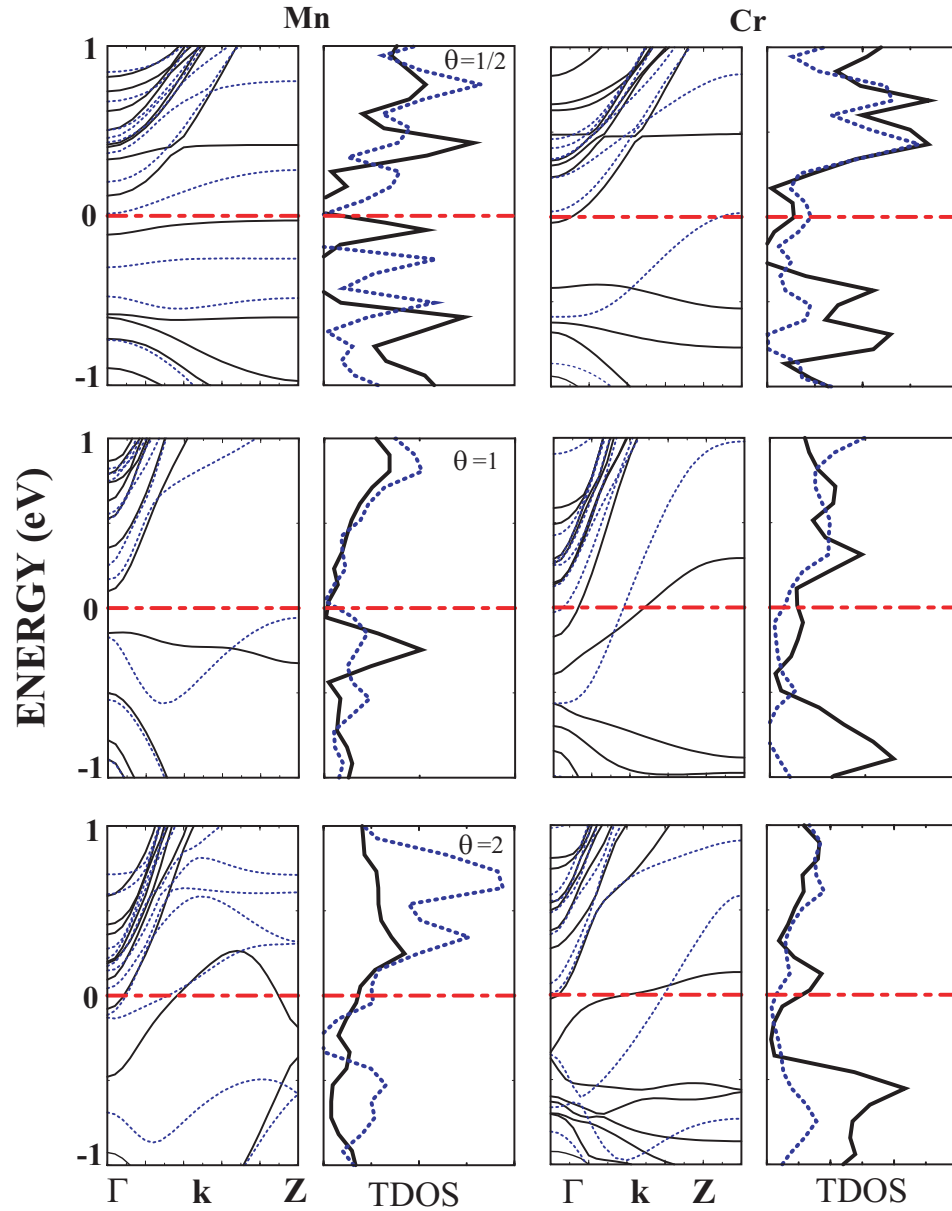


Figure 4. 3: The spin-dependent band structure and total density of states (TDOS) of Mn and Cr-chains adsorbed on the zigzag (8,0) SWNT for $\theta=1/2$, 1 and 2 geometries. Solid and dotted lines are for majority and minority spin states, respectively. The zero of energy is set to the Fermi level E_F .

4.2.1.5 Manganese

The Mn-chain adsorbed on the (8,0) SWNTs has ferromagnetic ground state for $\theta=1/2$, 1, and 2 geometries. The corresponding magnetic moments μ per atom are 5.5, 5.0, and 4.6 μ_B for $\theta=1/2$, 1, and 2, respectively. For $\theta=1/2$ geometry, the magnetic moment of SWNT+Mn chain system is even larger than that of free Mn atom in s^1d^6 configuration. Our PDOS analysis suggests that Mn-C interaction through the electron transfer from Mn 4s to Mn 3d and 4p is enhancing the spin alignment[106]. Even the calculations on the interaction of single Mn atom with graphene result in a similar charge transfer from Mn 4s to Mn 4p and 3d orbitals.[121] Bare Mn-chains corresponding to both $\theta=1/2$ and $\theta=1$ have magnetic moments equivalent to that of free Mn atom, since Mn-Mn interaction is almost negligible for $d_{Mn-Mn} > 4 \text{ \AA}$.

The band gap of the bare (8,0) SWNT increases upon the adsorption of the Mn-chain of $\theta=1/2$. The interesting point is that a band of majority spin states just touches the E_F at the Γ -point exhibiting a half semimetallic character. However, the system is semiconducting for $\theta=1$, but metallic for $\theta=2$ with small $P(E_F)$. For $\theta=2$, Fagan *et al.*[106] predicted similar optimized configuration with $\mu=4.2\mu_B$. Yang *et al.*[114] reported very high polarization, $P(E_F)=78\%$ with $\mu=3.6\mu_B$ for the case of Mn-chain adsorbed on the (14,0) SWNT according to $\theta=2$.

Finally, the general trends revealed from the above discussion can be summarized as: (i) The bond length d_{C-TM} ranges between 2.0 \AA and 2.5 \AA ; it does not exhibit significant variation with nanotube radius (R). However, d_{C-TM} slightly increases with increasing θ due to the increasing adatom-adatom coupling. (ii) The binding energy E_b , decreases as R increases. This is an expected result due to the curvature effect. E_b has the lowest value for Mn having half-filled d -shell in $3d^54s^2$ configuration. (iii) Generally μ decreases as R increases. Maximum of μ is obtained for Cr and Mn. The variation of μ and E_b with respect to the number of d -electrons, N_d , of the adsorbed TM atom is plotted in Fig. 4.4. Interestingly, different adsorption geometries corresponding to $\theta=1/2$, 1, and 2 display similar overall behaviors. The ground state magnetic moment μ has

a maximum value for $N_d = 5$ (corresponding to half-filling of the d -shell). In contrast, E_b shows a minimum at $N_d=5$. Earlier it has been shown that $E_b(N_d)$ passes through a two maxima for $N_d=2$ (Ti $3d^24s^2$ configuration) and $N_d=8$ (Ni in $3d^84s^2$ configuration).[109, 110] The behavior illustrated in Fig. 4. 4 is explained by using Friedel model.[109, 110, 122]

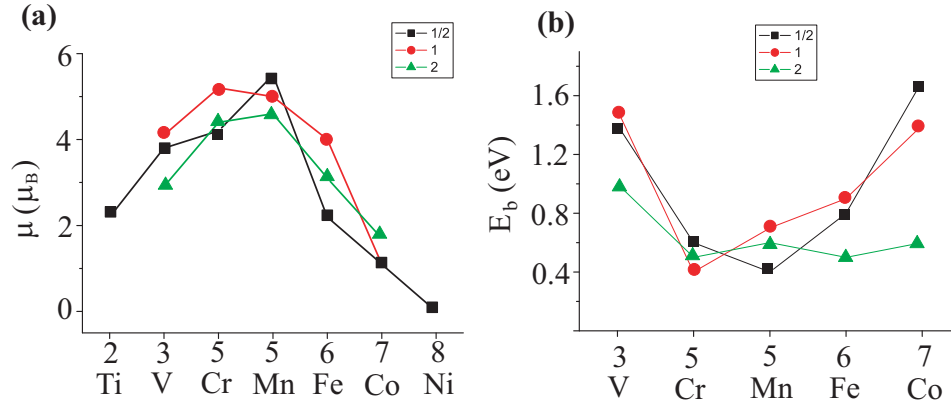


Figure 4. 4: The variation of magnetic moment, μ (a), and the binding energy, E_b (b) as a function of number of d -states for $\theta=1/2, 1$, and 2 for external adsorption.

4.2.2 Internal adsorption

The results obtained from the adsorption of Co, Fe, and V-chain for $\theta=1/2$ and 1 on the internal wall of the (8,0) SWNT are summarized in Table 4.2. The variation of d_{C-TM} , E_b , and μ with θ exhibit trends similar to those in the case of external adsorption. However, spin-polarization at E_F displays some differences from external adsorption. For example, while $P(E_F)$ is usually significant for external adsorption at $\theta = 1/2$, it is negligible for internal case. Similar to the external counter part, the ground state of internally doped (8,0) SWNT is ferromagnetic for all geometries. However, the band structure corresponding to the internal adsorption usually changes significantly for most of the cases. This

situation shows the effect of confinement on the interaction between TM and C. Both $\theta = 1/2$ and $\theta = 1$ geometries of adsorbed V-chains exhibit metallic character, but the high $P(E_F)$ calculated for the external doping case diminishes for $\theta=1/2$ and reduces to 0.22 for $\theta=1$.

The change in μ is more significant when Fe is adsorbed internally. For $\theta = 1/2$, while the Fe-chain externally doped is metallic with high $P(E_F)$, internally adsorbed system becomes semiconducting. On the other hand, for $\theta = 1$, the semiconducting system of the external adsorption case shows metallic behavior with $P(E_F)=0.62$ for the internal adsorption. The change in electronic structure as well as in $P(E_F)$ is again due to the hybridization of d -bands. Localized and almost dispersionless d -bands of external chains are dispersed for the internal case due to increased coupling. The overall shape of the band structures is similar, but near E_F changes become significant. For the (4,4) armchair SWNT, Yagi *et al.*[115] also found ferromagnetic ground state with the same adsorption geometry corresponding to $\theta = 1/2$. The atomic positions and E_b are very close for both case, but just a small increase in μ (from 3.0 to 3.1 μ_B) for the internal adsorption is pointed out.

As for Co, the semi-half metallic system becomes semiconducting for $\theta = 1/2$ and metallic for $\theta = 1$ with $P(E_F)=0.77$ in the case of internal adsorption. The change in the dispersion of the d -band of minority carriers determines the electronic properties and polarization of the system. The internal adsorption of Co atoms inside (4,4) and (8,8) armchair SWNT makes the system half-metallic.[115]

Briefly, in the internal adsorption, it is seen that geometry and d_{C-TM} do not change significantly with the type of TM atom. μ generally decreases for the internal adsorption (except for Co), since more $4s$ electrons are transferred to $3d$. As the strength of interaction changes, the value of E_b oscillates and hinders the derivation of a general rule. Nevertheless, the cases studied here clearly indicate that the polarization near E_F can also be manipulated by changing the doping from external to internal walls of SWNT.

	$\theta = 1/2$				$\theta = 1$			
	$d_{C-TM}(\text{\AA})$	$E_b(\text{eV})$	$\mu(\mu_B)$	$P(E_F)$	d_{C-TM}	$E_b(\text{eV})$	$\mu(\mu_B)$	$P(E_F)$
Co	2.0	1.2	1.0	-	2.0	1.6	1.4	0.77
Fe	2.2	0.4	2.3	-	2.1	0.4	2.3	-0.62
V	2.2	1.5	3.6	-	2.2	1.4	3.8	0.22

Table 4.2: The distance between TM and nearest neighbor C atom d_{C-TM} ; binding energy E_b ; magnetic moments μ per TM atom; polarization at Fermi level $P(E_F)$ of various chain structures of Co, Fe, and V atoms adsorbed inside the (8,0) SWNT for $\theta = 1/2$ and $\theta=1$. $P(E_F) < 0$ corresponds to $D(E_F, \downarrow) > D(E_F, \uparrow)$.

4.2.3 Other type of SWNTs

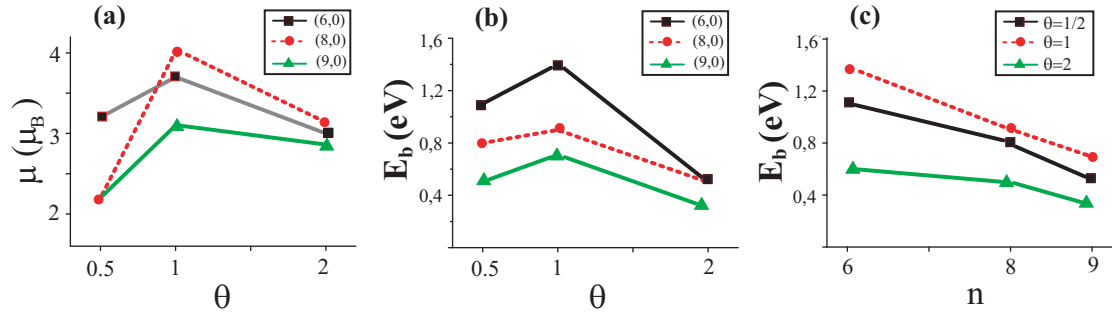


Figure 4. 5: Variation of the average magnetic moment μ and binding energy E_b of Fe-chain adsorbed on the external walls of zigzag $(n,0)$ SWNT ($n=6, 8,$ and 9) with the coverage geometry θ and tube index n . (a) μ versus θ ; (b) E_b versus θ ; (c) E_b versus n .

In addition to the zigzag (8,0) SWNT, we have analyzed the interaction of Fe with the (6,0) and (9,0) tubes which are chosen as prototype for $(n,0)$ (where n is the integer multiples of 3). The (6,0) SWNT is metallic due to the dipping of the π^* -singlet conduction band into the valence band as a result of curvature effect[123]. The (9,0) tube is semiconductor with very small band gap.[124] All Fe chains ($\theta=1/2, 1,$ and 2) have magnetic ground state. Variation of μ with θ is illustrated in Fig. 4. 5(a). θ as well as with the index of SWNT (n) are shown in Fig. 4. 5(b) and (c). It appears that $\mu(\theta)$ exhibits similar variation with θ for $n=6,8,$ and 9 . $\mu(\theta = 2)$ has comparable values for all three tubes which have

different radii. Owing to the curvature effect, E_b increases as n decreases (or R decreases). Their electronic band structures display also interesting properties. For (6,0), the system is metallic for all θ and shows high $P(E_F)$ except $\theta = 1$. For (9,0), the minority spin-bands just touch E_F and a small gap opens for majority spin bands and system becomes almost half-metallic with perfect spin-polarization at $\theta=1/2$ and 2. For $\theta = 1$, $P(E_F)$ is also high in favor of minority spin carriers but system becomes metallic for minority and majority spin-bands.

4.2.4 Adsorption on finite tubes

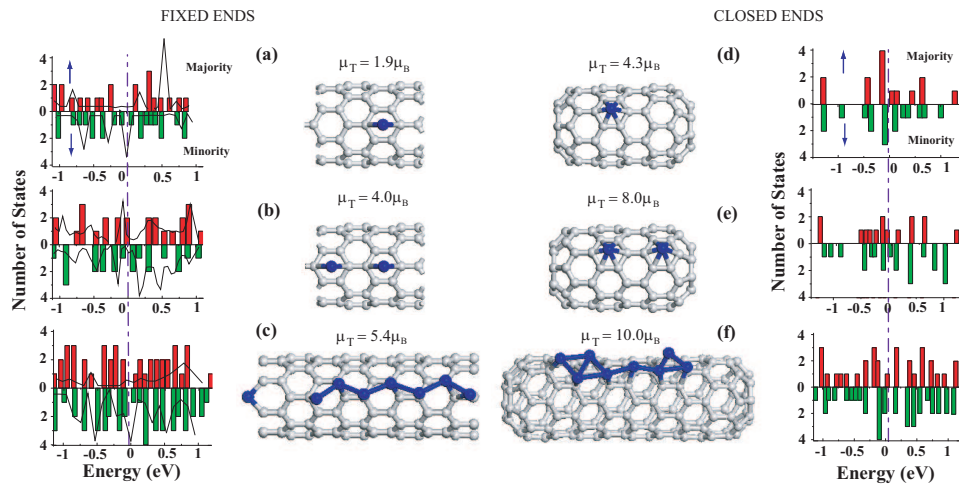


Figure 4. 6: Left panels: The number of states and corresponding structures of Fe atoms adsorbed on a finite (8,0) SWNT with open but fixed ends for (a) $\theta = 1/2$ (i.e 64 carbon atoms + one Fe), (b) $\theta = 1$ (i.e 64 carbon atoms + 2 Fe), and (c) $\theta = 2$ (i.e 128 carbon atoms + 8 Fe). The zero of energy is set to the Fermi level E_F . The total net magnetic moment for each finite tube, μ is shown. Total density of states of majority and minority spin states of infinite and periodic systems are also shown by continuous lines for $\theta=1/2$, 1, and 2. Right panels: Atomic configurations of Fe atoms adsorbed on the finite size (8,0) SWNT with closed ends. (d) One Fe atom is adsorbed on a tube consisting of 96 carbon atoms. (e) Two Fe atom are adsorbed on a tube consisting of 96 carbon atoms. (f) Eight Fe atoms are adsorbed on a tube of consisting of 160 carbon atoms. The calculated total magnetic moments μ_T and TDOS of majority and minority spin states are illustrated for each configuration.

While the study of periodic or infinite structures in previous sections may give an idea about the behavior of the systems in ideal cases, devices in real applications should have finite size and may be on substrates and/or connected to the leads. To examine the finite size effect, we considered Fe-chain adsorbed on the finite (8,0) tube. In the first model, we placed Fe atoms according to $\theta = 1/2$ and 1 geometry on a segment of the (8,0) SWNT consisting of 64 carbon atoms and for $\theta = 2$ case on a segment consisting of 128 carbon atoms. All tubes have open, but fixed ends. These finite models with fixed ends may be relevant for SWNTs connected to the electrodes from both ends. In this case the dangling bonds of free-end carbon atoms are combined with electrode states. Since this is a finite system all the parameters of calculation including supercell size are reoptimized as discussed in Methodology Chapter. Fe atoms remain stable for $\theta=1/2$ and 1 geometries, but one Fe atom is detached from the wire for $\theta = 2$ geometry and is attached to C atom at fixed ends. For a finite but longer system this effect will be minute. The ground state of all the systems are found to be ferromagnetic with total magnetic moments, $\mu_T = 1.9, 4.0,$ and $5.4 \mu_B$ for $\theta = 1/2, 1,$ and $2,$ respectively. Magnetic moment per Fe decreased with increased Fe-Fe interaction at $\theta = 2$. The results indicate that ferromagnetic ground state will be conserved for finite systems. When the number of states near E_F is compared with TDOS of infinite counter parts (see Fig. 4. 6) we also notice some changes in the distribution of spin states. These changes occur, since firstly, the electronic structure of bare nanotube changes due to fixed open ends. Secondly, the interaction between Fe and C atoms at both ends affects the electronic structure. Nevertheless, as the length of a finite-size system increases, the discrete electronic states are expected to converge to the spin dependent TDOS of infinite and periodic system. On the other hand, the fact that the contribution of minority spin states is relatively larger than that of majority spin states near E_F for $\theta = 1/2$ and 2 is similar to their infinite counter parts yielding high $P(E_F)$.

In the right panels of Fig. 4. 6, we present more realistic systems for finite-size devices. Here we consider slightly longer segments of the (8,0) SWNT and let the carbon atoms at both ends relax to close. These segments comprises 96 carbon

atoms for $\theta = 1/2$ and $\theta = 1$, but 160 carbon atoms for $\theta = 2$. By adsorbing Fe atoms similar to the cases of $\theta=1/2$, 1, and 2, we examined geometry and then calculated spin-polarized electronic structure and magnetic moments. While Fe atoms remain stable for $\theta=1/2$ and 1, the Fe chain which is composed of 8 atoms for $\theta = 2$ has deformed due to end effects and strong Fe-Fe interaction. For longer SWNTs this effect is expected to be minute and in any case the ferromagnetic ground state is conserved with $\mu_T = 10\mu_B$ like the stable low doping cases $\theta=1/2$ and 1. The energy level diagram of spin states and total magnetic moments of those Fe adsorbed needles are strongly dependent on the number of Fe atoms, and on their adsorption geometry. Moreover, we see dramatic changes between left panels (corresponding to fixed ends) and right panels (corresponding to closed ends). The spin-polarization and the ferromagnetic ground states are expected to be maintained even after these finite systems are connected to the non-magnetic metal electrodes from both sides. Depending on the character of the contact and type of the metal, the discrete levels can shift and can form resonances. Under an applied electric field these ferromagnetic needles behave as a resonant tunnelling device, as well as a spin valve for different spin directions. The size of the SWNT segment and the geometry of decoration of TM atoms, as well as their type can be relevant parameters to engineer nano-spintronic devices.

Chapter 5

Silicon Nanowires

The fabrication of stable and oxidation resistant Si nanowires (SiNW) at small diameters[54] (1-7 nm) has taken much interest. These wires display interesting electronic properties such as band gap variation with diameter. They can be used in electronic and optical applications like FETs [55], LEDs [56], lasers [57] and interconnects. The discovery of room temperature ferromagnetism in Mn⁺-doped SiNW [58] is another major development. Once combined with advanced silicon technology, these predicted properties can be realizable making "known silicon" again a potential material with promising nanoscale technological applications in spintronics and magnetism.

In this last chapter, firstly, electronic and mechanical properties and then stability of bare and hydrogen saturated (H-SiNW) of various radius are investigated. Then, spin-dependent electronic and magnetic properties of these structures when doped with different transition metal (TM) elements are studied. The possibility of half-metallic character is searched and its robustness is analyzed.[125]

5.1 Methodology

The results are obtained from first-principles plane wave calculations [81] (using a basis set up to kinetic energy of 400 eV) within DFT using the parameters (See Chapter 2). All calculations for paramagnetic, ferromagnetic and antiferromagnetic states are carried out using ultra-soft pseudopotentials [75] and confirmed by using PAW potential [76]. All atomic positions and lattice constants are optimized by using the conjugate gradient method where total energy and atomic forces are minimized. The convergence for energy is chosen as 10^{-6} eV between two steps, and the maximum force allowed on each atom is 10^{-3} eV/Å.

5.2 Bare and H-passivated Si Nanowires

In this section, firstly the bare and H-terminated Si nanowires oriented along [001] direction having different diameter (or different number of Si atoms in their unit cell) are characterized. The bare Si nanowire oriented along [001] direction and having N Si atoms in the primitive unit cell is specified by SiNW(N). Similarly, a nanowire with all dangling bonds on the surface passivated by H atom is specified by H-SiNW(N). Initially, bare SiNWs are cut in rod-like forms from the ideal bulk Si crystal. Subsequently, the initial atomic structure having ideal bulk configuration is relaxed to yield the minimum total energy and atomic forces smaller than 0.05 eV/Å. Hydrogen passivation of bare Si nanowires is achieved by termination of the dangling bonds of Si atoms (which had nearest neighbor coordination less than four Si atoms) by H atom and subsequently by optimization of the whole structure. This way another family of SiNWs are created. In the following discussion it will be clear that the properties of bare and H-SiNWs are quite different. This section presents a comparative study of atomic structure, and electronic band structure and elastic properties of these nanowires together with a comprehensive discussion of the relevant theoretical studies.

5.2.1 Atomic Structure and energetics

Figure 5. 1 shows the optimized atomic structures of bare SiNWs and H-SiNWs investigated in this section. The wire geometries having 21, 25, 57, 61, 81 Si atoms in the primitive unit cell are considered. Among these wires nanowires 21, 57 and 81 have rather round cross section, while those 25 and 61 have square-like cross section.

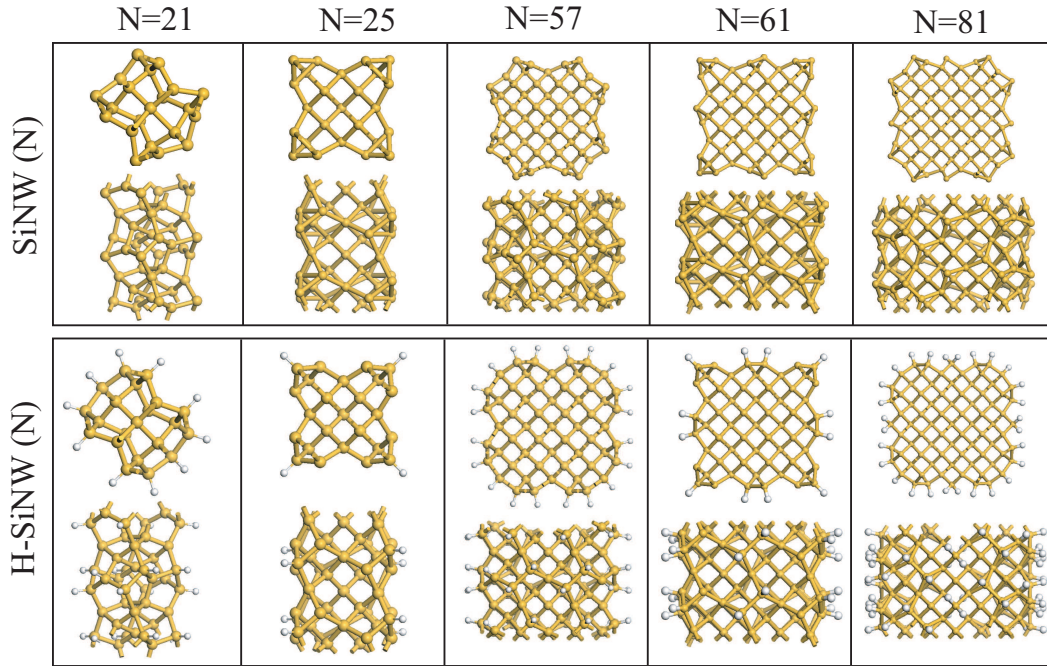


Figure 5. 1: Upper panels: Top and side views of optimized atomic structures of bare SiNW(N) grown along [001] direction. Lower panels: Same for H-SiNW(N) with $N=21, 25, 57, 61$ and 81 . Large and small balls indicate Si and H atoms, respectively. Side views consist of two primitive unit cells.

The cohesive energy (per Si atom) of the bare SiNWs are calculated by $E_c = E_T[Si] - E_T[SiNW(N)]/N$, in terms of the total energy of free Si atom and the total energy of bare SiNW(N) having optimized structure. According to this definition $E_c > 0$ indicates that the structure is stable with respect to constituent free atoms. The cohesive energy relative to the bulk crystal Si, $E'_c = E_T[BulkSi] - E_T[SiNW(N)]/N$, is calculated by replacing the free atom energy with the total

SiNW(N)	$c_o(\text{\AA})$	$R_{max}(\text{\AA})$	$E_c(\text{eV})$	$E'_c(\text{eV})$	$E_{gap}(\text{eV})$	$\kappa(\text{eV/cell})$
N=21	5.68	8.3	4.05	-0.59	0.6	133
N=25	5.33	10.76	4.13	-0.51	M	161
N=57	5.42	15.59	4.24	-0.40	M	339
N=61	5.38	18.43	4.26	-0.38	M	375
N=81	5.4	18.73	4.27	-0.37	M	432

Table 5.1: The binding energies (in eV) with respect to atomic and bulk energies of various metals.

H-SiNW(N)	$c_o(\text{\AA})$	$R_{max}(\text{\AA})$	$E_b(\text{eV})$	$E'_b(\text{eV})$	E_{gap}	$\kappa(\text{eV/cell})$
N=21	5.85	11.03	4.14	0.74	0.7	172
N=25	5.45	13.20	4.22	0.82	1.1	254
N=57	5.39	17.76	4.28	0.88	1.7	394
N=61	5.43	20.90	4.34	0.94	1.1	509
N=81	5.40	21.6	4.28	0.88	1.57	532

Table 5.2: The binding energies (in eV) with respect to atomic and bulk energies of various metals.

energy of bulk equilibrium crystal per atom, *i.e.* $E_T[BulkSi]$. The binding energy of hydrogen with respect to the free H atom is also of interest and is calculated by, $E_b = (N_H E_T[H] + E_T[SiNW(N)] - E_T[H - SiNW])/N_H$, in terms of the total energy of structure optimized bare SiNW(N) and H-SiNW(H) terminated by N_H hydrogen atom and the energy of free H atom, $E_T[H]$. The binding energy of hydrogen relative to H_2 molecule, E'_b , is obtained if $E_T[H]$ is replaced by $E_T[H_2]/2$. Calculated structure parameters, such as the lattice constant along the wire axis c_o and maximum radius of the cross section; cohesive energy relative to free Si atom and Si crystal, binding energy of H atom are presented in Table 5.1 and Table 5.2.

It is seen that the lattice constant c_o of bare and H-terminated SiNW(N) decreases with increasing N. Namely, the lattice constant is large for small N, but approaches to the lattice constant of bulk Si. The cohesive energy relative to the free Si atom as well as bulk Si show a reverse trend. E_c is small for small cross section but increases with increasing N.

Atomic structure of SiNWs has been analyzed by comparing the distribution of interatomic distances between various atoms (up to sixth nearest neighbor) with that of ideal crystal. In Fig. 5. 2 the distribution of interatomic distances are plotted for bare SiNW(N) and H-SiNW(N) for N=21, 57 and 81. Similar analysis is illustrated in Fig. 5. 3 for N=25 and 61, which have rather square cross section.

The deviations from ideal case is large for small N. The distribution of the first nearest neighbor distance is always sharp for all N. Significant deviations from the second, third, etc nearest neighbor distances of ideal bulk crystal are observed. In particular, second nearest neighbor distance exhibits a wide distribution. The deviation from ideal case decreases upon the hydrogen termination of dangling bonds. H-SiNW(81) is the structure, which comes closest to its ideal structure.

5.2.2 Elastic properties

The elastic properties of a SiNW can be deduced by calculating its elongation under a uniaxial tensile stress along the axis of the wire. The response of the wire to a uniaxial tensile stress can be formulated by the expression, $X_x = \kappa e_{xx}$, where κ is Young's modulus and e_{xx} is the strain along x -direction. κ can be related to the elastic stiffness constants, C_{11} , C_{12} in cubic crystals. However, since SiNWs studied here have high surface to volume ratio, it is better to calculate κ directly from the relation, $\kappa = \partial E_T / \partial c_o$. To this end we calculated self-consistent total energy, $E(T)$ as a function on the lattice constant c_o by relaxing all atomic positions under that constraint. The variation of κ with N is presented in Fig. 5. 4 for bare and hydrogen terminated SiNWs. One captures following general trends from this figure: (i) The stiffness and also strength of a bare SiNW increases upon hydrogen termination of dangling bonds. (ii) For bare SiNW κ increases with N almost linearly. SiNW(N) with N=25 and 61 show slight deviation from the linear relation due to perhaps their square-like cross section. The deviation from the linearity is enhanced in the case of H-SiNW(N)s. As compared to hydrogen terminated SiNWs with round cross section (N=21, 57 and 81) hydrogen terminated wires with square-like cross section (N=25 and 61) fall in a different

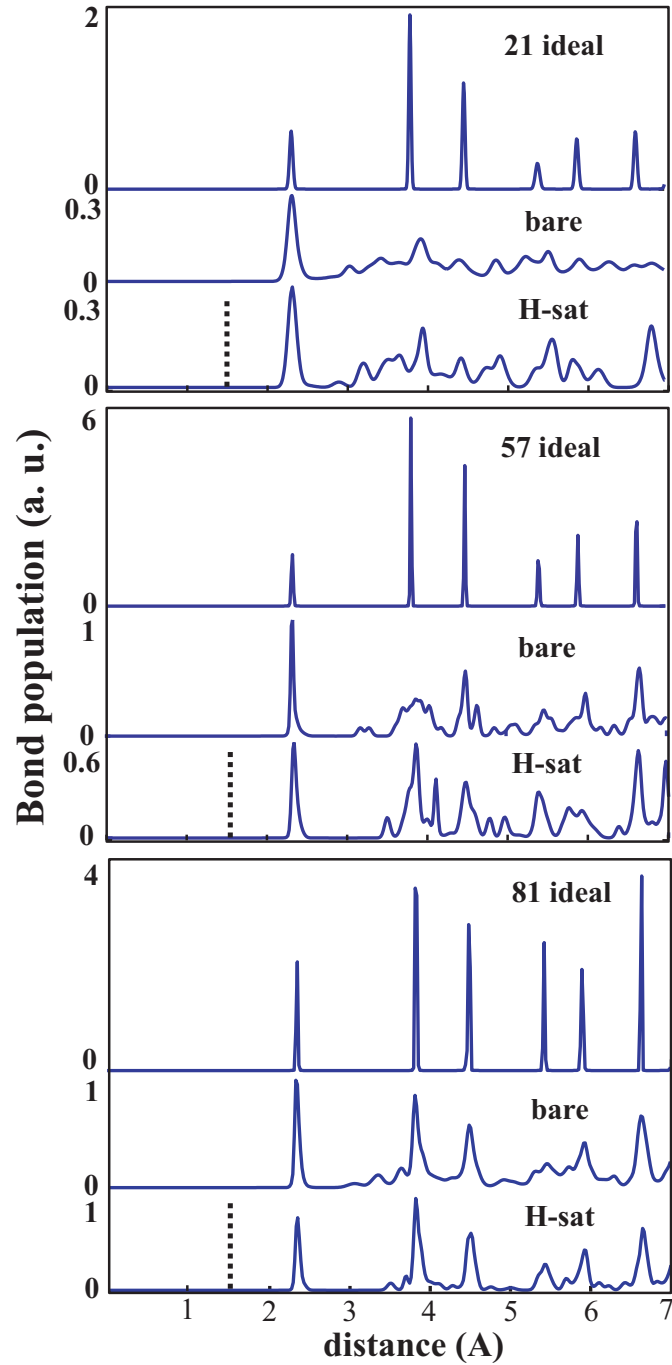


Figure 5. 2: Distribution of interatomic distances of structure-optimized bare SiNW(N) (bottom curve in each panel) and H-SiNW(N) (middle curve) for $N=21$, 57 and 81 . Upper curve with numerals indicate first, second, third, fourth etc nearest neighbor distances calculated for bulk Si crystal in equilibrium.

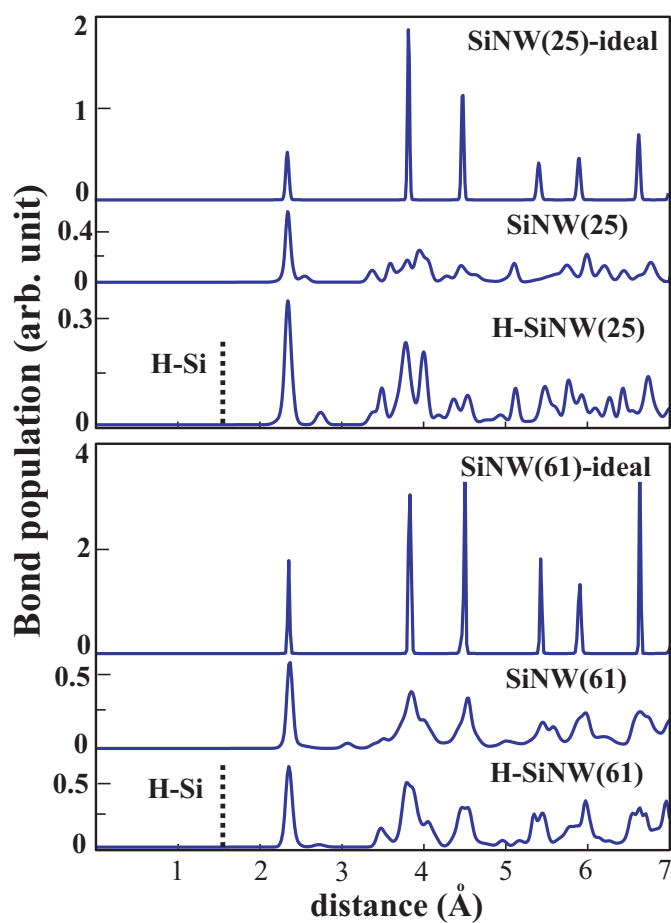


Figure 5. 3: Distribution of interatomic distances of structure-optimized bare SiNW(N) (bottom curve in each panel) and H-SiNW(N) (middle curve) for $N=25$ and 61. Upper curve with numerals indicate first, second, third, fourth etc nearest neighbor distances calculated for bulk Si crystal in equilibrium.

category. It appears that upon H-termination the strength of the latter wires increases more relative to the wires with round cross section. As with the electronic structure, this results point to the fact that the mechanical properties are sensitive to the geometry of the SiNW at small diameter.

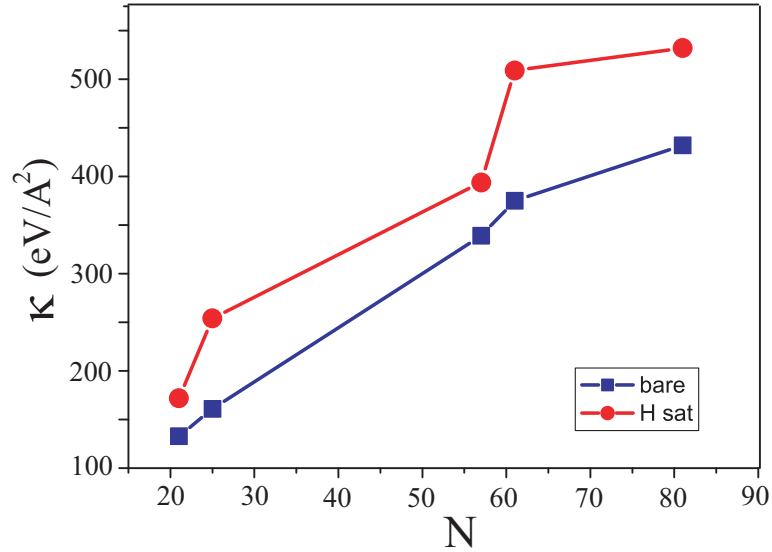


Figure 5. 4: Variation of elastic strength (Young's modulus) κ with number of atoms N in the primitive unit cell of the bare and hydrogen terminated SiNW(N)s. Wires with $N=21$, 57 and 81 have round cross section, whereas wires with $N=25$ and 61 have square-like cross section.

5.2.3 Stability analysis

It should be noted that the global minimum for Si is the crystal in diamond structure; nanowires described above are only local minima in the Born-Oppenheimer surface. In this respect the stability of the wire structures presented in Fig. 5. 1 is of prime importance. A thorough analysis of the stability of a SiNW is necessary before one aims at its possible application as an electronic device. Firstly, we doubled the unitcell size ($c=2c_o$ where c_o is the lattice constant of SiNW or H-SiNW) and slightly distort Si atoms from their equilibrium positions in order to remove any constraint. That reoptimizations results in the original, undistorted structures indicating stability. The stability is further tested by *ab initio*

molecular dynamics calculations at very high temperature. The calculations are performed at 1000K for 1 ps (which is long enough for MD calculations) for both SiNW and H-SiNWs with four unitcell. All the wires under consideration remain stable with small deformations.

5.2.4 Energy band structure

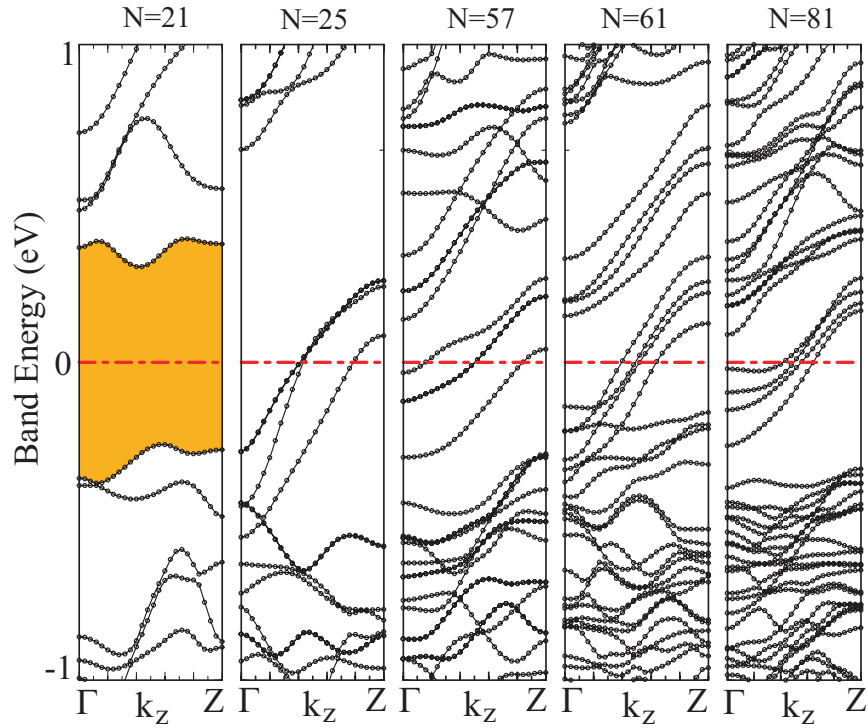


Figure 5. 5: Energy band structures of SiNW(N) for N=21, 25, 57, 61, 81. Shaded area is the band gap. Zero of band energies are set at the Fermi level.

Bare SiNWs are usually metallic due to the unsaturated bonds on the surface. These dangling bonds form surface bands, which occur in the band gap of the semiconductor and pin the Fermi level. In this respect the dangling bond surface states are localized at the surface. In Fig. 5. 5 the energy band structures calculated for bare SiNWs confirm this argument except SiNW(21), which is semiconducting with band gap of $E_G = 0.6$ eV. Owing to the even number of dangling bonds, the related bands of SiNW(21) are filled. Moreover, due to the

very small diameter of cross section the dangling bond surface states mix with bulk like bound states. On the other hand, SiNW(N) for $N=25, 57, 61$ and 81 are metallic. Since these metallic wires have n multiple bands crossing the Fermi level, their ballistic quantum conductance given by $G = nh/2e$ is high and supports their use as conducting interconnect between molecular or nanoelectronic devices. However, all these nanowires become semiconductor upon the termination of dangling bonds by H-atom as shown in Fig. 5. 6.

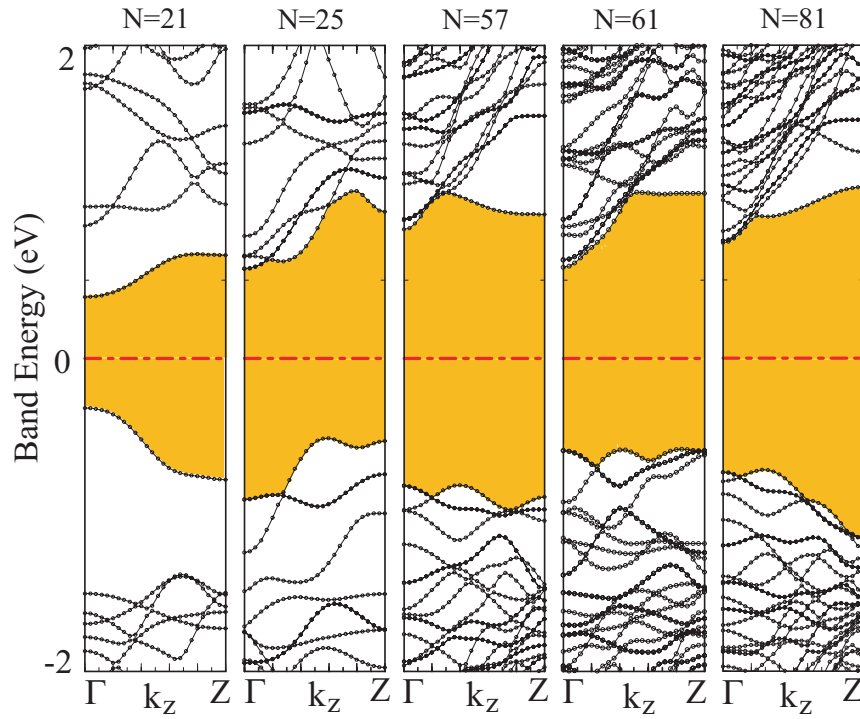


Figure 5. 6: Energy band structures of H-SiNW(N) for $N=21, 25, 57, 61, 81$. Shaded area is the band gap. Zero of band energies are set at the Fermi level.

5.3 Functionalization of SiNWs by Transition Metal Atoms

The adsorption of a single TM (TM=Fe, Ti, Co, Cr, and Mn) atom per primitive cell, denoted by $n = 1$, have been examined for different sites (hollow, top, bridge

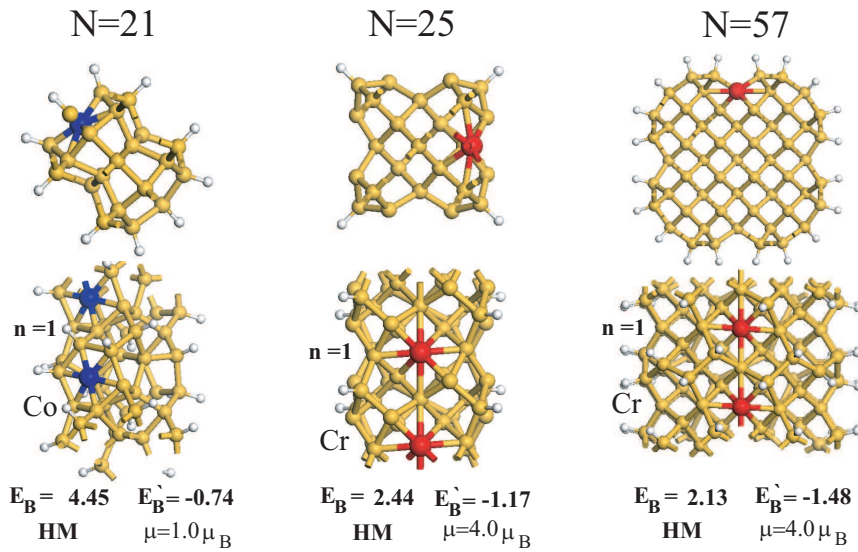


Figure 5. 7: Top and side views of optimized atomic structures of single TM atom adsorbed H-SiNW (per primitive cell, $n = 1$). Binding energies in regard to the adsorption of TM atoms, i.e. E_B , E'_B for $n = 1$ are defined in the text. μ denotes the net magnetic moment per primitive unit cell. Small, large-light and large-dark balls represent H, Si and TM atoms, respectively.

etc) on the surface of H-SiNW(N) for N=21, 25 and 57. In Fig. 5. 7, only the most energetic adsorption geometry for a specific TM atom for each N, which results in a HM state, is presented. These are H-SiNW(21)+Co, SiNW(25)+Cr and SiNW(57)+Cr. These nanowires have ferromagnetic ground state, since their energy difference between calculated spin-unpolarized and spin-polarized total energy, i.e. $\Delta E^m = E_T^{su} - E_T^{sp}$ is positive. We calculated $\Delta E^m = 0.04, 0.96$ and 0.99 eV for H-SiNW(21)+Co, H-SiNW(25)+Cr and H-SiNW(57)+Cr, respectively. Spin-polarized calculations have been carried out by starting with different initial magnetic moment values and subsequently by releasing them. Whether antiferromagnetic ground state exists in H-SiNW(N)+TM's has been explored by using supercell including double primitive cells. Moreover, these wires have integer number of unpaired spin in their primitive unit cell. The binding energy of TM atoms (E_B) on H-SiNWs is high and involves significant charge transfer from TM atom to the wire. This is in contrast to usually weak binding of TM atoms on single-wall carbon nanotubes which can lead clustering [109, 110]. Binding energy corresponding to $n=1$ is calculated by the following expression, $E_B = E_T[H - SiNW(N)] + E_T[TM] - E_T[H - SiNW(N) + TM]$ in terms of the total energy of optimized H-SiNW(N) and H-SiNW(N)+TM and the total energy of the string of TM atoms having the same lattice parameter c_o as H-SiNW(N)+TM; all calculated in the same supercell. Hence E_B can be taken as the binding energy of single isolated TM atom, since the coupling among adsorbed TM atoms has been subtracted. For $n > 1$, $E_T(TM)$ is taken as the free TM atom energy, and hence \bar{E}'_B includes the coupling between TM atoms. For this reason $\bar{E}'_B > 0$ for H-SiNW(21)+Co at $n=12$. Mulliken analysis indicates that the charge transfer from Co to H-SiNW(21) is 0.5 electrons. The charge transfer from Cr to H-SiNW(25) and H-SiNW(57) is even higher (0.8 and 0.9 electrons, respectively). Binding energies of adsorbed TM atoms relative to their bulk crystals (E'_B) are negative and hence indicate endothermic reaction. Due to very low vapor pressure of many metals, it is probably better to use some metal-precursor to synthesize the structures predicted here.

The band structures of HM nanowires are presented in Fig.5. 8. Once

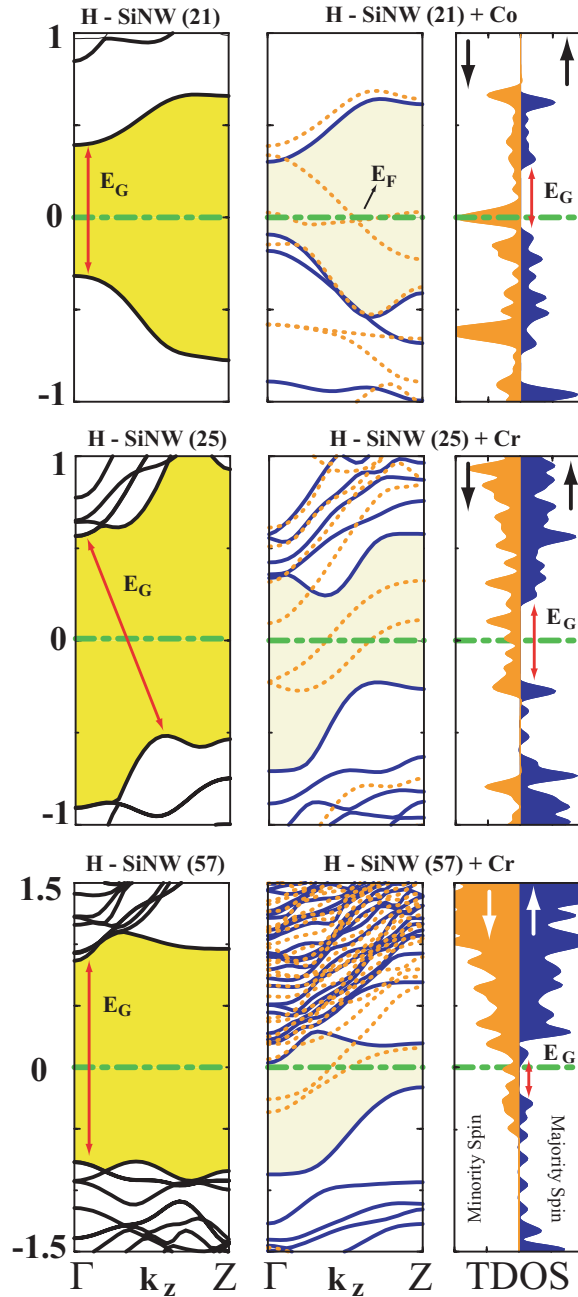


Figure 5. 8: Band structure and spin-dependent total density of states (TDOS) for $N=21, 25$ and 57 . Left panels: Semiconducting H-SiNW(N). Middle panels: Half-metallic H-SiNW(N)+TM. Right panels: Density of majority and minority spin states of H-SiNW(N)+TM. Bands described by continuous and dotted lines are majority and minority bands. Zero of energy is set to E_F .

a Co atom is adsorbed above the center of a hexagon on the surface of H-SiNW(21) the spin degeneracy is split and whole system becomes magnetic with a magnetic moment of $\mu=1 \mu_B$ (Bohr magneton per primitive unit cell). Electronic energy bands become asymmetric for different spins: Bands of majority spins continue to be semiconducting with relatively smaller direct gap of $E_G=0.4$ eV. In contrast, two bands of minority spins, which cross the Fermi level, become metallic. These metallic bands are composed of Co-3d and Si-3p hybridized states with higher Co contribution. The density of majority and minority spin states, namely $D(E, \uparrow)$ and $D(E, \downarrow)$, display a 100% spin-polarization $P = [D(E_F, \uparrow) - D(E_F, \downarrow)] / [D(E_F, \uparrow) + D(E_F, \downarrow)]$ at E_F . H-SiNW(25)+Cr is also HM. Indirect gap of majority spin bands has reduced to 0.5 eV. On the other hand, two bands constructed from Cr-3d and Si-3p hybridized states cross the Fermi level and hence attribute metallicity to the minority spin bands. Similarly, H-SiNW(57)+Cr is also HM. The large direct band gap of undoped H-SiNW(57) is modified to be indirect and reduced to 0.9 eV for majority spin bands. The minimum of the unoccupied conduction band occurs above but close to the Fermi level. The net magnetic moment is $4 \mu_B$.

We note that DFT underestimates the band gap of H-SiNW [79]. In the case of HM, H-SiNW+TM presented in Fig. 5. 8, the lowest conduction band and highest valence band are reminiscent of those of H-SiNW; the shrunk band gap still attributes a semiconducting behavior for majority spins. As for the metallic minority spin bands in the gap, they are reminiscent of the linear TM-chain having the same lattice parameter as H-SiNW+TM, except that their dispersions increase due to indirect TM-TM coupling through Si atoms. Under uniaxial compressive strain the minimum of the conduction band of majority spin states rises above the Fermi level. Conversely, it becomes semi-metallic under uniaxial tensile strain. Since conduction and valence bands of both H-SiNW(21)+Co and H-SiNW(25)+Cr are away from E_F , their HM behavior is robust under uniaxial strain. The form of two metallic bands crossing the Fermi level eliminates the possibility of Peierls distortion. Nevertheless, HM ground state of SiNWs is not common to all adsorbed TM atoms. For example H-SiNW(N)+Fe is consistently ferromagnetic semiconductor with different $E_{G,\uparrow}$ and $E_{G,\downarrow}$. H-SiNW(N)+Mn(Cr)

can be either ferromagnetic metal or HM depending on N.

5.3.1 Curie Temperature

In order to understand whether the predicted half-metallic character still remains close to room temperature, the Curie temperature is estimated by Heisenberg model and magnon theory.[73]

The electrostatic energy of a system depends on the relative orientation of the spins. The difference in energy when spins are parallel or antiparallel defines the exchange energy:

$$U = -2JS_iS_j \quad (5. 1)$$

where J is the exchange integral and $S_{i,j}$ are electrons spins of interacting atoms. An approximate connection between the exchange integral J and Curie temperature T_C can be established. Suppose that the atom under consideration has z nearest neighbors, each connected with the central atom by the interaction J . For more distant neighbors J is taken as zero. The mean field theory results:

$$J \simeq \frac{3k_B T_C}{2zS^2} \quad (5. 2)$$

In our system the spins are located on TM atoms so using magnon approach the exchange energy (U) will then be equal to $4JS^2$ which is calculated as the energy difference of antiferromagnetic (the spins on nearest TM atoms are antiparallel) and ferromagnetic (the spins on nearest TM atoms are parallel) states. As we can calculate U instead of J in our calculations, Equ. 5. 2 is reformulated using U :

$$T_C = \frac{zU}{6k_B} \quad (5. 3)$$

where $z=1$ for the structures under consideration. Using U calculated with PAW

potential, we estimated Curie temperature of half-metallic H-SiNW+TMs as $T_C \simeq 10, 290, \text{ and } 700 \text{ K}$ for $N=21, 25, \text{ and } 57$, respectively.

5.3.2 LDA+U

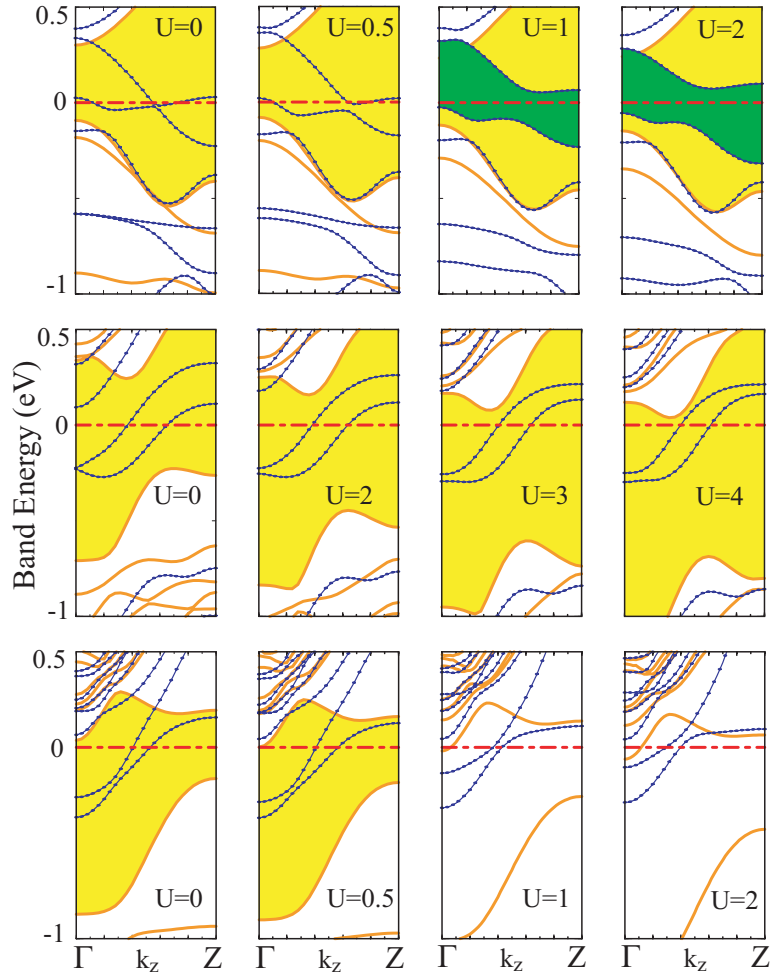


Figure 5. 9: The energy band structure variation of H-SiNW(21)+Co (up panel), H-SiNW(25)+Cr (mid-panel) and H-SiNW(57)+Cr (down panel) with respect to U value.

To see whether spin-dependent GGA properly represents localized d -electrons or possible on-site repulsive Coulomb interaction destroys the HM, we also carried out LDA+U [126] calculations. We found that insulating and metallic bands of

opposite spins coexist up to high values of repulsive energy ($U=4$) for $N=25$ as shown in Fig. 5. 9. For $N=57$, HM persists until $U\sim 1$. Clearly, HM character of H-SiNW+Cr revealed in Fig.5. 7 is robust and unique behavior for these structures. For H-SiNW(21)+Co, the metallic bands split as U value increases and the half-metallic character (also metallicity) is destroyed. The calculated T_C also indicated fragility of HM character for H-SiNW(21)+Co.

5.3.3 High TM Coverage of SiNWs

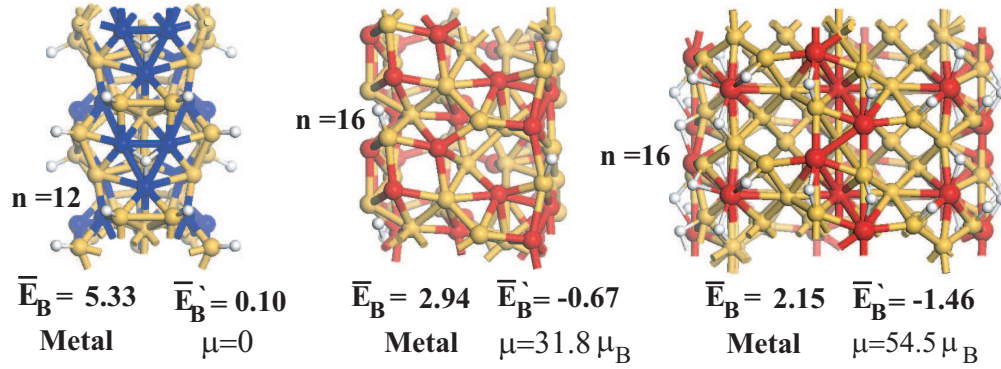


Figure 5. 10: Side views of optimized atomic structures of H-SiNWs covered by n TM atoms. \bar{E}_B , \bar{E}'_B are average binding energy values for $n > 1$ and are defined in the text. μ denotes the net magnetic moment per primitive unit cell. Small, large-light and large-dark balls represent H, Si and TM atoms, respectively.

Finally, we note that HM state predicted in TM-decorated H-SiNWs occurs in perfect structures; complete spin-polarization may deviate slightly from $P=100\%$ due to the finite extent of devices. Even if the exact HM character corresponding to $n = 1$ is disturbed for $n > 1$, the possibility that some H-SiNWs having high spin-polarization at E_F at high TM coverage can be relevant for spintronic applications. We therefore investigated electronic and magnetic structures of H-SiNW+TM for $n > 1$ as described in Fig. 5. 10.

H-SiNW(25) is ferromagnetic for different level of Cr coverage and has high net magnetic moment. For example, $n = 8$ can be achieved by two different geometries; both geometries are ferromagnetic with $\mu=19.6$ and $32.4 \mu_B$ and

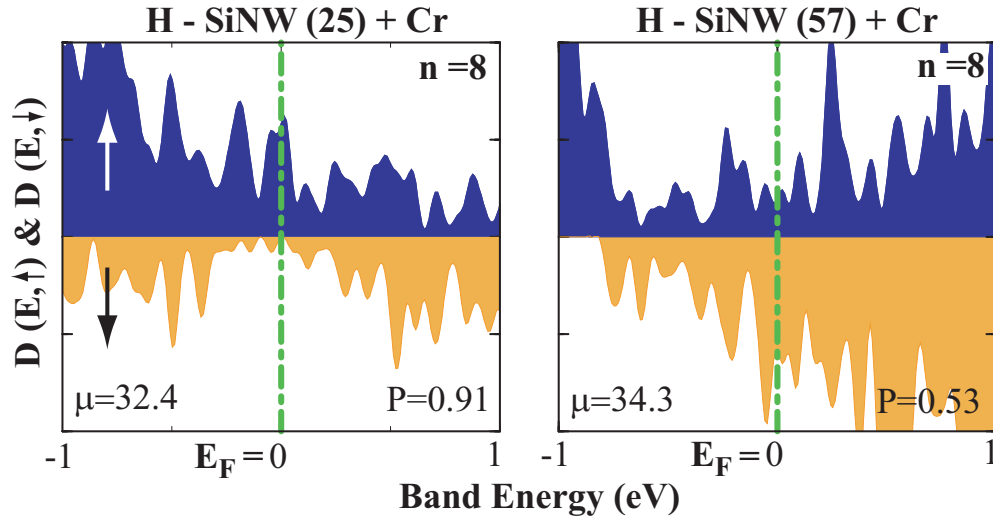


Figure 5. 11: $D(E, \downarrow)$, density of minority (light) and $D(E, \uparrow)$, majority (dark) spin states. (a) H-SiNW(25)+Cr, $n = 8$; (b) H-SiNW(57)+Cr, $n = 8$. P and μ indicate spin-polarization and net magnetic moment (in Bohr magnetons per primitive unit cell), respectively.

are metallic for both spin directions. Interestingly, while P is negligible for the former geometry, the latter one has $P = 0.91$ and hence is suitable for spintronic applications (See Fig. 5. 11). Similarly, Cr covered H-SiNW(57) with $n = 8$ and 16 are both ferromagnetic with $\mu = 34.3$ ($P = 53$) and $\mu = 54.5 \mu_B$ ($P = 0.33$), respectively. The latter nanostructure having magnetic moment as high as $54.5 \mu_B$ can be a potential nanomagnet. Clearly, not only total magnetic moment, but also the spin polarization at E_F of TM covered H-SiNMs exhibits interesting variations depending on n , N and the type of TM.

Chapter 6

Conclusions

In this study, new carbon and silicon-based nanomaterials which possess novel spintronic properties are systematically investigated. The obtained results can be briefly summarized in three groups.

First of all, the spin-dependent electronic, magnetic, and transport properties of atomic chain structures composed of carbon and transition metals, TM-C_n-TM molecules, are studied using first-principles methods. Synthesis of the linear structures of these finite atomic chains is energetically feasible, and they are stable even at elevated temperatures. The indirect exchange interaction of the TM atoms mediated by the carbon atomic chain determines whether the F or AF alignment of atomic moments leads to a lower energy. The ground state configuration and the total magnetic moment of the structures are determined by the number of carbon atoms in the spacer, and the type of the TM atom. The size-dependent variations of the physical properties of such systems exhibit several distinct forms, including regular alternations for Ti, V, Mn, Cr, Fe, and Co, and some irregular forms for Sc and Ni cases. The underlying mechanism of such diverse variations are modelled by a tight-binding model. The transport properties of these structures are also investigated. The conductance of TM-C_n-TM molecules when connected to metallic electrodes shows a strong spin-valve effect.

Secondly, a systematic analysis for the stability, atomic, electronic, and magnetic properties of TM atomic chains adsorbed on the external and internal wall of the SWNT is presented. For the sake of comparison we also considered bare TM chains by removing SWNT. The effects of coverage, geometry of the adsorbed chain configuration and the size of the tube on the magnetic and electronic properties have been investigated. We found that all adsorbed chains have ferromagnetic ground state. The coupling among the adsorbed TM atoms and the charge transfer between adsorbed TM and nearest carbon atom of SWNT play an important role in determining the resulting magnetic moment. Usually, the magnetic moment of the free TM atom is reduced upon the adsorption. We found that high spin polarization at the Fermi level can be obtained by the adsorption of V- and Fe-chains on the (8,0) SWNT at specific geometries. The polarization values achieved as high as 90% are expected to be suitable for nanospintronic application. Interesting variation of the magnetic moment and binding energy with the number of filled d -electrons of the adsorbate have been revealed. The dependence of the magnetic properties, in particular spin-polarization, on the radius and band gap of the zigzag tubes are further investigated by considering TM-chain adsorbed (6,0) and (9,0) SWNTs.

The spin-dependent electronic structure and the net magnetic moment calculated for finite-size systems are found to be different from infinite and periodic systems. Our results suggest that these finite size tubes holding TM atoms can be used as a nanomagnet and can perform as spin-valve or spin-dependent resonant-tunnelling devices when they are connected to the metal electrodes from their both ends. It is demonstrated that the semiconducting carbon nanotubes constitute a suitable substrate to hold transition metal chains and metallic leads to form nanoscale spintronic devices.

Finally, bare and hydrogen saturated silicon nanowires and their interaction with TM atoms are investigated. Hydrogen passivated SiNWs can exhibit half-metallic state when decorated with certain TM atoms. Resulting electronic and magnetic properties depend on the type of adsorbed TM atom, as well as on the diameter of the nanowire. When covered with more TM atoms, perfect

half-metallic state of H-SiNW is disturbed, but for certain cases, the spin polarization at E_F continues to be high. High magnetic moment obtained at high TM coverage is another remarkable result which may lead to the fabrication of nanomagnets for various applications. Briefly, functionalizing silicon nanowires with TM atoms presents us a wide range of interesting properties, such as half-metals, 1D ferromagnetic semiconductors or metals and nanomagnets.

We believe that our findings hold promise for the use of these structures in nanospintronics including various applications like magnetoresistance, spin-valve and non-volatile memories.

Chapter 7

Publications of the Author

7.1 Refereed Journals (SCI)

1. "Oscillatory exchange coupling in linear magnetic molecules" H. Sevincli, **E. Durgun**, R. T. Senger, and S. Ciraci *J. Phys.:Condens. Matter* 19, 216205 (2007).
2. "Hydrogen absorption properties of metal-ethylene complexes" W. Zhou, T. Yildirim, **E. Durgun**, and S. Ciraci *Phys. Rev. B* (in press).
3. "Theoretical study of hydrogen adsorption on single-wall BN tubes" **E. Durgun**, Y.-R. Jang, and S. Ciraci, *Phys. Rev. B* (Brief Report) (in press).
4. "Transition Metal-Ethylene Complexes as High-Capacity Hydrogen Storage Media" **E. Durgun**, S. Ciraci, W. Zhou, and T. Yildirim *Phys. Rev. Lett.* 97, 226102 (2006) [Cover page of December 1, 2006 issue].
5. "Electronic and mechanical properties of molybdenum selenide type nanowires by plane-wave pseudopotential calculations" D. Cakir, **E. Durgun**, O. Gulseren, and S. Ciraci *Phys. Rev. B* 74, 235433 (2006).
6. "Spintronic properties of carbon-based one-dimensional molecular structures" **E. Durgun**, H. Mehrez, R. T. Senger, H. Sevincli and S. Ciraci, *Phys. Rev. B* 74, 235413 (2006).

7. "Hydrogen storage capacity of titanium met-cars" N. Akman, **E. Durgun**, and S. Ciraci, *J. Phys.:Condens. Matter* 18, 9509-9517 (2006).
8. "Size-dependent alternation of magnetoresistive properties in atomic chains" **E. Durgun**, R. T. Senger, H. Mehrez, S. Dag, and S. Ciraci, *Journal of Chemical Physics* 125, 121102 (2006).
9. "Spin-dependent electronic structure of transition metal atomic chains adsorbed on single-wall carbon nanotubes" **E. Durgun** and S. Ciraci, *Phys. Rev. B* 74, 125404 (2006).
10. "Nanospintronic properties of carbon-cobalt atomic chains" **E. Durgun**, R. T. Senger, H. Mehrez, S. Dag and S. Ciraci *Europhys. Lett*, 73, 642 (2006).
11. "Half-metallic properties of atomic chains of carbon-transition-metal compounds" S. Dag, S. Tongay, T. Yildirim, **E. Durgun**, R. T. Senger, C. Y. Fong, and S. Ciraci, *Phys. Rev. B* 72, 155444 (2005).
12. "Atomic and electronic structure of carbon strings" S. Tongay, S. Dag, **E. Durgun**, R. T. Senger, and S. Ciraci, *J. Phys.:Condens. Matter* 17, 3823 (2005).
13. "Silicon and III-V compound nanotubes: Structural and electronic properties" **E. Durgun**, S. Tongay, and S. Ciraci *Phys. Rev. B* 72, 075420 (2005).
14. "Atomic chains of group-IV elements and III-V and II-VI binary compounds studied by a first-principles pseudopotential method" R. T. Senger, S. Tongay, **E. Durgun**, and S. Ciraci *Phys. Rev. B* 72, 075419 (2005).
15. "Carbon string structures: First-principles calculations of quantum conductance" R. T. Senger, S. Tongay, S. Dag, **E. Durgun**, and S. Ciraci *Phys. Rev. B* 71, 235406 (2005).
16. "Theoretical study of Ga-based nanowires and the interaction of Ga with single-wall carbon nanotubes" **E. Durgun**, S. Dag, and S. Ciraci *Phys. Rev. B* 70, 155305 (2004).

17. "High-conducting magnetic nanowires obtained from uniform titanium-covered carbon nanotubes" S. Dag, **E. Durgun**, and S. Ciraci *Phys. Rev. B* 69, 121407 (2004).
18. "Energetics and Electronic Structures of Individual Atoms Adsorbed on Carbon Nanotubes" **E. Durgun**, S. Dag, S. Ciraci, O. Gulseren *J. of Phys. Chem. B* 108(2); 575-582 (2004).
19. "Atomic strings of group IV, III-V, and II-VI elements" S. Tongay, **E. Durgun**, S. Ciraci *Appl. Phys. Lett.* 85, 6179 (2004).
20. "Systematic study of adsorption of single atoms on a carbon nanotube" **E. Durgun**, S. Dag, V. M. K. Bagci, O. Gulseren, T. Yildirim, and S. Ciraci *Phys. Rev. B* 67, 201401 (2003).
21. "Functionalization of carbon based nanostructures with light transition metal atoms for hydrogen storage" **E. Durgun**, T. Yildirim, and S. Ciraci, *Phys. Rev. B* (submitted).
22. "Half-metallic silicon nanowires" **E. Durgun**, D. Cakir, N. Akman and S. Ciraci, *Phys. Rev. Lett* (submitted).
23. "Atomic and electronic structure of doped silicon nanowires" **E. Durgun**, N. Akman, C. Ataca, S. Ciraci, *Phys. Rev. B* (submitted).
24. "Functionalization of silicon nanowires" **E. Durgun**, N. Akman and S. Ciraci (to be submitted to Phys. Rev. B).
25. "Electronic and magnetic properties of transition metal atomic chains" S. Cahangirov, C. Ataca, **E. Durgun**, Y.R. Jang, and S. Ciraci (to be submitted to Phys. Rev. B).
26. "Si-Ge nanowire superlattices" **E. Durgun**, N. Akman, S. Cahangirov, and S. Ciraci (to be submitted to Phys. Rev. B).
27. "Electronic and magnetic properties of transition metal element adsorbed graphene and graphene ribbons" H. Sevincli, M. Topsakal, **E. Durgun**, and S. Ciraci (to be submitted to Phys. Rev. B).

28. "Multiple quantum well structures of graphene ribbons" M. Topsakal, H. Sevincli, **E. Durgun**, and S. Ciraci (to be submitted to Phys. Rev. Lett).

7.2 Conference Proceedings

29. "Theoretical models for Nanodevices and Nanomagnets Based on Single-Wall Carbon Nanotubes" S. Ciraci, O. Gulseren, T. Yildirim, S. Dag, and **E. Durgun** Proceedings of NATO-ASI (Nanoengineered Nanofibrous Materials) 169, 181 Kluwer (2003).
30. "Functionalization of Carbon Nanotubes: Deformation, Coating, Contacts and Device Applications" O. Gulseren, T. Yildirim, S. Dag, **E. Durgun**, and S. Ciraci Proceedings of NATO-ASI (Nanoengineered Nanofibrous Materials) 169, 163 Kluwer (2003).

7.3 Non-SCI Journals

31. **E. Durgun** and S. Ciraci, Turkish Journal of Physics 29, 307 (2006).
32. S. Dag , **E. Durgun**, and S. Ciraci, Turkish Journal of Physics 29, 295 (2006).

7.4 Popular Magazine

1. "Yakıt Hücreleri" **E. Durgun**, TÜBİTAK Bilim ve Teknik Dergisi (Yeni Ufuklara Eki) sayı 467, sayfa 8 (Ekim 2006).
2. "Spin Elektronığı" R. T. Senger ve **E. Durgun**, TÜBİTAK Bilim ve Teknik Dergisi, sayı 471, sayfa 70 (Şubat 2007).
3. "Silisyum Nanoteller" **E. Durgun**, N. Akman ve S. Çıracı TÜBİTAK Bilim ve Teknik Dergisi, sayı 474 , sayfa 60 (Mayıs 2007).

Bibliography

- [1] G. A. Prinz, *Science* **282**, 1660 (1998).
- [2] S. A. Wolf, D. D. Awschalom, R. A. Buhrman, J. M. Daughton, S. von Molnar, M. L. Roukes, A. Y. Chtchelkanova, and D. M. Treger, *Science* **294**, 1488 (2001).
- [3] I. Zutic, J. Fabian, and S. Das Sarma, *Rev. Mod. Phys.* **76**, 323 (2004).
- [4] N. F. Mott, *Proc. R. Soc. London, Ser. A* **153**, 699 (1936). N. F. Mott, *Proc. R. Soc. London, Ser. A* **156**, 368 (1936).
- [5] T. Valet and A. Fert, *Phys. Rev. B* **48**, 7099 (1993).
- [6] E. L. Nagaev, *Physics of Magnetic Semiconductors* (Mir, Moscow) 1983.
- [7] L. Esaki, P. Stiles, and S. von Molnar, *Phys. Rev. Lett.* **19**, 852 (1967).
- [8] J. S. Moodera, X. Hao, G. A. Gibson, and R. Meservey, *Phys. Rev. B* **42**, 8235 (1988).
- [9] M. Julliere, *Phys. Lett.* **54A**, 225 (1975).
- [10] S. Maekawa and U. Gafvert, *IEEE Trans. Magn.* **18**, 707 (1982).
- [11] M. N. Baibich, J. M. Broto, A. Fert, F. Nguyen Van Dau, F. Petroff, P. Eitenne, G. Creuzet, A. Friederich, and J. Chazelas, *Phys. Rev. Lett.* **61**, 2472 (1988).
- [12] P. Bruno, *Phys. Rev. B* **52**, 411 (1995).

- [13] M. D. Stiles, J. Magn. Magn. Mater. **200**, 322 (1999).
- [14] S. S. P. Parkin, N. More, K. P. Roche, Phys. Rev. Lett. **64**, 2304 (1990).
- [15] D. M. Edwards, J. Mathon, R. B. Muniz, and M. S. Phan, Phys. Rev. Lett. **67**, 493 (1991).
- [16] J. d'Albuquerque e Castro, M. S. Ferreira, R. B. Muniz, Phys. Rev. B **49**, 16062 (1994).
- [17] J. S. Moodera, L. R. Kinder, T. M. Wong, R. Meservey, Phys. Rev. Lett. **74**, 3273 (1995).
- [18] C. Tsang, R. E. Fontana, T. Lin, D. E. Heim, V. S. Speriosu, B. A. Gurney, and M. L. Williams, IEEE Trans. Magn. **30**, 3801 (1994).
- [19] R. E. Scheuerlein *et al.*, IEEE ISSCC Digest of Technical Papers Cat. No.00CH37056, 128 (2000).
- [20] R. A. de Groot, F. M. Mueller, P. G. van Engen, and K. H. J. Buschow, Phys. Rev. Lett. **50**, 2024 (1983).
- [21] W.E. Pickett and J. S. Moodera, Phys. Today **54**, 39 (2001).
- [22] K. Schwarz, J. Phys. F **16**, L211 (1986).
- [23] A. Yamase and K. Shiratori, J. Phys. Soc. Jpn. **53**, 312 (1984).
- [24] Y. Okimoto, T. Katsufuji, T. Ishikawa, A. Urushibara, T. Arima and Y. Tokura, Phys. Rev. Lett. **75**, 109 (1995).
- [25] H. Akinaga, T. Manago and M. Shirai, Jpn. J. Appl. Phys. **39**, L1118 (2000).
- [26] Y-W Son, M.L. Cohen and S.G. Louie, Nature **444** 347, (2006); Phys. Rev. Lett. **97**, 216803 (2006).
- [27] E. G. Emberly and G. Kirczenow, Chem. Phys. **281**, 311 (2002).
- [28] Y. Wei, Y. Xu, J. Wang, and H. Guo, Phys. Rev. B **70**, 193406 (2004).

- [29] A. R. Rocha, V. M. García-Suárez, S. W. Bailey, C. J. Lambert, J. Ferrer, and S. Sanvito, *Nature Mat.* **4**, 335 (2005).
- [30] H. Dalglish and G. Kirczenow, *Phys. Rev. B* **72**, 184407 (2005).
- [31] D. Waldron, P. Haney, B. Larade, A. MacDonald, and H. Guo, *Phys. Rev. Lett.* **96**, 166804 (2006).
- [32] A. R. Rocha, V. M. García-Suárez, S. Bailey, C. Lambert, J. Ferrer, and S. Sanvito, *Phys. Rev. B* **73**, 085414 (2006).
- [33] J.-L. Mozos, C. C. Wan, G. Taraschi, J. Wang, and H. Guo, *Phys. Rev. B* **56**, R4351 (1997).
- [34] P. Sen, S. Ciraci, A. Buldum, and I. P. Batra, *Phys. Rev. B* **64**, 195420 (2001).
- [35] B. Larade, J. Taylor, H. Mehrez, and H. Guo, *Phys. Rev. B* **64**, 075420 (2001).
- [36] N. Agrait, C. Untiedt, G. Rubio-Bollinger, and S. Vieira, *Phys. Rev. Lett.* **88**, 216803 (2002).
- [37] F. J. Ribeiro and M. L. Cohen, *Phys. Rev. B* **68**, 035423 (2004).
- [38] F. Picaud, V. Pouthier, C. Girardet, E. Tosatti, *Surf. Sci.* **547**, 249 (2003).
- [39] S. Okano, K. Shiraishi, and A. Oshiyama, *Phys. Rev. B* **69**, 045401 (2004).
- [40] E. Z. da Silva, F. D. Novaes, A. J. R. da Silva, and A. Fazzio, *Phys. Rev. B* **69**, 115411 (2004).
- [41] S. Tongay, S. Dag, E. Durgun, R. T. Senger, and S. Ciraci, *J. Phys.: Condens. Matter* **17**, 3823 (2005).
- [42] R. T. Senger, S. Tongay, S. Dag, E. Durgun, and S. Ciraci, *Phys. Rev. B* **71**, 235406 (2005).
- [43] R. T. Senger, S. Tongay, E. Durgun, and S. Ciraci, *Phys. Rev. B* **72**, 075419 (2005).

- [44] S. R. Bahn and K. W. Jacobsen, Phys. Rev. Lett. **87**, 266101 (2001).
- [45] A. Smogunov, A. Dal Corso, and E. Tosatti, Phys. Rev. B **70**, 045417 (2004).
- [46] M. Wierzbowska, A. Delin, and E. Tosatti, Phys. Rev. B **72**, 035439 (2005).
- [47] A. Smogunov, A. Dal Corso, and E. Tosatti, Phys. Rev. B **73**, 075418 (2006).
- [48] S. Iijima, Nature **354**, 56-58 (1991).
- [49] E. Durgun, Master Thesis "Systematic Study of Single Atom Adsorption on Single-Wall Carbon Nanotubes" (2003).
- [50] A. T. Costa, D. F. Kirwan, and M. S. Ferreira, Phys. Rev. B **72**, 085402 (2005).
- [51] V. B. Shenoy, Phys. Rev. B **71**, 125431 (2005).
- [52] S. Sahoo, T. Kontos, J. Furer, C. Hoffmann, M. Graber, A. Cottet and C. Schonenberger, Nature Physics **1**, 99 (2005).
- [53] K. Tsukagoshi, B. W. Alphenaar and H. Ago, Nature **401**, 572 (1999).
- [54] D. D. D. Ma, C. S. Lee, F. C. K. Au, S. Y. Tong, S. T. Lee, Science **299**, 1874 (2003).
- [55] Y. Cui, Z. Zhong, D. Wang, W. U. Wang and C. M. Lieber, Nano Lett. **3**, 149 (2003).
- [56] Y. Huang, X. F. Duan and C. M. Lieber, Small **1**, 142 (2005).
- [57] X. F. Duan, Y. Huang, R. Agarwal and C. M. Lieber, Nature(London) **421**, 241 (2003).
- [58] H. W. Wu, C. J. Tsai, and L. J. Chen, Appl. Phys. Lett. **90**, 043121 (2007).
- [59] M. Born and J. R. Oppenheimer, Ann. der Phys. **84**, 457 (1927).
- [60] D. R. Hartree, Proc. Cambridge. Philos. Soc. **24**, 89 (1928).

- [61] V. Fock, Z. Phys. **61**, 126 (1930).
- [62] J. C. Slater, Phys. Rev. **35**, 210 (1930).
- [63] L. H. Thomas, Proc. Cambridge. Philos. Soc. **23**, 542 (1927).
- [64] E. Fermi, Z. Phys. **48**, 73 (1928).
- [65] P. Hohenberg and W. Kohn, Phys. Rev. **136**, B864 (1964)
- [66] W. Kohn and L. J. Sham, Phys. Rev. **140**, A1133 (1965).
- [67] D. M. Ceperley and B. J. Alder, Phys. Rev. Lett. **45**, 566 (1980).
- [68] J. P. Perdew and Y. Wang, Phys. Rev. B, **45**, 13244 (1991).
- [69] A. D. Becke, Phys. Rev A **38**, 3098-3100 (1988).
- [70] J. P. Perdew, K. Burke, and M. Ernzerhof, Phys. Rev. Lett, **77**, 3865-3868 (1996).
- [71] V. I. Anisimov, F. Aryasetiawan, and A. I. Lichtenstein, J.Phys.: Condensed Matter **9**,767-808 (1997).
- [72] J. Hubbard, Proc. Roy. Soc. London, series A **285**, 542 (1965).
- [73] C. Kittel *Introduction to Solid State Physics* (Wiley and Sons, New York, 1996).
- [74] H.J. Monkhorst and J.D. Pack, Phys. Rev. **B13**, 5188, (1976).
- [75] D. Vanderbilt, Phys. Rev. B **41**, R7892 (1990).
- [76] P. E. Blochl, Phys. Rev. B **50**, 17953-17979 (1994).
- [77] R. Landauer, Philos. Mag. **21**, 863 (1970).
- [78] S. Datta, *Electronic Transport in Mesoscopic Systems* (Cambridge University Press, Cambridge, 1995).
- [79] X. Zhao, Y. Ando, Y. Liu, M. Jinno, and T. Suzuki, Phys. Rev. Lett. **90**, 187401 (2003).

- [80] M. C. Payne, M. P. Teter, D. C. Allen, T. A. Arias and J. D. Joannopoulos, *Rev. Mod. Phys.* **64**, 1045 (1992).
- [81] Numerical computations have been carried out by using VASP software: G. Kresse, J. Hafner, *Phys Rev. B* **47**, 558 (1993); G. Kresse, J. Furthmuller, *Phys Rev. B* **54**, 11169 (1996).
- [82] S. A. Adelman and J. D. Doll, *J. Chem. Phys.* **64**, 2375 (1976).
- [83] E. Durgun, H. Mehrez, R. T. Senger, H. Sevincli and S. Ciraci, *Phys. Rev. B* **74**, 235413 (2006).
- [84] E. Durgun, R. T. Senger, H. Mehrez, S. Dag, and S. Ciraci, *J. Chem. Phys.* **125**, 121102 (2006).
- [85] H. Sevincli, E. Durgun, R. T. Senger, and S. Ciraci *J. Phys.: Condens. Matter* **19**, 216205 (2007).
- [86] P. Ordejón, E. Artacho, and J. M. Soler, *Phys. Rev. B* **53**, R10441 (1996); J. M. Soler, E. Artacho, J. D. Gale, A. Garcia, J. Junquera, P. Ordejon, and D. Sanchez-Portal, *J. Phys.: Condens. Matter* **14**, 2745 (2002).
- [87] GAUSSIAN 03, Revision C. 02, M. J. Frisch *et al.*, Gaussian Inc., Wollingford CT, 2004.
- [88] M. B. Nardelli, *Phys. Rev. B* **60**, 7828 (1999).
- [89] S. Tongay, R. T. Senger, S. Dag, and S. Ciraci, *Phys. Rev. Lett.* **93**, 136404 (2004).
- [90] G. Roth and H. Fischer, *Organometallics* **15**, 5766 (1996).
- [91] S. Eisler, A.D. Slepko, E. Elliott, T. Luu, R. McDonald, F. A. Hegmann, and R. R. Tykwinski, *J. Am. Chem. Soc.* **127**, 2666 (2005).
- [92] N. D. Lang and Ph. Avouris, *Phys. Rev. Lett.* **81**, 3515 (1998); *Phys. Rev. Lett.* **84**, 358 (2000).
- [93] N. D. Lang, *Phys. Rev. B* **52**, 5335 (1995); *Phys. Rev. Lett.* **79**, 1357 (1997).

- [94] M. A. Ruderman, and C. Kittel, *Phys. Rev.* **96**, 99 (1954); T. Kasuya, *Prog. Theor. Phys.* **16**, 45 (1956); T. Kasuya, *Prog. Theor. Phys.* **16**, 58 (1956); K. Yosida, *Phys. Rev.* **106**, 893 (1957).
- [95] P. Bruno, *J. Magn. Magn. Mater.* **121**, 238 (1993).
- [96] P. Bruno, *Phys. Rev. B* **52**, 411 (1995).
- [97] M. D. Stiles, *Phys. Rev. B* **48**, 7238 (1993).
- [98] R. Pati, M. Mailman, L. Senapati, P. M. Ajayan, S. D. Mahanti, and S. K. Nayak, *Phys. Rev. B* **68**, 014412 (2003).
- [99] L. Senapati, R. Pati, M. Mailman, and S. K. Nayak, *Phys. Rev. B* **72**, 064416 (2005).
- [100] R. Seeger and J. A. Pople, *J. Chem. Phys.* **66**, 3045 (1977).
- [101] S. Dag, S. Tongay, T. Yildirim, E. Durgun, R. T. Senger, C. Y. Fong, and S. Ciraci, *Phys. Rev. B* **72**, 155444 (2005).
- [102] E. Durgun, R. T. Senger, H. Mehrez, S. Dag, and S. Ciraci, *Europhys. Lett.* **73**, 642 (2006).
- [103] S. Ciraci, S. Dag, T. Yildirim, O. Gülseren, and R. T. Senger, *J. Phys.: Condens. Matter* **16**, R901 (2004).
- [104] S. B. Fagan, R. Mota, A. J. R. da Silva, and A. Fazzio, *Phys. Rev. B* **67**, 205414 (2003).
- [105] S. B. Fagan, R. Mota, A. J. R. da Silva, and A. Fazzio, *Microelectronics Journal* **34**, 481 (2003).
- [106] S. B. Fagan, R. Mota, A. J. R. da Silva, and A. Fazzio, *J. Phys.: Condens. Matter* **16**, 3647 (2004).
- [107] C. K. Yang, J. Zhao, and J. P. Lu, *Phys. Lett.* **90**, 257203 (2003).
- [108] M. S. Ferreira and S. Sanvito, *Phys. Rev. B* **69**, 035407 (2004).

- [109] E. Durgun, S. Dag, V. M. K. Bagci, O. Gülseren, T. Yildirim, and S. Ciraci, *Phys. Rev. B* **67**, R201401 (2003)
- [110] E. Durgun, S. Dag, S. Ciraci, and O. Gülseren, *J. Phys. Chem. B* **108**(2), 575 (2004).
- [111] B. Zhao, I. Monch, T. Muhl, and C. M. Schneider, *Appl. Phys. Lett.* **80**, 3144 (2002).
- [112] S.J. Tans, M.H. Devoret, H. Dai, A. Thess, R.E. Smalley, L.J. Geerlings, and C. Dekker, *Nature (London)* **386**, 474 (1997).
- [113] S. Frank, P. Poncharal, Z.L. Wang, and W.A. de Heer, *Science* **280**, 1744 (1998).
- [114] C. Yang, J. Zhao, and J. P. Lu, *Nano. Lett.* **4**, 561 (2004).
- [115] Y. Yagi, T. M. Briere, M. H. F. Sluiter, V. Kumar, A. A. Farajian, and Y. Kawazoe, *Phys. Rev. B* **69**, 075414 (2004).
- [116] M. Methfessel and A. T. Paxton, *Phys. Rev. B* **40**, 3616 (1989).
- [117] For the definition of the radial strain ϵ_r see for example: O. Gülseren, T. Yildirim, S. Ciraci and C. Kilic, *Phys. Rev. B* **65**, 155410 (2002).
- [118] Y. Zhang and H. Dai, *Appl. Phys. Lett.* **77**, 3015 (2000); Y. Zhang, N.W. Franklin, R.J. Chen, and H. Dai, *Chem. Phys. Lett.* **331**, 35 (2000).
- [119] A. N. Andriotis, M. Menon, and G. E. Froudakis, *Phys. Rev. B*, **62**, 9867 (2000).
- [120] X. Blase, L. X. Benedict, E. L. Shirley, and S. G. Louie, *Phys. Rev. Lett.* **72**, 1878 (1994).
- [121] D. M. Duffy and J. A. Blackman, *Phys. Rev. B*, **58**, 7443 (1998).
- [122] J. Friedel, *The Physics of Metals*, edited by J. M. Ziman (Cambridge University Press, New York, 1969); D.G. Pettifor, in *Solid State Physics*, edited by H. Ehrenreich and D. Turnbull (Academic, New York, 1987). Vol. **40**, p43.

- [123] X. Blase, L.X. Benedict, E.L. Shirley and S.G. Louie, *Phys. Rev. Lett.* **72**, 1878 (1994).
- [124] O. Gülseren, T. Yildirim, and S. Ciraci, *Phys. Rev. B* **65**, 153405 (2002).
- [125] E. Durgun, D. Cakir, N. Akman, and S. Ciraci, *Phys. Rev. Lett.* (submitted)
- [126] S. L. Dudarev, G. A. Botton, S. Y. Savrasov, C. J. Humphreys and A. P. Sutton, *Phys. Rev. B*, **57**, 1505 (1998).